

Production and Characterization of Novel Catalysts Based on Bimetallic Deposited Clusters

Ting-Wei Liao

Supervisor:
Prof. Peter Lievens
Co-supervisor:
Dr. Didier Grandjean

Dissertation presented in partial
fulfilment of the requirements for the
degree of Doctor of Science

Members of the Examination Committee:

Prof. Lino da Costa Pereira	Chairman
Prof. Ewald Janssens	
Prof. Bert Sels	
Prof. Margriet Van Bael	
Prof. Francesca Baletto	King's College London
Prof. Sammy W. Verbruggen	University of Antwerp

© 2018 KU Leuven, Science, Engineering & Technology
Uitgegeven in eigen beheer, Ting-Wei Liao, Celestijnenlaan 200D, 3001 Leuven,
Belgium

Alle rechten voorbehouden. Niets uit deze uitgave mag worden vermenigvuldigd en/of openbaar gemaakt worden door middel van druk, fotokopie, microfilm, elektronisch of op welke andere wijze ook zonder voorafgaandelijke schriftelijke toestemming van de uitgever.

All rights reserved. No part of the publication may be reproduced in any form by print, photoprint, microfilm, electronic or any other means without written permission from the publisher.

Acknowledgement

The past years have been an exciting journey. This work could not have been completed without the tremendous help and support in every possible way from colleagues, friends and family. I would like to take this opportunity to express my most sincere gratitude to all the people who have helped and supported me along the way.

First of all, I would like to thank my promoter, Prof. Peter Lievens and co-supervisor Dr. Didier Grandjean for offering me this opportunity to conduct my PhD research in the CLASS group, VSM, KU Leuven. Furthermore, thank you both for providing me this excellent position allowing me to build up knowledge, have many great experiences and network within the CATSENSE ITN project (FP7/2007-2013 n° 607417). Because of you, I got to do experiments in a multitude of institutes all over the world while collaborating with amazing people from diverse backgrounds. The guidance, supervision and strong support I received from you are most appreciated. Special thanks to Dr. Didier Grandjean for sharing the repertoire of your ideas, experiences and advice with me. I also would like to thank you for a great opportunity to participate in X-ray characterization experiments with you at the ESRF.

Furthermore, I would like to thank all my examination committee members: Prof. Peter Lievens, Dr. Didier Grandjean, Prof. Lino da Costa Pereira, Prof. Ewald Janssens, Prof. Bert Sels, Prof. Margriet Van Bael, Prof. Francesca Baletto of the King's College London and Prof. Sammy W. Verbruggen of the University of Antwerp. Thank you all for your valuable feedback and comments on the manuscript to enhance the quality of this thesis.

Also thanks to the Department of Physics and Astronomy for their relentless support. Special thanks to Prof. Ewald Janssens for the support and the extensive collaboration especially during the final phase of my PhD. In particular, I would like to thank for all the advice and support, both scientific and technical, from Prof. Margriet Van Bael, Prof. Chris Van Haesendonck, Prof. Lino da Costa Pereira, Prof. André Vantomme, and Prof. Jean-Pierre Locquet. You have my sincere gratitude for the opportunities you provided me to learn a variety of techniques, allowing me to become a more capable researcher. Without your help, I would have had no chance to use AFM, STM, XRD, XPS, RBS and LEED during my PhD. I would also like to thank Prof. Bert Sels at the Centre for Surface Chemistry and Catalysis for his support of CO oxidation experiments. Furthermore, my immense appreciation goes to the technical supports from Philippe Mispelter, Stijn Vandezande, Bas Oppendoes, Valentijn Tuts and Sven Villé. The administrative assistance from Monique Van Meerbeek and Liliane Goffin is equally appreciated.

This work highly depended on the Cluster Deposition Apparatus (CDA). I could not familiar with the setup so fast without the experience sharing and training on the CDA from Kelly, Tobias, Piero and Johanna at the beginning of my PhD. I also would like to thank Dr. Thomas Picot and Dr. Arnaud Hillion for guiding me with using the Magnetron sputtering setup. My office mates, Didier, Yejun, Meiya and Johan also played important roles during my PhD years. Thank you for being there when I needed encouragement and support. My special thanks to Johan for all the suggestions and ideas, not only in the labs, but in many other aspects. I also must thank my lab mates (in any labs): Anupam, Salvo, Kuo-Juei, Pin-Cheng, Zhe, Jeroen, Saleh, Matías, Jan, Slava, Pía, Asteriona, Sasha, Uma and Qiang. Thank you all for the discussions and helping me with experiments. I enjoyed the moments we had in the labs and thank you for the time you spent troubleshooting with me. Special thanks to Anupam for great assistance in sample preparations and all the ideas that you shared with me.

I value and cherish the opportunity to have been a member of the CATSENSE ITN project. I would like to thank all my collaborators at the University of Birmingham, University of Milan, Teer Coatings Limited and Swansea University. All of you enabled the discoveries made during my PhD journey.

In the past few years, I have had a wonderful time with my Taiwanese friends in Leuven. You are an essential part of my life here. My gratitude goes to every one of you, for arranging all kinds of activities and always inviting me to join. I would like to thank the Education Division of Taipei representative office in the EU and Belgium. Thank you for providing us opportunities to meet different people and expand my social network.

Finally, my deepest appreciation goes to my family, especially my parents. Thank you for your unconditional support and for always allowing me to do whatever I set my mind on. Although we are continents apart, your constant encouragement and support never ceased to reach me.

I could not have come so far on my own. Without any one of you, this fantastic journey would not have been this fantastic.

Ting-Wei

December 2018

Abstract

The remarkable catalytic activities of metal nanoclusters and their promising applications in sustainable energy development and environmental protection have attracted a great interest. Nanoclusters (NCs) are typically composed of less than thousand atoms and have dimensions smaller than a few nanometres. They have unique plasmonic, catalytic, and magnetic properties, distinct from those of bulk materials. Different from the monometallic nanoclusters, the physical and chemical properties of their bimetallic counterparts can be further fine-tuned by their composition and atomic arrangements while the synergistic effect of bimetallic nanoclusters can be fundamentally investigated to design better catalysts. Bimetallic nanoclusters are promising candidates for new energy harvesting and pollution reduction applications. Designing new catalysts by depositing preformed bimetallic nanoclusters, with well-defined sizes and compositions, on oxide supports, could be one of the key solutions to achieve this goal.

Today many important technologies such as automobile catalytic converters, oxidation catalysis and biomedical engineering rely upon the catalytic properties of bimetallic nanoparticles and nanoclusters. Achieving sustainable development in the current world's economy is faced with two major obstacles: the increasing energy demand and rising pollution levels. Therefore, it is crucial to better understand the origin of metal NCs characteristic catalytic properties to increase their reactivity, selectivity and stability to design better catalysts. There are four main factors that influence the physical and chemical properties of bimetallic clusters, which are the size, the composition, the chemical ordering and their interaction with the support. However, the roles of each individual and combined parameters in the performance of catalysts still remain not fully understood. Thus understanding at an atomic level the synergy between two metals through an accurate control of the size and composition of the bimetallic nanoclusters (BNCs) is essential.

The main objective of this PhD thesis is based on the production of deposited BNCs by cluster beam deposition methods, the characterization of the deposited BNCs to reveal their properties and the application of the deposited BNCs on various oxide supports as novel catalysts. Therefore, systematic synthesis and investigations of bimetallic nanoclusters, produced by cluster beam deposition with precise composition control, are carried out. Furthermore, the atomic structure, composition/synergistic effect and support interaction on the catalytic properties of designed bimetallic nanoclusters are studied with various catalytic, electronic and spectroscopic characterization techniques.

In **Chapter 1**, general aspects of NCs are introduced along with a short history of the development of nanotechnology. A concise overview of the mono-/bi-metallic NCs synthesis methods and the important research results obtained by tuning the properties of nanoclusters with different parameters are also discussed. Laser ablation cluster sources and magnetron sputtering sources with different composition control methods are described and compared. In addition, examples of fine-tuning the catalytic properties of supported clusters towards CO oxidation are reviewed. Also other catalytic and photocatalytic applications of bimetallic nanoclusters/nanoparticles are discussed in this chapter.

In **Chapter 2**, the nanocluster synthesis methods and the characterization techniques used in this thesis are described in detail. First of all, the three cluster sources used in this work, i.e. laser ablation, magnetron sputtering, and matrix assembly cluster sources, are described. In the laser ablation-based source, a precise control of the cluster composition is obtained by fine-tuning the laser power applied on the metal targets while the corresponding cluster beam is characterized by high resolution mass spectrometry; therefore, the description of the reflectron time of flight mass spectrometry follows. An overview of the electron microscopy and X-ray spectroscopy techniques utilized to characterize the deposited clusters is presented. The gas flow reactor used to study the catalytic activities of the deposited clusters is introduced. It also includes a detailed description of the temperature programmed desorption system as well as a transferable sample holder for the catalysis studies of supported clusters under ultra-high vacuum condition.

In **Chapter 3**, an extensive investigation of the structural and electronic properties of composition-controlled $\text{Au}_x\text{Ag}_{1-x}$ bimetallic nanoclusters (BNCs) over the full Au/Ag miscibility range is presented. Their synthesis method is introduced while the composition-dependent phase-segregated structures of deposited $\text{Au}_x\text{Ag}_{1-x}$ bimetallic nanoclusters are investigated by a combination of high-angle annular dark-field (HAADF) scanning transmission electron microscopy (STEM), X-ray absorption fine structure and X-ray photoelectron spectroscopies. A nucleation and growth mechanism of phase segregated $\text{Au}_x\text{Ag}_{1-x}$ bimetallic nanoclusters supported by density functional theory (DFT) calculations is proposed.

Preliminary investigation of the catalytic activity under atmospheric pressure of $\text{Au}_x\text{Ag}_{1-x}$ BNCs supported by SiO_2 , TiO_2 and MgO in the CO oxidation model reaction is reported in **Chapter 4**. These BNCs with different compositions are deposited on various supports both using the laser ablation and the matrix assembly cluster sources to study the composition and support interaction effects on their CO oxidation activity in a tube gas flow reactor.

The catalytic activity of SiO₂ supported Pt_xNi_{1-x} BNCs in methanol decomposition reactions are investigated under low pressure using a home-built temperature programmed desorption setup described in **Chapter 5**. A significant reduction of CO poisoning of Pt NCs upon Ni alloying is demonstrated in Pt_xNi_{1-x} BNCs. Structures of series of Pt_xNi_{1-x} BNCs produced in the laser ablation cluster source are studied by HAADF-STEM. Furthermore, the electronic interaction between Pt atoms and CO molecules is investigated by density functional theory.

Finally, in **Chapter 6**, the application of Au NCs produced by laser ablation and deposited on TiO₂ surface as photocatalysts is discussed. The effect of ligand-free Au clusters coverage on the photocatalytic stearic acid degradation activity under ultraviolet and visible light is investigated by monitoring the molecule degradation with Fourier-transform infrared spectroscopy. The correlation between the surface morphology and the UV-VIS absorption is also studied.

The main results and conclusions in the aforementioned chapters are summarized in the **General Conclusions and Perspective**. Based on the knowledge obtained in this work, directions for further investigations on the cluster production and their catalytic properties with gas flow reactors, as well as their application in photocatalysis are formulated.

Uittreksel in het Nederlands

Recentelijk is er veel interesse ontstaan in metalen nanoclusters, dit vanwege de ongebruikelijke katalytische eigenschappen en de mogelijke toepassingen voor het aanboren van nieuwe energiebronnen, alsmede de bescherming van het milieu. Typisch zijn nanoclusters opgebouwd uit minder dan duizend atomen met afmetingen kleiner dan een paar nanometer. Ze bezitten unieke plasmonische, katalytische en magnetische eigenschappen die zeer verschillen van die van massief materiaal. In tegenstelling tot de éénmetalige versies bieden nanoclusters bestaande uit twee metalen de mogelijkheid tot fijnafstemming van hun fysische en chemische eigenschappen, door middel van een goede controle over hun compositie en atomaire indeling. Fundamenteel onderzoek naar de synergie tussen deze twee metalen stelt ons in staat betere katalysatoren te ontwerpen. Deze tweemetalige nanoclusters vormen dus veelbelovende kandidaten voor het oogsten van nieuwe energiebronnen en het vinden van toepassingen die vervuiling tegengaan. Nieuw ontworpen katalysatoren, gemaakt door gevormde tweemetalige nanoclusters met een goedgedefinieerde grootte en compositie op een oxidesubstraat af te zetten, vormen wellicht één van de sleuteloplossingen in de speurtocht naar het bereiken van dit doel.

Veel belangrijke technologieën zijn vandaag de dag afhankelijk van de katalytische eigenschappen van tweemetalige nanodeeltjes en nanoclusters. Voorbeelden van zulke toepassingen zijn te vinden in driewegkatalysatoren, oxidatiekatalyse en de biomedische technologie. Op de weg naar duurzame ontwikkeling in de huidige wereldeconomie liggen twee grote obstakels: de steeds hogere vraag naar energie en de toenemende luchtvervuiling. Daarom is het essentieel om beter te begrijpen wat de oorsprong van de karakteristieke katalytische eigenschappen van deze tweemetalige deeltjes is, om aan de ene kant hun reactiviteit en selectiviteit te verhogen, en aan de andere kant om betere katalysatoren te ontwerpen. Er zijn drie hoofdfactoren die de fysische en chemische eigenschappen van tweemetalige clusters beïnvloeden, de grootte, de samenstelling, en de wisselwerking tussen de clusters en hun drager. De rollen van zowel de individuele als de gecombineerde parameters zijn echter nog steeds niet volledig begrepen. Daarom is het voor het ontwerpen van een betere katalysator essentieel om de synergie tussen de twee metalen op een atomair niveau te begrijpen, en dit door middel van een nauwkeurige controle van de grootte en de samenstelling van deze tweemetalige nanoclusters.

Het hoofddoel van dit proefschrift is het produceren en kenschetsen van nieuwe katalysatoren, gebaseerd op de afzetting van in een clusterbundel geproduceerde tweemetalige nanoclusters op een substraat, met een precieze controle over de deeltjessamenstelling. Deze afzettingen worden systematisch gesynthetiseerd en

vervolgens onderzocht. Bovendien worden de atomaire structuur, de katalytische eigenschappen en de effecten van samenstelling, synergie en de keuze van het substraat bestudeerd door middel van een breed scala aan katalytische, elektronische en spectroscopische karakterisatietechnieken.

In **Hoofdstuk 1** worden de algemene aspecten van clusters geïntroduceerd tezamen met een korte geschiedenis van de ontwikkelingen in de nanotechnologie. Bovendien bevat het een beknopt overzicht van de één- en tweemetalige synthesemethodes alsmede de belangrijkste onderzoeksresultaten betreffende het aanpassen van de eigenschappen van nanoclusters als functie van de verschillende parameters. Clusterbronnen gebaseerd op laserablatie en magnetrongesputter, elk met verschillende methodes voor compositiecontrole, worden beschreven en vergeleken. Daarnaast worden voorbeelden van het fijnafstemmen van de katalytische eigenschappen van het door een substraat gedragen clusters voor het proces van koolstofmonoxide-oxidatie bekeken. Tot slot bespreekt dit hoofdstuk ook nog andere katalytische en fotokatalytische toepassingen van tweemetalige nanoclusters en –deeltjes.

In **Hoofdstuk 2** worden de clustersynthesemethodes en karakterisatietechnieken, zoals gebruikt in dit proefschrift, in detail behandeld. Allereerst beschrijft het de drie clusterbrontypes die terugkomen in dit werk, laserablatie, magnetrongesputter, en matrixassemblage. Bij het eerste type wordt precieze controle over de clustersamenstelling bereikt door het fijnafstemmen van de laser vermogens die worden gebruikt om het materiaal van de doelwitten te verdampen, in combinatie met massaspectroscopie met hoge resolutie. Hiertoe bevat dit hoofdstuk een beschrijving van reflectiegebaseerde vluchtijdmassaspectrometrie. Verder wordt een overzicht van de elektronenmicroscopie en röntgenspectroscopie, die voor het kenschetsen van de afgezette clusters wordt gebruikt, voorgesteld. Bovendien wordt de industrieel relevante gasstroomreactor geïntroduceerd, welke wordt gebruikt om de katalytische eigenschappen van de afgezette clusters te bestuderen. Daarnaast bevat het hoofdstuk een gedetailleerde beschrijving van het temperatuursgeprogrammeerde desorptiesysteem (TPD), alsmede een verplaatsbare monsterhouder ten behoeve van de katalytische studies van de door een substraat gedragen clusters in het ultrahoge vacuum.

De precieze samenstellingscontrole over $\text{Au}_x\text{Ag}_{1-x}$ goudzilveren nanoclusters wordt geïntroduceerd in **Hoofdstuk 3**. De samenstellingsafhankelijkheid van de fasege-segregeerde structuur van de afgezette $\text{Au}_x\text{Ag}_{1-x}$ goudzilveren tweemetalige nanoclusters wordt onderzocht door middel van rastertransmissie-elektronenmicroscopie ringvormig gemeten op hoge hoek gepositioneerde donkervelddetector (HAADF-STEM). Deze fasege-segregeerde structuur wordt bovendien verder onderzocht en bevestigd door röntgenabsorptiefijnstructuurspectroscopie. De vormingsmechanismen en structurele

eigenschappen van deze fasegesegregeerde clusters worden verklaard door middel van dichtheidsfunctionaaltheorie en vervolgens bestudeerd door middel van röntgenfoto-elektronspectroscopie.

Hoofdstuk 4 doet verslag van preliminaire studies betreffende de katalytische koolstofmonoxide-oxidatieactiviteit van een volledige legering van fasegesegregeerde $\text{Au}_x\text{Ag}_{1-x}$ goudzilveren tweemetalige nanoclusters, welke geproduceerd werden in zowel de laserablatiebron als de matrixassemblagebron. Deze tweemetalige nanoclusters werden afgezet op verscheidene dragende substraten. Dit werd gedaan in relatie tot het onderzoek naar het effect van zowel hun samenstelling, alsmede de keuze van het dragende substraat richting de uitvoering van koolstofmonoxide-oxidatiereacties met een industrieel relevante buisgasstroomreactor.

De katalytische activiteit van tweemetalige $\text{Pt}_x\text{Ni}_{1-x}$ platinanickelnanoclusters ten behoeve van methanoldecompositiereacties met een gereduceerde koolstofmonoxide-vergiftiging van de nanoclusters wordt bestudeerd in **Hoofdstuk 5**. Dit gebeurde met een zelf ontwikkelde temperatuursgeprogrammeerde desorptieopstelling. $\text{Pt}_x\text{Ni}_{1-x}$ platinanickel tweemetalige nanoclusters werden vervolgens geproduceerd met de laserablatiebron en bestudeerd met HAADF-STEM om hun structuur te onthullen. Verder werd de wisselwerking tussen platina-atomen en koolstofmonoxidemoleculen bestudeerd door een samenspel van röntgenfoto-elektronspectroscopie en dichtheidsfunctionaaltheorie.

Tot slot wordt in **Hoofdstuk 6** de fotokatalytische toepassing van goudclusters gedragen door een titaandioxidesubstraat besproken. De clusters werden geproduceerd door middel van de laserablatiemethode en direct afgezet op het titaandioxideoppervlak. Ten behoeve van degradatie van stearinezuur onder ultraviolet en zichtbaar licht werd de invloed van een ligandvrije goudclusterbedekking op de fotokatalytische activiteit bestudeerd. Dit gebeurde door middel van fouriergetransformeerde infraroodspectroscopie, om de molecuuldegradatie te monitoren. Als uitsmijter wordt nog de correlatie tussen de morfologie van het oppervlak en UV/VIS-absorptie bestudeerd.

De belangrijkste resultaten en de conclusies zijn samengevat in de **algemene conclusies**. Gebaseerd op de in dit werk verkregen kennis worden aanwijzingen gegeven voor verder speurwerk naar clusterproductie, katalytische studies met gasstroomreactors, en de toepassing van clusters voor fotokatalytische studies.

Contents

Acknowledgement	I
Abstract.....	III
Uittreksel in het Nederlands	VII
Contents	XI
List of Abbreviations	XV
List of Symbols.....	XVII
List of Figures.....	XIX
List of Tables.....	XXV
Chapter 1 Introduction.....	1
1.1 Synthesis of composition and structure controlled nanoclusters	1
1.2 Tuning the properties of nanoclusters	3
1.3 Application of supported bimetallic nanoclusters/nanoparticles	5
1.3.1 Nanoclusters/nanoparticles as Catalysts	5
1.3.2 Nanoclusters/nanoparticles as Photocatalysts	5
1.4 Objective of this thesis	7
Chapter 2 Experimental setups and characterization techniques	9
2.1 Cluster beam deposition methods.....	9
2.1.1 Laser ablation cluster setup	9
2.1.2 Magnetron sputtering cluster setup	13
2.1.3 Matrix Assembly Cluster Source	17
2.1.4 Discussions	19
2.2 Reflectron Time-of-flight mass spectrometry	21
2.3 Rutherford backscattering spectrometry.....	24
2.4 Scanning transmission electron microscopy	27
2.5 X-ray photoelectron spectroscopy.....	29
2.6 X-ray absorption fine structure spectroscopy	31
2.7 Gas flow reactor	37
2.8 Temperature-Programmed Desorption.....	37
2.8.1 General description of the homebuilt TPD setup	41

2.8.2	Sample holder and sample stage.....	42
Chapter 3	Composition-dependent spatial atomic arrangement in Au_xAg_{1-x} bimetallic nanoparticles controlled at the nucleation stage	45
3.1	Introduction.....	46
3.2	Experimental details	48
3.3	Production of composition controlled Au_xAg_{1-x} bimetallic nanoclusters.....	55
3.4	Phase segregated Au_xAg_{1-x} bimetallic nanoclusters.....	56
3.5	Atomic arrangement in Au_xAg_{1-x} bimetallic nanoparticles	59
3.6	Cluster formation mechanism.....	63
3.7	Conclusions.....	67
Chapter 4	CO oxidation on oxide supported Au_xAg_{1-x} bimetallic nanoclusters.....	69
4.1	Introduction.....	69
4.2	Phase segregated Au_xAg_{1-x} nanoclusters deposited on SiO_2 wafers and TiO_2 powders produced by laser ablation cluster source	70
4.3	Fully alloyed Au_xAg_{1-x} nanoclusters deposited on MgO powders produced by matrix assembly cluster source.....	72
4.4	Conclusions.....	75
Chapter 5	Methanol decomposition on CO poisoning reduced Pt_xNi_{1-x} nanoparticles supported by SiO_2	77
5.1	Introduction.....	78
5.2	Experimental details	80
5.3	Morphology of Pt_xNi_{1-x} nanoclusters	82
5.4	Catalytic activity of Pt_xNi_{1-x} nanoclusters.....	83
5.5	Oxidation states and atomic structure of Pt_xNi_{1-x} nanoclusters.....	86
5.6	DFT calculations of the electronic band structure of Pt_xNi_{1-x} nanoclusters and CO-Pt interactions	88
5.7	Conclusions.....	91
Chapter 6	Au nanoclusters modified TiO_2 films toward stearic acid degradation as self-cleaning surfaces under visible light	93
6.1	Introduction.....	94
6.2	Sample preparation and methods.....	95

6.2.1	Preparation of Au nanoclusters modified films.....	95
6.2.2	Film characterization	96
6.2.3	Photocatalysis towards stearic acid degradation	96
6.3	Morphology of Au nanoclusters modified TiO ₂ powder films.....	97
6.4	Photo-degradation of stearic acid on Au cluster modified films	98
6.5	Discussion	100
6.6	Conclusions	102
	General Conclusions and Perspective	103
	Bibliography	107
	List of Publications	125
	Curriculum Vitae	127

List of Abbreviations

Acronym	Description
AFM	Atomic force microscope
BE	Binding energy
BNCs	Bimetallic nanoclusters
BNPs	Bimetallic nanoparticles
CBD	Cluster beam deposition
DC	Direct current
DFT	Density functional theory
DMFC	Direct methanol fuel cell
EDX	Energy-dispersive X-ray spectroscopy
EPR	Electron paramagnetic resonance
EXAFS	Extended X-ray absorption fine structure
FQE	Formal quantum efficiency
FTIR	Fourier-transform infrared
HAADF-STEM	High-angle annular dark-field scanning transmission electron microscopy
LED	Light-emitting diode
LN ₂	Liquid nitrogen
LSPR	localized surface plasmon resonance
LUMO	Lowest unoccupied molecular orbital
MACS	Matrix assembly cluster source
MCP	Microchannel plate detector
ML	monolayer
NG	Noble gas
PEMFC	Low temperature proton exchange membrane fuel cells
PES	Photon-electron spectroscopy
PID	Proportional-integral-derivative
PSV	Pulsed supersonic valve
QMS	Quadrupole mass spectrometer
QMF	Quadrupole mass filter
RBS	Rutherford backscattering spectrometry
Refl-XAFS	Reflected X-ray absorption fine structure spectroscopy
RF	Radio frequency
RTof-MS	Reflectron time of flight mass spectrometer
SOFC	High temperature solid oxide fuel cells
STM	Scanning tunnelling microscope
TEY	Total-electron-yield
TNCs	Trimetallic nanoclusters
TNPs	Trimetallic nanoparticles
TPD	Temperature programmed desorption

TPR	Temperature-programmed reaction
UHV	Ultra-high vacuum
UV-Vis	Ultraviolet-visible
W/	With
W/O	Without
XANES	X-ray absorption near edge structure
XPS	X-ray photoelectron spectroscopy
Z	Atomic number

List of Symbols

Symbols	Description
M	Mass of a particle/cluster
v_0	Cluster initial velocity
q	Cluster charge
x	distance between cluster initial position to the second extraction grid
E_{1st} and E_{2nd}	First and second extraction grids
V_{E1} and V_{E2}	Pulsed voltages applied on first and second extraction grids
L_{E1}	Distance between first and second extraction grids
v_{E1}	Cluster velocity at the position of second extraction grid in extraction zone
t_{E1}	Cluster traveling time in between first and second extraction grids
v_{E2}	Cluster velocity at the position of grounded extraction grid in extraction zone
t_{E2}	Cluster traveling time in between second and grounded extraction grids
v_F	Cluster velocity in free fly zone
L_F	Length of free fly zone
t_F	Cluster traveling time in free fly zone
R_{2nd} and R_{3rd}	Second and third reflectron grids
V_{R2} and V_{R1}	Potentials applied on the second and third reflectron grids
t_{R2}	Cluster traveling time in between grounded and second reflectron grids
v_{R2}	Cluster velocity at the position of second reflectron grid in reflectron zone
y	Penetration depth between second and third reflectron grids
t_{R1}	Cluster traveling time in between second and third reflectron grids
t_{FD}	Cluster traveling time in between grounded first reflectron grid to detector
E_i	Kinetic energy of incident projectile particle
E_t	Kinetic energy of target particle
E_t'	Kinetic energy loss after collision
E_s	Kinetic energy of backscattered projectile particle
θ	Backscattered angle
K	Kinematic factor
$\sigma(\theta)$	Scattering cross section of elements at the angle θ
Ω	Solid angle of the detector
N	Number of particles
I	HAADF intensity of elements

$E_{kinetic}$	Kinetic energy of a photoelectron as measured by an energy analyser
$h\nu$	Energy of X-ray photons
ϕ	Work function of the energy analyser
I_0	The photoelectron intensity from the origin
I_d	The intensity of the emitted photoelectron
d	Distance between the origin of photoelectron to vacuum
λ_E	Inelastic mean free path as a function of electron kinetic energy
ρ	Sample density
$\mu(E)$	Oscillating portion of the X-ray absorption coefficient
$\mu_0(E)$	Isolated-atom X-ray absorption
$\chi(E)$	Modulated X-ray absorption
μ_{exp}	Measured X-ray absorption signal
$\Delta\mu_{exp}$	Edge jump through extrapolation of the pre- and post-edge lines
μ_{bg}	Smooth background spline function fitted through the data
$A_j(k)$	Amplitude function of EXAFS
$\sin[\Phi_j(k)]$	The oscillation function of EXAFS
S_0^2	Amplitude reduction factor
$F_j(k)$	Theoretical backscattering amplitude function
$e^{-2k^2\sigma^2}$	Debye–Waller factor
$e^{\frac{-2R_j^2}{k\lambda(k)}}$	Amplitude loss resulting from photoelectron inelastic scattering
N_{ip}	Independent parameters
$r_d(\theta)$	Molecule desorption rate
A	Total area of the sample surface
n_a	Number of adsorption sites per area
θ	Molecule coverage
$\nu(\theta)$	Pre-exponential factor
m	Order of desorption
$E_d(\theta)$	Activation energy for desorption
K	Ideal gas constant
T	Temperature of a sample
T_0	Initial temperature of a sample
β	Heating rate of temperature programmed desorption
T_{max}	Temperature of maximum rate of desorption

List of Figures

Figure 2.1 Top view schematic drawing of the laser ablation cluster setup. The detector is located at higher level in the deposition chamber. The cluster beam is bended up to the position of the detector when voltages are applied on the deflector. Details are not to scale. 10

Figure 2.2 Time sequence of the cluster formation process. Pulsed He is released in the chamber at t_0 . When the He pulse reaches the first target metal plate, t_1 , the first laser is triggered and the second laser is triggered to ablate the second target metal plate as the He pulse reaches the position of second target metal plate, t_2 10

Figure 2.3 Mass spectra of (a) Au nanoclusters in the few-atom size region, (b) main production region of the laser ablation cluster source and (c) mass-selected nanoclusters for different bending voltages from 100 V (purple) to 300 V (dark red). 12

Figure 2.4 Mass spectra of Au_xAg_{1-x} with $x = 0.1, 0.3, 0.5, 0.7, 0.9$ bimetallic nanoclusters produced by ablating Au_xAg_{1-x} alloy targets in the mass range from 1000 u to 2000 u. The red peaks are the simulated distributions of the decamer according to the composition of the alloy targets with binomial combinatorial calculations. 12

Figure 2.5 Top view schematic drawing of the magnetron sputtering setup. 14

Figure 2.6 Schematic drawing of the magnetron sputtering source chamber. 14

Figure 2.7 Au mass spectra nanoclusters produced by variation of various parameters: aggregation distance in cm (a), He to Ar gas flow in sscm (b), plasma power in watt (c) and total pressure of the buffer gases in mbar (d). 15

Figure 2.8 Mass spectra of Au nanoclusters produced by the magnetron sputtering source and scanned by the RF quadrupole mass filter with 330 kHz frequency generator. Mass spectra with different mass selection conditions are showing with different colour from red to brown. 16

Figure 2.9 STEM images of Au_{20} , Au_{34} , Au_{58} and Au_{500} nanoclusters produced by magnetron sputtering source and deposited on carbon TEM grids with carbon capping layer. 17

Figure 2.10 Top view schematic drawing of the matrix assembly cluster source. 18

Figure 2.11 Illustration of the MACS process. 18

Figure 2.12 STEM images of Au _{0.75} Ag _{0.25} , Au _{0.5} Ag _{0.5} and Au _{0.25} Ag _{0.75} nanoclusters on carbon TEM grids.	19
Figure 2.13 Schematic drawing of two stages reflectron time-of-flight mass spectrometer used in laser ablation cluster setup.	21
Figure 2.14 ToF spectrum of Au nanoclusters from Au ₁ to Au ₄₈ (a). Mass of the Au _N nanoclusters plotted as a function of time-of-flight (b) and mass root as a function of time (c).	24
Figure 2.15 Illustrations of a general RBS allocation (a) and mechanism of RBS on an elastic collision between a projectile ion and a target atom.	25
Figure 2.16 RBS spectra of trimetallic CuAgAu nanoclusters produced from MACS with different compositions.	26
Figure 2.17 Schematic drawing (a) and the mechanism of HAADF-STEM (b).	27
Figure 2.18 Illustration of X-ray photoelectric effect, the principle of X-ray photoelectron spectroscopy.	29
Figure 2.19 Schematic drawing of a typical experimental arrangement of XPS.	31
Figure 2.20 Schematic drawing of a typical experimental arrangement of Refl-XAFS.	32
Figure 2.21 Schematic drawing of decay mechanisms of the excited atomic state: X-ray fluorescence (a) and the Auger effect (b).	33
Figure 2.22 Schematic drawing of the constructive (top row) and destructive (bottom row) interferences of outgoing photoelectron wave and the backscattered electron wave.	34
Figure 2.23 Illustration of the absorption signal, edge jump extrapolated from the pre- and post-edge lines and the spline function of the absorption background.	35
Figure 2.24 Schematic drawing of the gas flow reactor.	37
Figure 2.25 Schematic drawing of the temperature programmed desorption.	38
Figure 2.26 Illustration of zero order desorption mechanism (a) and desorption curves of zero order desorption with different coverages.	39
Figure 2.27 Illustration of first order desorption mechanism (a) and desorption curves of first order desorption with different coverages.	40
Figure 2.28 Illustration of second order desorption mechanism (a) and desorption curves of second order desorption with different coverages.	41

Figure 2.29 Top view (a) and a side view (b) of the TPD setup.	42
Figure 2.30 Schematic drawing of the sample holder with side, front and bottom views.	43
Figure 2.31 Schematic drawing of the sample holder with side and front views as well as a front view with sample holder in the sample slot.	44
Figure 3.1 Full RToF mass spectrum of Au_xAg_{1-x} nanoclusters taken from Au-Ag alloy target 35 at% Au and 65 at% Ag from few atoms region to the main production region.	48
Figure 3.2 RToF-MS of deposited Au_xAg_{1-x} nanoclusters, (a) and (b) mass spectra of 73.8 ± 0.4 at% Au and 26.2 ± 0.4 at% Ag as well as 35.9 ± 0.7 at% Au and 64.1 ± 0.7 at% Ag combined with simulation spectra.	50
Figure 3.3 Validation of the fitting based on binomial theorem composition analysis method was done with additionally compositions obtained from the analysis of the mass spectra within the mass range from 600 u to 3000 u (4 atoms to 30 atoms) of a series Au_xAg_{1-x} nanoclusters produced from Au_xAg_{1-x} alloy targets of known stoichiometries ($x = 0.1, 0.3, 0.5, 0.7$ and 0.9). It is showed always a very good agreement with the target composition. The corresponding composition fitting are shown above in the mass range from 600 u to 3000 u, $x = 0.9$ (a), 0.7 (b), 0.5 (c), 0.3 (d) and 0.1 (e).	51
Figure 3.4 RBS spectra of deposited Au_xAg_{1-x} BNCs from gold rich to silver rich on SiO_2 wafers. The inset table shows the overall composition of deposited nanoclusters as determined by RBS.	51
Figure 3.5 k^3 weighted XAFS spectra of the Au_xAg_{1-x} BNCs on SiO_2 wafers from $x = 0.9$ to 0.1 . The corresponding phase-corrected Fourier transformed EXAFS spectra are shown in Figure 3.10-a.	54
Figure 3.6 STEM images and histograms of diameter distributions of Au_xAg_{1-x} BNCs: (a, e) $Au_{0.9}Ag_{0.1}$; (b, f) $Au_{0.7}Ag_{0.3}$; (c, g) $Au_{0.3}Ag_{0.7}$; (d, h) $Au_{0.2}Ag_{0.8}$	55
Figure 3.7 Example of detailed HAADF-STEM images of Au_xAg_{1-x} BNCs with simulation results also shown alongside: (a, f) $Au_{0.9}Ag_{0.1}$; (b, g) $Au_{0.7}Ag_{0.3}$; (c, h) $Au_{0.5}Ag_{0.5}$; (d, i) $Au_{0.4}Ag_{0.6}$; (e, j) $Au_{0.2}Ag_{0.8}$. The HAADF-STEM radial intensity profiles are taken from the center to the edge of the cluster and integrated from 0° to 360° . The red dash lines are the simulations of cluster STEM intensity with gradient composition evolution. The grey dotted lines and grey dash dotted lines are simulated STEM intensities with pure Au nanoclusters and pure Ag nanoclusters, respectively.	56

Figure 3.8 O 1s, Ag 3d and Au 4f XPS spectra of the Au_xAg_{1-x} BNCs on SiO_2 wafers from $x = 0.9$ to 0.1 . The green dash lines are the Shirley backgrounds, the blue lines are pure phase of Au and Ag and the grey lines are the Au-Ag alloy phases.58

Figure 3.9 Integrated peak area ratio of the XPS of Ag(0), pure phase, to Ag(δ), alloy phase, (black square) plotted with those of Au(0), pure phase, to Au(δ), alloy phase, (red circle) from Au rich to Ag rich BNCs compositions.59

Figure 3.10 (a) Phase-corrected Fourier transformed XAFS spectra from gold rich to silver rich nanoclusters. Bond distances of Ag-Ag (b) and Ag-Au (c), and Ag coordination fraction (Ag coordination number over the sum of Ag and Au coordination numbers) as a function of composition (d)..... 60

Figure 3.11 AFM images and height histograms of the 0.1 ML Au-Ag BNCs with different composition, $Au_{0.9}Ag_{0.1}$ (a,d), $Au_{0.6}Ag_{0.4}$ (b,e), $Au_{0.2}Ag_{0.8}$ (c,f) deposited on SiO_2 wafers. 61

Figure 3.12 XANES spectra of gold-rich $Au_{0.9}Ag_{0.1}$ and $Au_{0.7}Ag_{0.3}$ BNCs along with Ag foil reference. 62

Figure 3.13 (a) DFT calculations of the mixing energy of tetramers: Ag_4 , Au_1Ag_3 , Au_2Ag_2 , Au_3Ag_1 , and Au_4 . RTof-MS peak intensity difference of the relative abundance of trimers to hexamers, which are calculated from $Au_{0.4}Ag_{0.6}$ and $Au_{0.7}Ag_{0.3}$ RTof-MS. Vertical dash lines represent the global compositions and the 0 in y-axis corresponds to no abundance difference between the experimental and simulated MS (b). The corresponding RTof-MS of $Au_{0.7}Ag_{0.3}$ and $Au_{0.4}Ag_{0.6}$ with binomial combinatorial calculations of trimer (red), tetramers (orange), pentamer (green) and hexamer (blue) are shown in (c) and (d), respectively. 64

Figure 3.14 Schematic representation of the 4-step growth process of Au-Ag nanoclusters in the gas-phase before deposition: (I) Au and Ag atoms are generated by laser ablation of the targets; (II) ultra-small BNCs form and the minority element is depleted from the metal gas; (III) the small BNCs serve as embryos or building blocks for the further growth of nuclei/seeds and the majority element atoms also condense on the bimetallic core to form the cluster shell; (IV) formation of nanoclusters, with alloy cores enriched by the minority element and shell enriched by the majority element. A full alloy is formed in $Au_{0.5}Ag_{0.5}$ 66

Figure 4.1 CO_2 production of 4 deposition areas of 1 ML Au_xAg_{1-x} ($x = 0.4, 0.5, 0.9$) BNCs supported by 2 cm \times 2 cm SiO_2 wafer in the first of reaction cycle of CO oxidation (a), second reaction cycle in the inset panel (a) with the first reaction

cycle results shown in small dots for comparison. Catalytic activity of powder supported Au _{0.5} Ag _{0.5} BNCs on SiO ₂ wafer and TiO ₂ (b).....	71
Figure 4.2 STEM images of the Au _{0.75} Ag _{0.25} , Au _{0.5} Ag _{0.5} and Au _{0.25} Ag _{0.75} nanoclusters on MgO powders.	73
Figure 4.3 RBS spectra of deposited Au _x Ag _{1-x} BNCs from gold rich to silver rich on MgO powders.	73
Figure 4.4 Production of CO ₂ and the consumption of CO in the first (a) and second (b) reaction cycles with MgO supported Au _x Ag _{1-x} BNCs.....	74
Figure 5.1 STEM images and histograms of diameter distributions of Pt _x Ni _{1-x} BNCs: (a, f) Pt _{0.9} Ni _{0.1} ; (b, g) Pt _{0.7} Ni _{0.3} ; (c, h) Pt _{0.5} Ni _{0.5} ; (d, i) Pt _{0.3} Ag _{0.7} ; (e, j) Pt _{0.1} Ag _{0.9}	82
Figure 5.2 Examples of HAADF-STEM images of Pt _x Ni _{1-x} BNCs: (a, d) Pt _{0.7} Ni _{0.3} ; (b, e) Pt _{0.5} Ni _{0.5} ; (c, f) Pt _{0.1} Ni _{0.9} . The HAADF-STEM radial intensity profiles (d, e, f) are taken from the centre to the edge of the cluster and integrated from 0° to 360°. The red dash lines correspond to simulations of cluster STEM intensity profiles with gradient composition evolution. The light grey dotted lines and dark grey dash lines are simulated STEM intensities with pure Pt nanoclusters and pure Ni nanoclusters, respectively.....	83
Figure 5.3 DFT calculations of the mixing energy of tetramers: Ni ₄ , Pt ₁ Ni ₃ , Pt ₂ Ni ₂ , Pt ₃ Ni ₁ , and Pt ₄	83
Figure 5.4 Methanol desorption from the cleaned amorphous SiO ₂ surface for selected masses stemming from cracking: CD ₃ OD, CO, CD ₄ , D ₂	84
Figure 5.5 TPD spectra of methanol decomposition on Pt _x Ni _{1-x} BNCs of different compositions on SiO ₂ supports, showing the desorption of (a) CO and (b) D ₂ . Overviews of the (c) CO and (d) D ₂ desorption temperatures as a function of the Ni fraction in the BNCs.	86
Figure 5.6 Pt 4f (a) and Ni 2p (b) XPS spectra of the Pt _x Ni _{1-x} BNCs on SiO ₂ wafers from x = 0.9 to 0.1 with pure Pt and Ni NPs. The Pt 4f peaks of Pt 4f _{7/2} and Pt 4f _{5/2} are deconvoluted into Pt metal phase (71.3 eV and 74.6 eV) and Pt oxide phases (72.4 eV, 75.7 eV, 73.8eV and 77.1 eV); the Pt 4f XPS intensity ratio of the oxide phase is summarized in (c). The Ni 2p peaks of Ni 2p _{3/2} and Ni 2p _{1/2} are deconvoluted into a Ni metal phase (852.5 eV and 869.6 eV) and Ni hydroxide/oxide phases (853.2 eV, 870.7 eV, 855.9 eV, 873.4 eV, 860.7 eV, 878.0 eV, 863.6 eV and 880.8 eV); the Ni 2p XPS intensity ratio of the oxide phase is summarized in (d).	87

- Figure 5.7 nanoclusters with smaller (100) surface was modelled with $\text{Pt}_{417}\text{Ni}_{144}$ nanocluster using Wulff construction (a) and $\text{Pt}_{353}\text{Ni}_{106}$ nanocluster with larger (100) surface (b). The CO adsorption on bridge sites are also illustrated. The grey, green, dark grey, and red balls represent, Pt, Ni, C, and O atoms, respectively. .88
- Figure 5.8 Plot of the d-band population and CO binding energy on the Pt atom at the (111) surface of the $\text{Pt}_{353}\text{Ni}_{106}$ and $\text{Pt}_{417}\text{Ni}_{144}$ cluster with Pt or Ni subsurface atoms (blue cycles). The linear fit is presented as a dashed red line. 90
- Figure 6.1 SEM images of Si wafers supported TiO_2 P25 (a). Gas phase Au cluster modified P25 films with 2 ML (b), 4 ML (c) and 8 ML (d) equivalent coverage as well as size distribution histograms of 2 ML (e), 4 ML (f) and 8 ML (g) samples. The red dash lines in the histograms are the fittings of cluster distributions. 97
- Figure 6.2 UV-Vis absorption spectra of 2 ML (black), 4 ML (red) and 8 ML (blue) AuNCs on TiO_2 films, with a pristine TiO_2 film as the background sample..... 98
- Figure 6.3 Evolution of integrated FTIR absorbance of stearic acid between 2800 to 3000 cm^{-1} as a function of illumination time on the sample of pristine TiO_2 P25 film (blue ■) and Au cluster modified TiO_2 P25 films with 2 ML (yellow ●), 4 ML (grey▲) and 8 ML (orange ◆) Au coverages under (a) UV and (b) green light illumination. 99
- Figure 6.4 *FQE* under (a) UV and (b) green light illumination as a function of Au cluster coverage on TiO_2 P25. 99
- Figure 6.5 Schematic illustration of hot electron transfer from an excited plasmonic state on the gold nanoparticle, to the TiO_2 conduction band. Modified from reference.²¹² 101
- Figure 7.1 Simulated mass spectra within the mass range from 600 u to 2000 u (4 atoms to 15 atoms) of a series Au-Ag-Cu nanoclusters from Au rich $\text{Au}_{0.5}\text{Ag}_{0.25}\text{Cu}_{0.25}$ (a), Ag rich $\text{Au}_{0.25}\text{Ag}_{0.5}\text{Cu}_{0.25}$ (b) and Cu rich $\text{Au}_{0.25}\text{Ag}_{0.25}\text{Cu}_{0.5}$ 105

List of Tables

Table 2.1 Parameters of magnetron sputtering cluster source for cluster formation from few atoms to thousands of atoms sizes	15
Table 2.2 Parameters of the ion optics for charged cluster transfer from the source chamber to the deposition chamber.	17
Table 2.3 Comparison of the laser ablation, magnetron sputtering and matrix assembly cluster sources.	20
Table 3.1 Summary of structural results of Ag K-edge XAFS refinements of Au-Ag BNCs on SiO ₂ wafer measured in full reflection and fluorescence-detection mode.	53
Table 5.1 Summary table presenting the charge of Pt and Ni atoms using Hirchfeld, Bader, Löwdin and Mulliken analysis methods. The Mulliken analysis was not performed for the larger nanocluster. The unit of transferred charge presented here is elementary charge.....	89
Table 5.2 Summary table of d-electron population calculation based on the Löwdin and Mulliken methods. The <Ni> and <Pt> are the averages value of Ni or Pt atoms in the nanoclusters and Pt/Ni (Pt/Pt) denotes Pt atoms on the 111 surface (results for Pt on the (100) surface is given for the larger nanocluster), with a Ni or Pt subsurface atom. The Pt/X numbers are an average of few sites. The Mulliken analysis was done only for the Pt ₃₅₃ Ni ₁₀₆ nanocluster.....	89
Table 5.3 Summary table of the CO-Pt binding energies of Pt atoms on various sites. Some of the sites with no number given are either unstable or have not been calculated. The unit of CO-Pt binding energy here is eV.	89

Chapter 1

Introduction

Nanoparticles/nanoclusters (NPs/NCs) are basic materials in the universe. NPs with size range from few nanometres up to few hundred nanometers are the most abundant constituents of the interstellar medium.¹⁻⁴ The aggregation of these interstellar nanoparticles was the first step in the formation of stars and planets. Nanoscale particles also widely exist on the Earth surface in natural environments and are produced by microbial metabolism,⁵ volcano eruptions,⁶ and disintegration of meteorites.⁷ These nanoparticles have a great influence on the chemical reactions happening in nature.⁶ In human history, the usage of nanoparticles can be dated back to several early civilizations, with prominent examples such as the Lycurgus Cup (4th-century, Roman), lusterware tiles (9th-century, Mesopotamia) and Jun glazed porcelains (10th-century, Song Dynasty).⁸⁻⁹ In the mid-20th-century, the concept of nanotechnology was first provided by Professor Richard Feynman in his famous lecture “There's Plenty of Room at the Bottom”.¹⁰ The possibility of imaging and designing nanoparticles was realized by the invention of electron microscopes.¹¹⁻¹² Thereafter, researchers have started to produce various types of nanoparticles and manipulate their properties, initiating the development of the nanotechnology field.

Today, after three decades of investigations and developments, many important technologies such as automobile catalytic converters, oxidation catalysis, self-cleaning surfaces and biomedical engineering rely upon the catalytic properties of NPs and NCs.¹³⁻¹⁵ Therefore, with the rapid growth in NPs and NCs demand, a large number of chemical,¹⁶ biological,⁵ and physical¹⁷ synthesis protocols have been developed. Contrarily to physical approaches, chemistry and biology synthesis methods can provide suitable amounts of nanoparticles for industrial applications. Despite being still far from massive production, physical synthesis produces unmatched size, composition and structural controlled ligand-free NPs and NCs. This opens up new opportunities to perform more fundamental investigations on better defined systems, to get a better understanding of the origin of NPs and NCs catalytic properties. This is crucial to design new tailored high performance catalysts with enhanced reactivity, selectivity and stability.

1.1 Synthesis of composition and structure controlled nanoclusters

The key components of a cluster source are on one hand the metal atoms and rare gas sources and on the other hand the cluster aggregation zone. Several methods are

available to remove metal atoms from a metal target surface, such as laser ablation, magnetron sputtering and thermal evaporation methods while, in these cluster sources, the rare gas is injected into the chamber by a continuous flow or a pulsed mode for the cluster formation. The basic principle of gas phase cluster sources relies on the three body collision between metal atoms and rare gas atoms to remove the extra energy of the metal atoms to form nanoclusters. By controlling the cluster formation conditions, such as the temperature, the gas pressure and the concentration of metal atom, the particle size can be fine-tuned.

Alloying two elements into a bimetallic nanocluster (BNCs) allows further fine-tuning its properties through the composition and atomic structure. Composition controlled BNCs can be synthesized via a cluster source either by using a single alloy target or two pure targets of the two elements and applying adequate laser ablation/sputtering powers to generate BNCs with the required compositions. BNCs have been produced by laser ablation cluster sources with a single alloy target,¹⁸⁻¹⁹ dual-target sources using a split ablation laser²⁰ and dual-target dual-laser sources.²¹⁻²² Although the single alloy target approach is the simplest method to produce BNCs, it lacks composition flexibility as the BNC composition always reflects that of the alloy target.²³⁻²⁴ The dual-target with a split ablation laser generally provides a better control of the BNC composition by the split laser power, however it does not allow fine-tuning the ablation time and laser power on the two targets since only one laser is used. Last, the dual-target dual-laser combination provides the highest flexibility on controlling the sequence of targets ablation, the ablation time and the laser power on the targets. Therefore, not only the composition of the BNC can be controlled, but also its spatial structure via sequential ablation and adequate selection of the ablation time between the two lasers. This allows forming either mixed alloy nanoclusters, core-shell BNCs with the first element forming the core and second element the shell of the nanoclusters or arrangements governed by its formation mechanism.

BNCs can be successfully produced in cluster sources containing either a single magnetron, multiple magnetrons in plane or multiple magnetrons with position adjustable design. In the single-magnetron design, the BNCs can be obtained by using one magnetron sputtering head to sputter one alloy target and a target composed of two/multiple elements with different sputtering areas;²⁵⁻²⁶ the BNC composition from a single alloy target method is limited by the target composition and the composition of BNC can be varied by a combined target with two/multiple elements with different areas, however, the chamber has to be vented to change the target to obtain BNC with different composition. In-plane multi-magnetron sputtering provides a high level of control on the BNC composition by varying the sputtering power.²⁷⁻²⁹ Position adjustable multi-magnetron sputtering allows synthesizing BNCs with more flexibility on the BNC structure.³⁰ By fine-tuning both the sputtering power applied on each metal target and the

position of each magnetron sputtering head, homogenous alloys, single core-shell, alloy-core-pure-shell and core-multi-shell BNC structures can be obtained.³¹

1.2 Tuning the properties of nanoclusters

Four main factors are influencing the physical and chemical properties of BNCs which are the size, the composition, the chemical ordering within the nanoclusters and the cluster-support interaction.³²⁻³⁴ In order to design a better catalyst, understanding at the atomic level of the synergy between the two chemical elements through an accurate control of the size and the composition of the BNCs obtained in the two types of cluster sources introduced in the aforementioned section is essential. Systematic investigation of the different sizes and compositions of nanoclusters deposited on various supports can contribute to a better fundamental understanding of the catalytic properties influenced by their size, synergistic and support effects. Since the discovery of the size effect of Au nanoparticles on their catalytic activity by Haruta,³⁵ a new approach to design catalysts has been inspired and the size effect of nanoclusters has received a tremendous interest. Although Au has long been considered as an inert material, Haruta found that supported Au and Pt nanoclusters show comparable CO oxidation as well as excellent hydrogenation ability.³⁵

Size-dependent catalytic activity of few-atom Au nanoclusters was also investigated on mass-selected Au_n nanoclusters by quadrupole ion guides and deposited on various oxide supports. A strong size dependence of the CO oxidation activity was found on Au_n /rutile $TiO_2(110)$ ($n = 1 - 7$); only Au_3 , Au_4 , and Au_7 were efficient catalysts and this size dependency was attributed to ability of these nanoclusters of to bind oxygen.³⁶ The CO oxidation catalytic activity of $Au_n/MgO(100)$ ($n = 2 - 20$) was found to be strongly dependent on the abundance of defects and oxygen vacancies on the MgO support.³⁷ Au_8 on defect rich $MgO(100)$ was found to be the smallest active catalyst, while no catalytic activity was found on defect poor MgO supported Au_8 system. The defect site of MgO can provide extra charge to Au nanoclusters, that can activate both oxygen and CO molecules adsorbed on them. In these two cases, CO oxidation activity is not only influenced by the cluster size but also by the support effect. When supported on rutile $TiO_2(110)$, Au nanoclusters are active for all sizes larger than Au_3 , while the activities vary non-monotonically with the cluster size.³⁶ Au nanoclusters from Au_8 to the largest investigated Au_{20} nanoclusters show a pronounced activity on defect rich $MgO(100)$, while no catalytic activity can be found on defect free $MgO(100)$ and a thin Au film.³⁷

Another example of the cluster size effect on their CO oxidation catalytic activity is provided by Pd_n ($n = 1, 2, 4, 7, 10, 16, 20$, and 25) nanoclusters supported on $TiO_2(110)$.³⁸ A non-monotone variation of the cluster activity as a function of its size is revealed while

$\text{Pd}_{20}/\text{TiO}_2(110)$ is found to be the most active catalyst; this size-dependent catalytic activity is correlated with the valence electronic structure of the nanoclusters. Furthermore, a support effect on Pt_7 nanoclusters on low reduction state TiO_2 (LR- TiO_2) and high reduction state TiO_2 (HR- TiO_2) was unravelled with Pt_7 supported on LR- TiO_2 being the more active system. The quenched CO oxidation activity observed in the Pt/HR- TiO_2 system is due to a competition between of the absorption of O_2 on the Pt_7 nanoclusters that are oxidizing CO and the oxidation of the TiO_2 support.³⁹

In alloyed BNCs two additional parameters, i.e. the element type and the composition, need to be considered when fine-tuning the properties of nanoclusters. The role of these two parameters have been extensively investigated in Au-based BNCs/bimetallic nanoparticles (BNPs) active as CO oxidation catalysts such as Au-Cu, Au-Ag and Au-Sr BNCs/BNPs on various supports produced by chemical and physical methods with particle sizes in few nm range. Au-Cu BNPs of 3.0 - 3.6 nm⁴⁰ on silica gel supports, produced chemically and physically, with a metal loading around 5.5 wt% showed a higher CO oxidation catalytic activity than monometallic gold catalysts. Even upon inclusion of a small fraction of Cu in the BNPs, the catalytic activity was highly enhanced at room temperature with a CO conversion reaching 100%. However, an activity valley was observed in most of the Au-Cu BNPs around 200 °C in which the temperature range (valley width) and the reduced activity (valley depth) were highly correlated with the Au-Cu composition, the valley being wider and deeper in Au rich BNPs. This was attributed to reaction switching between two pathways: CO oxidation reaction on Au sites at low temperature and O_2 activation on Cu sites at high temperature.⁴⁰ A similar system of 4 to 6 nm Au-Ag BNPs supported on mesoporous silica with 5 wt% metal loading under CO oxidation⁴¹ showed that the catalytic activity of bimetallic Au-Ag BNPs is much higher than their mono-metallic counterparts in the 300 - 380 K temperature range.⁴¹ $\text{Au}_{0.89}\text{Ag}_{0.11}$ (Au/Ag = 8/1) BNPs provided the best CO oxidation catalytic activity with an activity onset at around 250 K.

The catalytic activity towards CO oxidation studied by temperature-programmed reaction (TPR) of Au_n and Au_nSr ($n = 1 - 8$) nanoclusters soft-landed by cluster beam deposition (CBD) on $\text{MgO}(100)$ thin film⁴² showed that Au_8 is the smallest Au cluster that can catalyse the CO oxidation reaction, while Au_4 is catalytically inert.³⁷ DFT calculations showed that the cluster size-dependent catalytic activity can be correlated with their d band electronic structure.⁴² The low catalytic activity of Au_4 is attributed to the narrower d band of the O_2 adsorbed Au_4 cluster compared to that of Au_8 with consequently a lack of overlap between the states at the bottom of the d band of the Au cluster and the O_2 states. However, when a single Au cluster atom is replaced by Sr, the resulting cluster Au_3Sr became active. Calculations showed that, with a single Sr atom doping, the bonding and activation of O_2 change significantly compared to that in the pure Au_4 . The O_2 binds mainly to the Sr atom of the Au_3Sr cluster, and this bonding is

characterized by a substantially higher adsorption energy and a significant weakening of the O-O bond.⁴²

1.3 Application of supported bimetallic nanoclusters/nanoparticles

In section 1.2, examples of chemical reactivity tuning of Au_n/MgO, Pd_n/TiO₂, Au-Cu BNPs on silica gel, Au-Ag BNPs on mesoporous silica and Au_nSr/MgO(100) towards CO oxidation reaction by their size, support and composition was introduced. In this section, few examples of the application of BNCs and BNPs to other catalytic and photocatalytic reactions will be reviewed and introduced.

1.3.1 Nanoclusters/nanoparticles as Catalysts

Methanol synthesis by CO₂ hydrogenation reaction was studied with Ni_xGa_{1-x} (x = 0.5 to 0.75) catalysts, which were prepared by incipient wetness impregnation and dried in air for 24 hours at 100 °C.⁴³ The total loading of nickel and gallium in the reduced catalyst was 17 wt%. The dried Ni-Ga/SiO₂ catalysts were prepared in three different ways to understand the relationship between structure and catalytic activity: reduced directly in a flow of pure hydrogen for 2 hours at 700 °C (a) or first calcined in stagnant air for 4 hours at 400 °C (b) or 700 °C (c) prior to reduction. The resulting particle size of the sample without calcination pre-treatment was the smallest (4.7 ± 1.2 nm); while the particle size of the samples with calcination pre-treatment was larger and depending on the calcination temperature: 5.2 ± 2.0 nm for the 400 °C sample and 8.8 ± 2.5 nm for the 700 °C sample. Catalytic measurements of series of Ni_xGa_{1-x} (x = 0.5 to 0.75) catalysts were performed with 25% of CO₂ and 75% of H₂ under atmospheric pressure in gas flow quartz reactors with reaction temperatures of 165 °C and 205 °C. Although the methanol production rate was higher at 205 °C, the selectivity of methanol production was 100% at 165 °C except for the Ni_{0.75}Ga_{0.25} composition. The maximum of methanol production was observed with the Ni_{0.675}Ga_{0.325} catalyst at both reaction temperatures. Preparation methods had also a significant effect, as non-calcined Ni_{0.75}Ga_{0.25} catalyst was the most active, followed by the catalyst calcined at 400 °C, while the catalyst calcined at 700 °C featured the lowest activity between 165 °C and 240 °C. It was concluded that the methanol synthesis reaction on Ni_{0.625}Ga_{0.375} nanoparticles could be structure sensitive. The smaller particles with higher fraction of low-coordinated sites (corners, kinks and step sites) on the surface showed higher catalytic activity.⁴³

1.3.2 Nanoclusters/nanoparticles as Photocatalysts

Photocatalytic reactions are catalytic reactions triggered by absorbed photons. Transition metal oxides and semiconductors, such as TiO₂, ZnO and III-V compound

semiconductors, are the most common heterogeneous photocatalysts.⁴⁴ The main factors that determine the photocatalytic properties of semiconductor-based photocatalysts are the band gap, the position of the conduction band and the valence band, the mobility of photo-generated charge carriers, and the material stability.⁴⁵ Among transition metal oxides and semiconductors, TiO₂ is one of the most promising photocatalyst towards water splitting and oxidation of organic compounds under UV light.⁴⁶⁻⁴⁷ However, its photocatalytic properties need to be improved significantly in the visible range, especially under green light that corresponds to the maximum output range of the Sun's total irradiance spectrum. In this section, application of several BNPs modified TiO₂ systems towards various reactions will be introduced.

Au-Cu modified TiO₂ powders produced by wet chemistry and reduced in H₂ were tested towards the photocatalytic isopropanol oxidation reaction.⁴⁸ Composition of the 3.4 nm BNPs was controlled by the respective fractions of the Au and Cu precursors whose loading was maintained at 1 mol%. The photocatalytic activity in the oxidation of isopropanol (2-propanol) to acetone with and without visible-light irradiation (Xe lamp, 450 - 800 nm, 16.8 mWcm⁻²) was tested at 298 K. Although nanoparticle modified TiO₂ showed a modest catalytic activity and produced acetone without visible-light irradiation, irradiation with visible-light strongly enhanced the catalytic activity of the Au rich photocatalysts, Au_{0.7}Cu_{0.3}/TiO₂ being the most active sample. Further increase of the Cu fraction resulted in a reduced activity. Both pure TiO₂ and Cu modified TiO₂ powders showed almost no reaction with and without visible-light irradiation. Similarly, light irradiation did not significantly enhance the catalysis activity of Au-Pt, Au-Pd and Au-Ag systems towards the photocatalytic isopropanol oxidation reaction. The enhancement of activity in the Au-Cu alloy catalyst observed under light irradiation was attributed to the reduction of the surface Cu²⁺ oxide promoted by the light absorption of the Au species located at the surface of the nanoparticles, that way avoiding the catalyst deactivation upon oxide formation.

Photocatalytic activities of TiO₂ supported Au-Pd BNPs towards H₂ production using various bioavailable chemicals such as ethanol, glycerol, ethylene glycol, 1,2-propanediol, glucose, and fructose were investigated under UV-LED irradiation (365 nm, photon flux = 4×10^{17} photons/s).⁴⁹ A series of Au-rich to Pd-rich Au-Pd nanoparticles with chemical arrangements ranging from random alloy to core-shell structures were prepared by a colloidal method and supported on TiO₂ powders. All the investigated compositions of 4 – 5 nm Au-Pd nanoparticles were active in the photocatalytic reaction with water-ethanol (25 vol%) solution. Both gas-phase and liquid-phase products were formed. The main gas phase products consisted in H₂ with trace amounts of CH₄, CO, and CO₂, whereas the liquid-phase products were CH₃CHO and CH₃COOH. Monometallic Pd/TiO₂ was more active than Au/TiO₂ and both Au-rich and Pd-rich TiO₂

supported BNPs presented a slightly lower catalytic activity compared to their monometallic counterparts. However, it was found that $\text{Au}_{0.25}\text{Pd}_{0.75}/\text{TiO}_2$ with Au-core-Pd-shell structure showed a remarkable photocatalytic activity in the H_2 evolution. Similar catalytic activity of the Au-Pd photocatalyst under H_2 evolution condition with other bioavailable chemicals was also found. DFT calculations based on the 147-atom icosahedral nanoclusters of Au, Pd, Au-core-Pd-shell and Pd-core-Au-shell showed that the unoccupied, energetically favourable, and physically accessible surface d-orbitals on the Au-core-Pd-shell BNPs were at the origin of their high activity.

1.4 Objective of this thesis

The applications of nanoclusters towards exhaust pollutants removal (1.2), fuel synthesis (1.3.1) and aerobic oxidation (1.3.2), presented in the aforementioned sections show that NCs are suitable catalysts to reduce the pollution level, lower the amount CO_2 in the atmosphere and convert photon energy to chemical energy. Hence, gaining the fundamental understanding of such nanocatalysts at the atomic level is key to design higher efficiency, better selectivity and longer life-time catalysts. The objective of this thesis is to produce and characterize series of novel gas-phase catalysts based on size-selected and composition-controlled bimetallic nanoclusters supported on various oxide surfaces for easing the pollution levels created by economic activities and also fulfilling the increasing energy demand to achieve a sustainable society.

In this thesis, exhaust pollutants removal, direct methanol fuel cell life time prolongation, and self-cleaning surface efficiency enhancement are the three main focuses for solving the major obstacles of achieving a sustainable society by using NCs and BNCs. In order to study the composition-based atomic arrangements and the synergistic effect of the two elements within BNCs on their catalytic properties, the first step of the investigation is to have a better control of the BNC composition prior to deposition. It is achieved by controlling the ablation laser powers and analysing the RTof mass spectra in real time (2.1.1, 2.2, 3.3). HAADF-STEM, XPS and EXAFS investigations were carried out to understand the BNC structure evolution as function of composition (Chapter 3). Composition controlled BNCs were deposited on various oxide supports and tested under CO oxidation reaction (Chapter 4) and methanol decomposition as well as CO desorption (Chapter 5) to study their catalytic properties as a function of their composition. Coverage-controlled metal modified TiO_2 surfaces were utilized as a model system to study the cluster support interactions and the photocatalytic improvement brought by metal modification (Chapter 6).

Chapter 2

Experimental setups and characterization techniques

In this chapter, various techniques and setups that were used in this doctoral thesis will be introduced: the three cluster synthesis techniques, electron microscopy, spectroscopic characterization techniques, and catalytic reaction setups.

2.1 Cluster beam deposition methods

Three types of cluster sources were used, which are the laser ablation cluster source^{22, 50-52} and the magnetron sputtering cluster setup⁵²⁻⁵⁴ in the Clusters and Laser Spectroscopy (CLASS) group, Laboratory of Solid State Physics and Magnetism (VSM), KU Leuven as well as the novel high flux matrix assembly cluster source⁵⁵⁻⁵⁷ developed in the Nanoscale Physics Research Laboratory (NPRL), University of Birmingham.

2.1.1 Laser ablation cluster setup

A schematic drawing of the laser ablation cluster setup is shown in Figure 2.1. This setup is composed of 4 chambers which are the source chamber for cluster production, the extraction chamber for mass selection and acceleration of charged nanoclusters, the deposition chamber for cluster deposition as well as cluster size, composition and flux determination and the load lock chambers for sample transfer.⁵⁰⁻⁵²

The nanoclusters are produced by pulsed laser ablation of plate targets and inert gas condensation. The source chamber is equipped with a fast pulsed valve to generate pulsed helium (He) beams and two Nd:YAG lasers which are synchronized by two delay generators. High pressure and high purity He pulses (pressure 9 bar, purity 99.9999%, duration 125 μ s, repetition rate 10 Hz) are sent into the source block by a pulsed valve. When the He pulses reach the target positions, the two lasers (wavelength 532 nm, duration 7 ns, repetition rate 10 Hz) are triggered sequentially and focused to 0.9 mm in diameter to ablate the two metal targets to generate hot metal vapour mixtures. By three-body collisions with He atoms, the hot metal atoms are cooled down to form nanoclusters. The time sequence of the cluster synthesis process with timing of the pulsed valve and the two lasers is schematically shown Figure 2.2.⁵⁰⁻⁵²

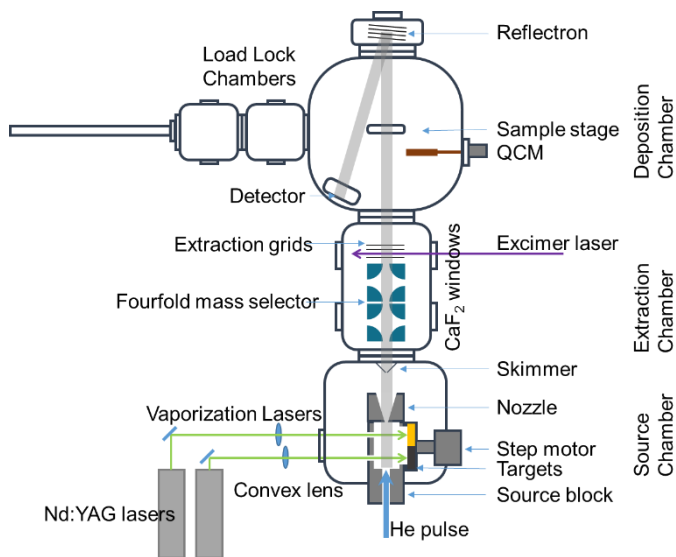


Figure 2.1 Top view schematic drawing of the laser ablation cluster setup. The detector is located at higher level in the deposition chamber. The cluster beam is bended up to the position of the detector when voltages are applied on the deflector. Details are not to scale.

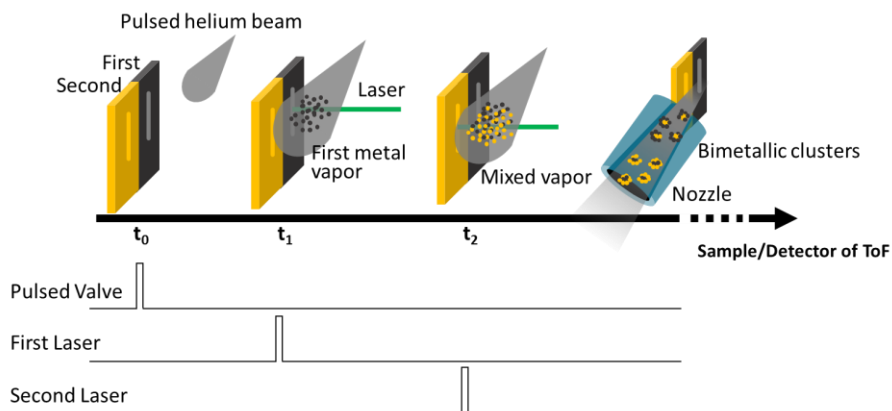
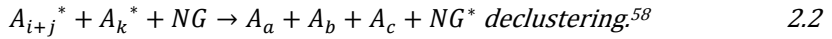
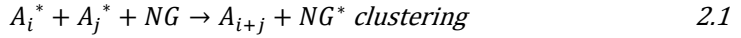


Figure 2.2 Time sequence of the cluster formation process. Pulsed He is released in the chamber at t_0 . When the He pulse reaches the first target metal plate, t_1 , the first laser is triggered and the second laser is triggered to ablate the second target metal plate as the He pulse reaches the position of second target metal plate, t_2 .

The cluster formation process requires three-body collisions for removing surplus thermal energy and to fulfil the conservation of energy and momentum. The dynamic processes are describe as



As described by the dynamic processes, the collisions between energetic particles, A^* , and noble gases, NG , can lead to cluster formation (2.1) or cluster dissociation (2.2) depending on the kinetic energy of the metal atoms/nanoclusters in the plasma and the binding energy of the atoms in the nanoclusters. As the kinetic energy of the metal atoms in the plasma is removed by NG and the kinetic energy is not sufficient to break the bonds, the cluster formation process starts. It starts from the formation of dimers and the dimers can serve as nuclei for further condensation. The cluster formation process of bimetallic nanoclusters is further discussed in Chapter 3.

The size distribution of the nanoclusters formed in the cluster source is in the range of few atoms to the order of 1000 atoms; the average cluster size can be tuned by the cluster formation conditions which are the He pressure, the temperature of the source block and the nozzle, and the laser power and timing. Larger nanoclusters can be formed by supplying a larger amount of atoms (upper limit of suitable laser power range),⁵⁹ with efficient cooling (source block and nozzle are cooled to LN_2 temperature) and laser triggering in between the central and the end (falling edge) of the gas pulse to ensure more collisions between He atoms and hot metal atoms as well as longer aggregation time in the source block.

The wavelength of the laser is set as 532 nm which is sufficiently high to ablate the target and eject hot atoms from the target surface without single photon ionization of the atoms. Therefore, most of the nanoclusters are neutral and only a small fraction of the nanoclusters is charged.⁵² The centreline of the cluster beam is extracted and collimated to the extraction chamber by a skimmer at the end of the source chamber. CaF_2 windows are installed in the extraction chamber, allowing the 157 nm F_2 excimer laser light to enter the chamber for ionizing the neutral nanoclusters. The charged nanoclusters can be mass selected by a fourfold electrostatic mass selector and/or accelerated by the ion optics in the extraction chamber of the reflectron time of flight mass spectrometer (RToF-MS) measurements. The working principle of RToF-MS is discussed in section 2.2. The spectrum shown in Figure 2.3-a is the F_2 laser ionized Au cluster spectrum from 1 atom to 100 atoms. The main production of the Au nanoclusters from the cluster source is shown in Figure 2.3-b and it is peaked around 64000 u and extends to 100000 u. The mass spectra of fourfold bender selected nanoclusters are presented in Figure 2.3-c with different bender voltages; the first mass peak is around 25000 u (125 Au atoms) and it is increased to 101000 u (505 Au atoms) with 4000 u increment for every spectrum.

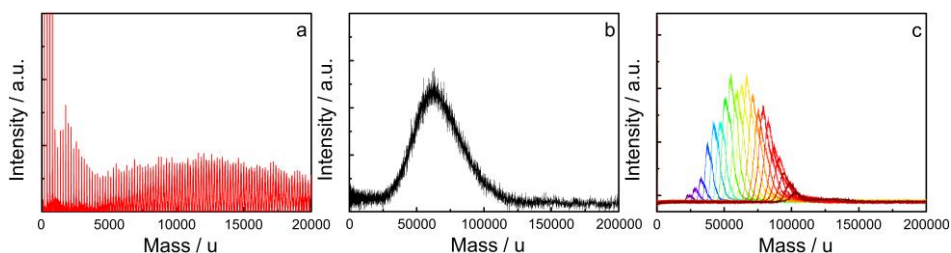


Figure 2.3 Mass spectra of (a) Au nanoclusters in the few-atom size region, (b) main production region of the laser ablation cluster source and (c) mass-selected nanoclusters for different bending voltages from 100 V (purple) to 300 V (dark red).

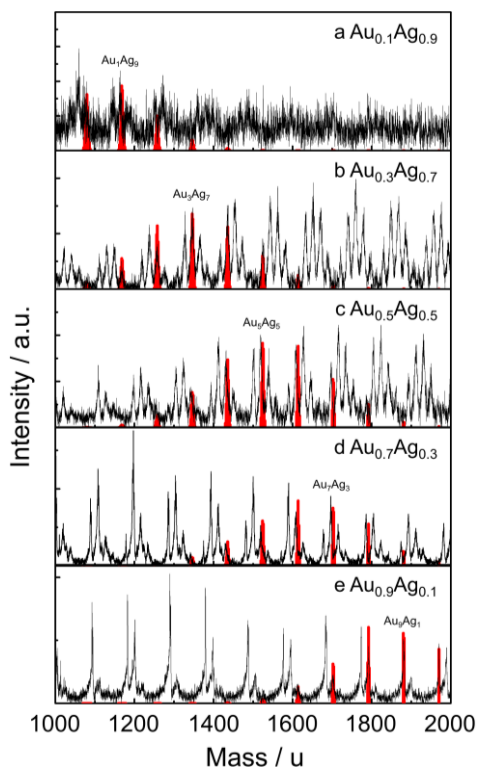


Figure 2.4 Mass spectra of $\text{Au}_x\text{Ag}_{1-x}$ with $x = 0.1, 0.3, 0.5, 0.7, 0.9$ bimetallic nanoclusters produced by ablating $\text{Au}_x\text{Ag}_{1-x}$ alloy targets in the mass range from 1000 u to 2000 u. The red peaks are the simulated distributions of the decamer according to the composition of the alloy targets with binomial combinatorial calculations.

Bimetallic nanoclusters can be produced by using either one alloy target (14 mm \times 24 mm \times 1 mm) or two metal targets (7 mm \times 24 mm \times 1 mm). With alloy targets, the composition of the produced nanoclusters is fixed and reflects the composition of the

alloy target.²³⁻²⁴ However, the composition of the produced nanoclusters can be controlled with the dual target dual laser approach by tuning the power of the two lasers. The normal power range of the two lasers is within 150 mW to 300 mW with 10 Hz repetition rate, or laser pulse energy of 15 mJ to 30 mJ. The amount of atoms generated by laser ablation is strongly dependent on the metal response to the laser, for instance the laser power required to ablate Ag rich targets is higher than the power for ablating Au rich targets. In general, however, the higher the power used, the larger the amount of ablated atoms. It was demonstrated that the mass spectrum of bimetallic nanoclusters produced by alloy targets reflects the targets composition well.²³ A series of $\text{Au}_x\text{Ag}_{1-x}$ bimetallic nanoclusters are produced by ablating alloy targets from Au rich to Ag rich ($x = 0.1, 0.3, 0.5, 0.7$ and 0.9) with typical mass spectra shown in Figure 2.4; the expected distribution of the Au_NAg_M ($N+M = 10$) nanoclusters are indicated by red simulation peaks and the most abundant decamers are labeled in each spectrum. More detail of the simulation method can be found in section 3.2. For instance, the most abundant decamer is Au_1Ag_9 in the spectrum taken by ablating the $\text{Au}_{0.1}\text{Ag}_{0.9}$ alloy target. The number of Au atoms increases in the decamer cases as the Au fraction increases. Consequently, control of cluster compositions is possible by changing the composition of the alloy target. More flexible composition control can be obtained when two elemental targets are used with two lasers for laser ablation. Composition control of $\text{Au}_x\text{Ag}_{1-x}$ bimetallic nanoclusters and the structure evolution as a function of composition is discussed in detail in Chapter 3.

2.1.2 Magnetron sputtering cluster setup

The magnetron sputtering cluster setup⁶⁰⁻⁶¹ is composed of a conventional gas aggregation DC magnetron sputtering source,⁶¹ ion guides chambers, a cluster deflection chamber, a radio frequency (RF) quadrupole mass filter, a deposition chamber, a preparation chamber and a load lock chamber. A schematic drawing of the magnetron sputtering setup is shown in Figure 2.5.

Different from the laser ablation cluster setup, the magnetron sputtering cluster setup is operated in a continuous mode. A schematic cross section view of the magnetron source is shown in Figure 2.6. A mixed Ar and He gas flow is introduced continuously by two flow controllers into the sputtering source chamber. By ionizing and accelerating the Ar ions with 200 to 400 eV to impact the target surface, the atoms of the target material are sputtered out from the target surface. Ionization of the Ar atoms is enhanced by trapping the free electrons generated during the sputtering process with a strong magnetic field, which enhances the sputtering efficiency. Therefore, this method is called magnetron sputtering.

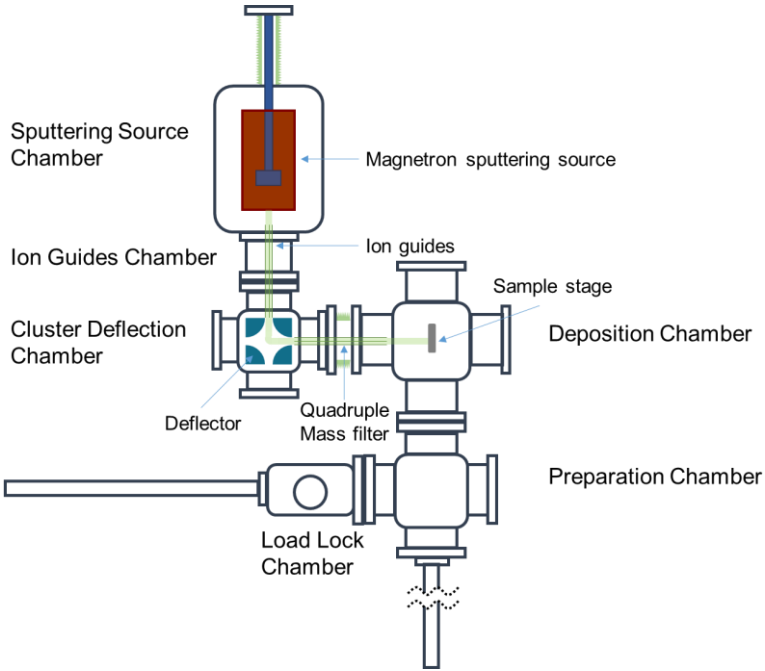


Figure 2.5 Top view schematic drawing of the magnetron sputtering setup.

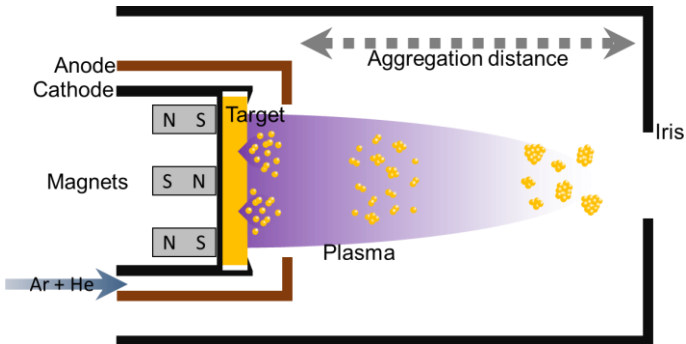


Figure 2.6 Schematic drawing of the magnetron sputtering source chamber.

Once the atoms of the sputtered target (5 cm in diameter \times 2 mm in thickness) are ejected, collisions between energetic target atoms and the buffer gases, such as Ar and He, cool down the atoms and the atoms start to aggregate into nanoclusters. The nanoclusters follow the gas flow to the exit of the condensation chamber and they grow from few atoms size up to thousands atoms. The size of the nanoclusters is determined by the number of atoms available and number of collisions during the cluster formation process. Therefore, the cluster size can be controlled by tuning the plasma power, the

buffer gas composition and pressure, the distance between the target and the exit of the aggregation chamber, and the temperature of the condensation chamber. In general, lower plasma power and lower Ar to He buffer gas ratio will make less atoms available for cluster formation and hence smaller cluster sizes. Also decreasing the Ar to He buffer gas ratio decreases the total pressure; and the shorter the aggregation length, the lower the number of collisions which also results in smaller size.⁶²⁻⁶³ Examples of Au spectra produced with different aggregation distance, He to Ar buffer gas ratio, plasma power and the total pressure of the buffer gases are shown in Figure 2.7. The typical used parameters for cluster formation are listed in Table 2.1.

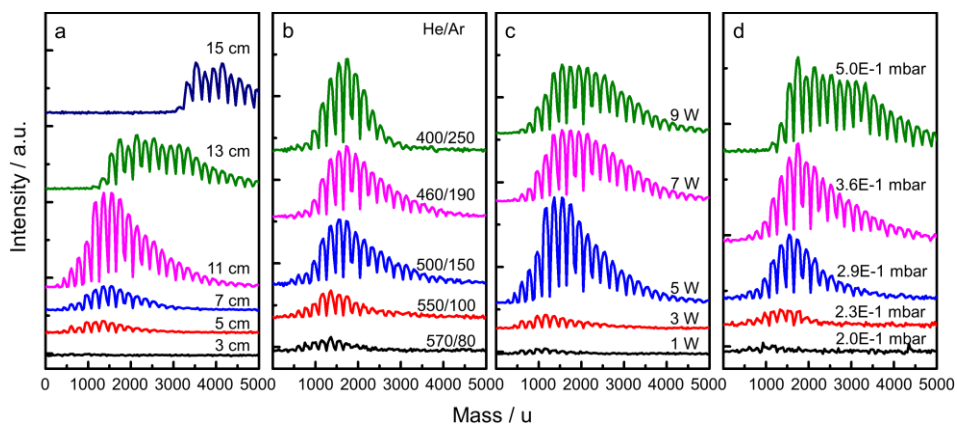


Figure 2.7 Au mass spectra nanoclusters produced by variation of various parameters: aggregation distance in cm (a), He to Ar gas flow in sccm (b), plasma power in watt (c) and total pressure of the buffer gases in mbar (d).

Table 2.1 Parameters of magnetron sputtering cluster source for cluster formation from few atoms to thousands of atoms sizes

Parameter	Value range	Unit
Plasma power	1 – 30	W
Ar flow	50 – 570	sccm
He flow	0 – 300	sccm
Pressure of the buffer gases	0.05 – 1	mbar
Aggregation distance	1 – 25	cm
Chamber temperature	300 – 80	K

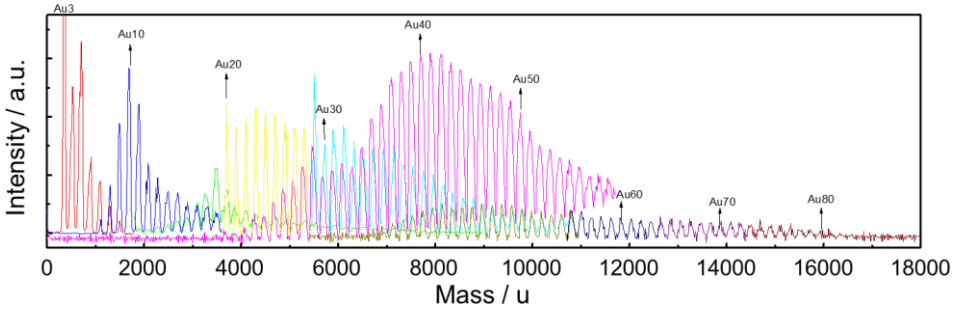


Figure 2.8 Mass spectra of Au nanoclusters produced by the magnetron sputtering source and scanned by the RF quadrupole mass filter with 330 kHz frequency generator. Mass spectra with different mass selection conditions are showing with different colour from red to brown.

Due to the sputtering process, a large fraction of nanoclusters is charged. Therefore, the nanoclusters can be extracted by applying a small voltage on the iris diaphragm at the exit of the aggregation chamber towards the ion guide chambers. With differential pumping, the pressure in the ion guide chambers is decreased to the 10^{-2} and 10^{-4} mbar range, respectively. The ion guides guide the charged nanoclusters by radio frequency (RF) voltages to the deflection chamber. The pressure further drops to 10^{-6} mbar in the deflection chamber. A DC quadrupole bender is utilized to deflect the charged cluster beam by 90° to the RF quadrupole mass filter (Ardara technology) for precise mass selection. The RF quadrupole can be operated in three different frequency modes depending on the mass range of interest: 1.1 MHz, 550 kHz and 330 kHz for cluster mass smaller than 1500 u, 5000 u and 18000 u, respectively. The nominal resolution of the quadrupole at 1.1 MHz is $M/\Delta M = 1000$. A higher mass resolution implies a lower throughput of the cluster flux. Therefore, during cluster deposition for a larger amount of nanoclusters, the maximum mass resolution of the RF quadrupole is set as $M/\Delta M = 200$ in the whole mass range, allowing cluster beams passing through the RF quadrupole with broader mass distribution, to obtain a realistic deposition time. Typical mass spectra of Au nanoclusters produced with the magnetron sputtering source and scanned by the RF quadrupole mass filter with 330 kHz frequency generators are presented in Figure 2.8. Since the mass selected nanoclusters are charged, the nanoclusters only can be deposited on vacuum compatible conducting or semi-conducting substrates, for charge compensation, in the deposition chamber with 10^{-10} mbar condition. The sample with deposited nanoclusters can be transferred to the preparation chamber for sample treatment, such as thin film carbon capping for cluster protection, and further transfer to the load lock chamber for sample exchange. The normal parameters of the voltages and frequencies applied on the ion optics and ion guides for cluster transfer from the aggregation chamber to the deposition chamber are listed in Table 2.2.

STEM images of Au₂₀, Au₃₄, Au₅₈ and Au₅₀₀ nanoclusters produced by the magnetron sputtering source and deposited on carbon TEM grids with a carbon capping layer are shown in Figure 2.9 and present the capability of the magnetron sputtering cluster source to produce a wide range of nanoclusters from 20 atoms to around 500 atoms.

Table 2.2 Parameters of the ion optics for charged cluster transfer from the source chamber to the deposition chamber.

Parameter	Value range	Unit
Voltage on iris	-20 – 20	V
Voltage on first ion guides	-10 – 10	V
Frequency of first ion guides	100 – 1000	kHz
Voltage on second ion guides	-20 – 20	V
Frequency of second ion guides	100 – 1000	kHz
DC quadrupole bender voltage	40 – 800	V

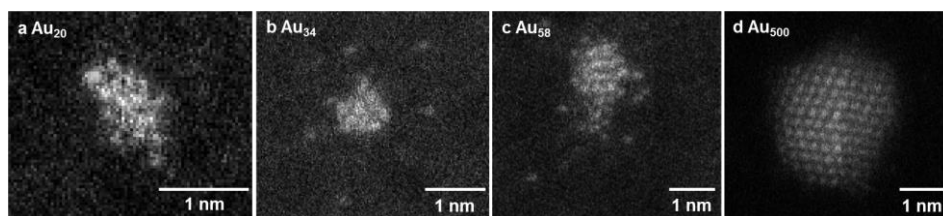


Figure 2.9 STEM images of Au₂₀, Au₃₄, Au₅₈ and Au₅₀₀ nanoclusters produced by magnetron sputtering source and deposited on carbon TEM grids with carbon capping layer.

2.1.3 Matrix Assembly Cluster Source

The nanoclusters are condensed and formed in gas phase in both the laser ablation cluster source and the magnetron sputtering cluster source. Both cluster sources use cooled carrier gases for condensing hot atoms into nanoclusters. The cluster formation principle of the matrix assembly cluster source (MACS), on the other hand, relies on removing the extra energy of the hot metal atoms and atom condensation by trapping them in a cryogenic noble gas matrix, which is a more effective three body collision method. This novel cluster source is currently capable of producing 100 nA of nanoclusters and has been developed by prof. Richard E. Palmer and coworkers at the University of Birmingham.^{56-57, 64} A schematic drawing of the MACS is shown in Figure 2.10. The setup is composed of two chambers, the source chamber with the cryogenic matrix support, Ar doser, metal evaporators and Ar⁺ beam sputtering source, and the

deposition chamber separated by a gate valve and a sample carousel with 21 sample slots located inside.

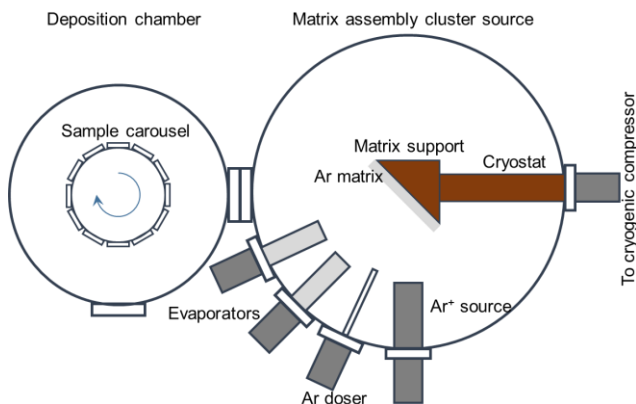


Figure 2.10 Top view schematic drawing of the matrix assembly cluster source.

The Ar dosage is fine-tuned and controlled by a leak valve and the pressure of Ar is kept around 5×10^{-6} Torr; the Ar gas is condensed onto a cryogenic compressor cooled matrix support and forms an Ar matrix. The metal atoms, such as Au and Ag, are generated by thermal evaporators with a fixed deposition rate to control the metal loading and the composition of the two metals in the Ar matrix. This pre-formed metal atom-Ar matrix is then bombarded by an Ar^+ ion beam, which applies extra energy that causes atomic diffusion and aggregation to form the nanoclusters of a desired size range. At the same time, the formed metal nanoclusters gain extra energy from the Ar ions and nanoclusters emitted from the matrix to the samples in the deposition chamber.⁵⁵ The cluster yield to the number of Ar^+ ions in the beam is around 1%, for instance, ~ 28 nA of cluster beam current can be obtained by applying a $3 \mu\text{A}$ Ar^+ ion beam. An illustration of the principle of operation of the MACS process is presented in Figure 2.11.

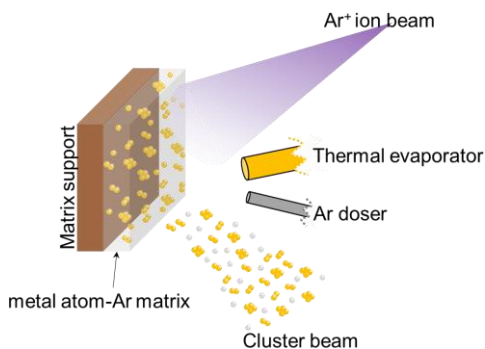


Figure 2.11 Illustration of the MACS process.

More to the point, MACS is an emerging cluster beam technology that is not only capable of massive size and composition controlled physical synthesis of catalysts, but also of achieving higher catalyst loadings in reasonable deposition time, for performing reaction studies in industrial relevant gas flow reactors. Hence, with the MACS technique, the total cluster weight is expected to reach up to μg amounts with 0.1 wt% of cluster to support ratio.⁵⁶

For this thesis a series of Au-Ag bimetallic nanoclusters are produced and deposited on glass slide supported MgO powders. $\text{Au}_{0.75}\text{Ag}_{0.25}$, $\text{Au}_{0.5}\text{Ag}_{0.5}$ and $\text{Au}_{0.25}\text{Ag}_{0.75}$ bimetallic nanoclusters are produced based by controlling the evaporation rate of the two elements from two thermal evaporators. The pressure of Ar was kept at 6×10^{-6} Torr and the metal atom-Ar matrix was condensed on the copper matrix support cooled down to 25 K. After 80 minutes of matrix formation, the matrix was subsequently sputtered with an Ar^+ beam for 5 minutes and the nanoclusters were deposited on 21 glass slides covered with MgO powder on the rotating sample carousel. STEM images of the Au-Ag nanoclusters supported on MgO powders are shown in Figure 2.12. Without mass selection, a relatively narrow size distribution is obtained and the cluster size with all the compositions is around 1.1 nm in diameter, which shows the special character of MACS.⁵⁵ A more detailed discussion of the characterization will be given in Chapter 4, which deals with the catalytic CO oxidation activity of the Au-Ag bimetallic nanoclusters on MgO produced with MACS.

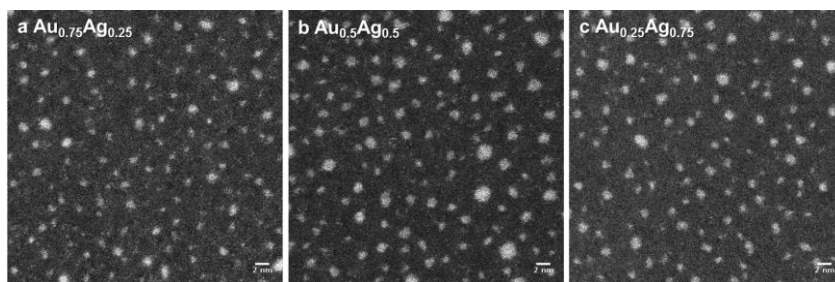


Figure 2.12 STEM images of $\text{Au}_{0.75}\text{Ag}_{0.25}$, $\text{Au}_{0.5}\text{Ag}_{0.5}$ and $\text{Au}_{0.25}\text{Ag}_{0.75}$ nanoclusters on carbon TEM grids.

2.1.4 Discussions

In the previous three sections, the three types of cluster sources that I have used during my PhD were introduced. There are advantages and limitations for all three. Considering the cluster beam flux, the matrix assembly cluster source is the most efficient one. Although MACS requires the smallest target size, however, due to the design of the evaporator, a considerable amount of the material is condensed on the wall/exit of the

evaporator. Therefore, regarding the amount of nanoclusters produced per material usage in the non-mass selected case, the laser ablation cluster source will consume the least material. The nanoclusters are mostly neutral for the laser ablation and matrix assembly cluster sources while most of the nanoclusters produced with magnetron sputtering are charged.⁶³ This high fraction of charged nanoclusters allows mass selection with a reasonably high flux. However, in order to compensate the charge of the nanoclusters produced by magnetron sputtering, the substrate must be conductive or semi-conductive. As far as the size range of the nanoclusters produced by these three cluster sources is concerned, magnetron sputtering nanoclusters have the smallest size range with the best size distribution while both laser ablation and matrix assembly cluster sources show similar performance. A comparison between the three cluster sources is given in Table 2.3.

Table 2.3 Comparison of the laser ablation, magnetron sputtering and matrix assembly cluster sources.

	Laser ablation	Magnetron sputtering	Matrix assembly	
Target dimension	7 mm / 14 mm × 24 mm × 1 mm	5 cm in diameter × 2 mm in thickness	Wires can fit in a crucible with 8 mm in diameter × 12 mm in length	
Cluster charge rate	~10 % ⁵²	> 50% ⁶³	~10% ⁵⁷	
Mass selection method	Fourfold bender	Quadrupole mass filter	N/A	
Size range	100 - ~2000 atoms	1 - 100 atoms (QMF) Up to ~500 atoms (bender only)	1 - ~2000 atoms	
Flux	w/o mass selection	5 nA	10 nA	210 nA
	w/ mass selection	50 pA	500 pA	N/A
Cluster size distribution	w/o mass selection	700 ± 150 atoms	500 ± 100 atoms	600 ± 100 atoms
	w/ mass selection	700 ± 30 atoms	50 ± 1 atoms	N/A
Substrate requirements	Vacuum compatible	Vacuum compatible Conducting or semi-conducting	Vacuum compatible	
Risk of cluster production			Cu contamination from matrix support	

2.2 Reflectron Time-of-flight mass spectrometry

The laser ablation cluster setup is equipped with an RToF mass spectrometer to analyse the mass distribution, allowing to obtain the desired cluster sizes and compositions by fine-tuning the cluster formation conditions.⁶⁵ Once the nanoclusters are formed in the cluster source chamber, they fly into the extraction chamber where the charged nanoclusters are accelerated by an electrical field originating from voltages applied on the extraction optics and reflected towards a microchannel plate (MCP) detector. Charged nanoclusters experiencing the same potential difference will receive the same kinetic energy; therefore, the velocity of nanoclusters with different masses will be different and result in different arrival times at the MCP detector. Flight time is the key parameter to determine the mass of the nanoclusters; in order to have a better mass resolution, two stage extraction and reflectron configurations are used in the laser ablation cluster setup for acquiring a better time resolution. A schematic drawing with the applied potentials on the extraction and reflectron ion optics is shown in Figure 2.13.

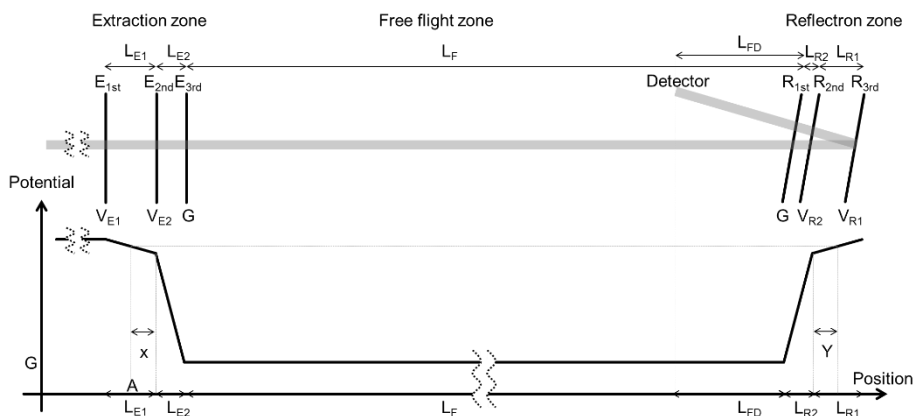


Figure 2.13 Schematic drawing of two stages reflectron time-of-flight mass spectrometer used in laser ablation cluster setup.

Due to the supersonic expansion, the nanoclusters exit the source chamber and enter the first stage of the extraction zone, in between a first and second extraction grid, with a Gaussian-like distributed initial velocity v_0 . Considering a charged cluster with mass m and a charge q at a position A a distance x from the second extraction grid, and applying pulsed voltages V_{E1} and V_{E2} on the respective first and second extraction grids, the charged cluster will experience a $x(V_{E1} - V_{E2})/L_{E1}$ potential difference and it will be accelerated to a velocity v_{E1} at the position of the second extraction grid with a traveling time t_{E1} .

$$v_{E1} = \sqrt{v_0^2 + \frac{2q}{m} \left(\frac{V_{E1} - V_{E2}}{L_{E1}} \right) x} \approx \sqrt{\frac{2q}{m} \left(\frac{V_{E1} - V_{E2}}{L_{E1}} \right) x} \quad 2.3$$

$$t_{E1} = \frac{mL_{E1}}{q(V_{E1} - V_{E2})} (v_{E1} - v_0) \approx \frac{mL_{E1}}{q(V_{E1} - V_{E2})} v_{E1}. \quad 2.4$$

In the laser ablation cluster setup, the voltages applied on the extraction grids are around 2000 V to 5000 V, and therefore the velocity v_{E1} is in the order of 10000 m/s making the initial velocity v_0 negligible. As shown in equation 2.3 and 2.4, the values of v_{E1} and t_{E1} depend on the initial cluster position with a larger x resulting in a higher velocity v_{E1} and a longer travel time t_{E1} between the first and second extraction grids. After that, the cluster is further accelerated to v_{E2} by the potential difference between the second extraction grid and the third grounded extraction grid within t_{E2} , where

$$v_{E2} = \sqrt{v_{E1}^2 + \frac{2q(V_{E2} - G)}{m}} = \sqrt{v_{E1}^2 + \frac{2qV_{E2}}{m}}, \quad G = 0 \quad 2.5$$

$$t_{E2} = \frac{mL_{E2}}{q(V_{E2} - G)} (v_{E2} - v_{E1}) = \frac{mL_{E2}}{qV_{E2}} (v_{E2} - v_{E1}), \quad G = 0. \quad 2.6$$

After the cluster leaves the extraction zone, the cluster will experience no field in the free flight zone between the grounded third extraction grid and a grounded first reflectron grid. Therefore, the velocity v_F remains v_{E2} and the traveling time is t_F ,

$$v_F = v_{E2} \quad 2.7$$

$$t_F = \frac{L_F}{v_F}. \quad 2.8$$

Static potentials V_{R2} and V_{R1} are applied on the second and third reflectron grids to decelerate the nanoclusters, to narrow the spatial/temporal distribution and to reflect the nanoclusters towards the MCP detector. When the nanoclusters fly between the first and second reflectron grids, they experience a potential difference between the grounded first reflectron grid and the second reflectron grid at potential V_{R2} . Therefore, the cluster travels with traveling time t_{R2} to reach the position of second reflectron grid with velocity v_{R2} ,

$$v_{R2} = \sqrt{v_F^2 - \frac{2q(V_{R2} - G)}{m}} = \sqrt{v_F^2 - \frac{2qV_{R2}}{m}}, \quad G = 0 \quad 2.9$$

$$t_{R2} = \frac{mL_{R2}}{q(V_{R2} - G)} (v_F - v_{R2}) = \frac{mL_{R2}}{qV_{R2}} (v_F - v_{R2}), \quad G = 0. \quad 2.10$$

Combining equations 2.3, 2.5, 2.7 and 2.9, the velocity v_{R2} and the travel time t_{R2} are dependent on the initial cluster position x . At the second stage of the reflectron, the cluster is further decelerated and comes to a standstill by a potential applied on the third reflectron grid. With a different initial position x of the acceleration in between the first and second extraction grids, the cluster reaches a different velocity resulting in a different

penetration depth y between second and third reflectron grids with different traveling time t_{R1} ,

$$v_{R1} = 0 \quad 2.11$$

$$y = \frac{mL_{R1}}{q(V_{R1}-V_{R2})} v_{R2}^2 \quad 2.12$$

$$t_{R1} = \frac{mL_{R1}}{q(V_{R1}-V_{R2})} v_{R2}. \quad 2.13$$

After that, the cluster is accelerated and gains velocity from the potentials applied on the reflectron grids and the travel time in between third to second and second to first reflectron grids will be the same as t_{R1} and t_{R2} , respectively. Again, a cluster with higher velocity will arrive at the reflectron earlier and penetrate deeper into the reflectron with longer traveling time; on the other hand, a cluster with lower velocity will arrive at the reflectron later and the time spend in the reflectron will be shorter. Therefore, the expanded spatial/temporal distribution of the nanoclusters in the free flight zone with the different velocities will be eliminated by a proper set of reflectron potentials.⁶⁶ The cluster at the grounded first reflectron grid accelerates back to the same v_F and enters the free flight zone again; finally the cluster reaches to the MCP detector with traveling time t_{FD} ,

$$t_{FD} = \frac{L_{FD}}{v_F}. \quad 2.14$$

The total cluster time of flight is t_{total} ,

$$t_{total} = t_{E1} + t_{E2} + t_F + 2 \times (t_{R2} + t_{R1}) + t_{FD}, \quad 2.15$$

and it is found that all the components in t_{total} are proportional to \sqrt{m} . That is to say, equation 2.15 can be written as

$$t_{total} = \sqrt{m} \times [C_{E1} + C_{E2} + C_F + 2 \times (C_{R2} + C_{R1}) + C_{FD}] = \sqrt{m} \times C, \quad 2.16$$

where C is a setup geometry and potential dependent constant. Due to the internal delay t_0 of the electronics used in the RTof-MS, equation 2.16 can be generalized and deduced as

$$m = a(t_{total} - t_0)^2, \quad 2.17$$

where the a is the reciprocal constant of C in equation 2.16. When the nanoclusters impact the MCP detector, the charge of the nanoclusters is amplified and the current signal is converted to a voltage signal. The voltage signal as a function of time is recorded by a digital oscilloscope. From this time information, the mass of the nanoclusters can be obtained; therefore, by analysing the mass of the nanoclusters, the size and composition of nanoclusters can be obtained. An example of a mass spectrum of Au nanoclusters as a function of time from Au₁ to Au₄₈ is shown in Figure 2.14-a; the time of flight of the Au nanoclusters with different sizes is summarized and fitted with a parabolic equation in

Figure 2.14-b. It is shown in equation 2.16 and 2.17 that the cluster time of flight is proportional to \sqrt{m} and in order to examine the time to mass relationship clearly, Figure 2.14-b is converted to Figure 2.14-c showing that the mass root indeed varies linearly with time, where the slope of the fitting line is the constant \sqrt{a} and the intercept is the internal delay t_0 . Example of the Au mass spectrum shown in Figure 2.14, the linear relationship of mass root and time can be fitted by a line with a constant $\sqrt{a} = 0.491 \text{ amu}^{1/2}/\mu\text{s}$ and a delay $t_0 = 0.881 \mu\text{s}$ and the r-square is 0.99997. A detailed application of the RToF-MS to determine the composition of Au-Ag bimetallic nanoclusters produced by various cluster formation conditions is given in section 3.2.

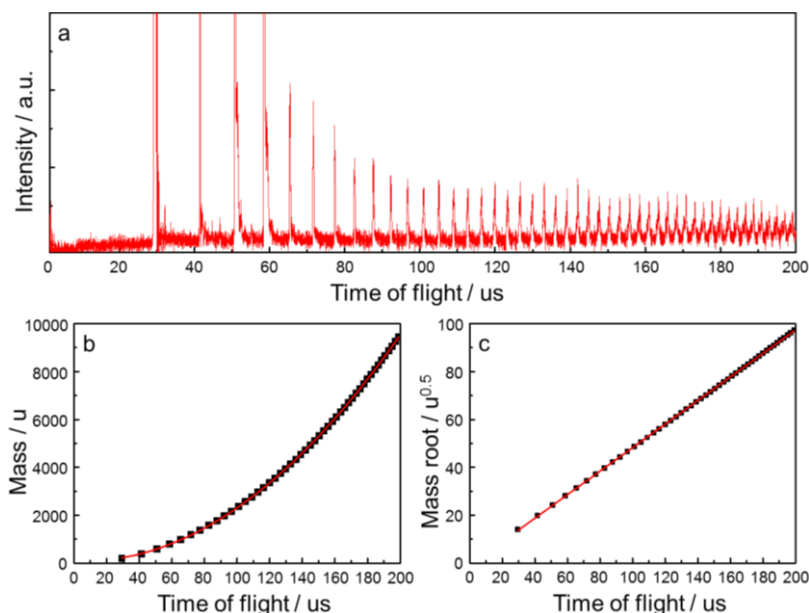


Figure 2.14 ToF spectrum of Au nanoclusters from Au₁ to Au₄₈ (a). Mass of the Au_N nanoclusters plotted as a function of time-of-flight (b) and mass root as a function of time (c).

2.3 Rutherford backscattering spectrometry

Rutherford backscattering spectrometry (RBS) is a powerful elemental analysis technique for analysing the material present on a sample surface and for providing quantitative elemental information.⁶⁷ In order to examine the average composition and the coverage of the nanoclusters deposited on substrates, RBS is applied in the Ion and Molecular Beam Laboratory (IMBL) of Institute for Nuclear and Radiation Physics (IKS) KU Leuven. RBS is a high energy ion scattering technique. A mono-energetic α particle (He^+) beam with an energy of a few MeV is collimated and directed onto the sample surface to collide with the atoms of the sample surface with a probe size around 1 - 2 mm.

The α particles backscattered by the nuclei by Coulomb repulsion are collected with a fixed angle detector; the amount of material and the elemental information can be extracted by analysing the number and energy of backscattered α particles. An illustration of the RBS setup is shown in Figure 2.15-a. RBS analysis can provide high accuracy evaluations of the atomic content of heavy atoms, such as Ni, Ag, Pt and Au studied in this thesis. Classical Coulomb repulsion elastic scattering is the basic principle of RBS. Based on the interaction between the α particles and the nuclei of target atoms in sub-monolayer cases, the kinematic factor and scattering cross section can be used to determine the atomic mass and amount of the target nuclei by the energy and the intensity of a backscattering peak. In general, the higher the atomic mass of the target nuclei, the higher the energy of the peaks present in a spectrum; the higher the amount of the target nuclei, the more intense the peak will be; with the same amount of nuclei of two elements, the element with higher atomic mass will result in a more intense RBS peak. The RBS mechanism is shown in Figure 2.15-b.

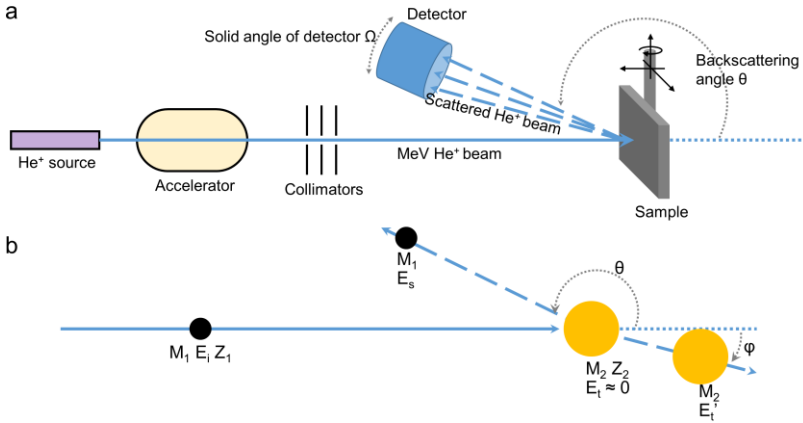


Figure 2.15 Illustrations of a general RBS allocation (a) and mechanism of RBS on an elastic collision between a projectile ion and a target atom.

The incident projectile particle with mass m_1 is accelerated to E_i to collide on a target particle m_2 with kinetic energy E_t ; after collision, the projectile particle lost energy E_t' and the energy is transferred to the target particle m_2 . The projectile particle is backscattered with energy E_s and an angle θ . Since the energy range of the accelerated particle m_1 is in a MeV range, the initial kinetic energy E_t of target particle m_2 is negligible. Based on the conservation of momentum and kinetic energy, the process can be described as,

$$E_i = E_s + E_t' \quad 2.18$$

$$\sqrt{2M_1 E_i} = \sqrt{2M_1 E_s} \cos \theta + \sqrt{2M_2 E_t'} \cos \phi \quad 2.19$$

$$0 = \sqrt{2M_1E_s} \sin \theta + \sqrt{2M_2E_t'} \sin \varphi. \quad 2.20$$

The energy of backscattered projectile particle E_s can be described by solving the equations 2.18, 2.19 and 2.20, and the ratio of E_s to E_i , the kinematic factor K , also can be obtained,

$$K = \frac{E_s}{E_i} = \left[\frac{\sqrt{M_2^2 - M_1^2 \sin^2 \theta} + M_1 \cos \theta}{M_1 + M_2} \right]^2. \quad 2.21$$

With a fixed detector position, the scatter angle θ becomes a fixed value and makes that the kinematic factor only depends on the mass of the target atom. Hence, this mass can be derived from a measurement of the backscattering energy of the projectile particles, and a higher E_s obtained in a spectrum means the mass of the target atom is higher. RBS spectra of trimetallic CuAgAu nanoclusters supported on SiO₂ wafers are shown in Figure 2.16 and it shows the RBS is capable of resolving the chemical information of the sample with different scattering energy and showing three individual peaks of Cu, Ag and Au.

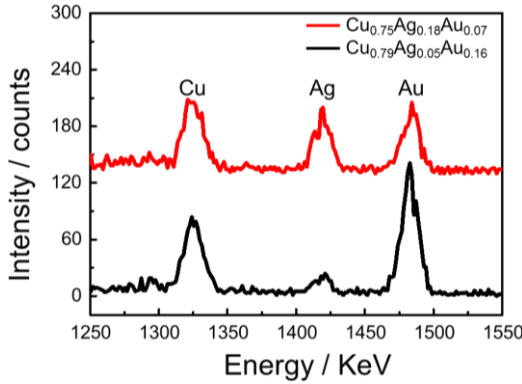


Figure 2.16 RBS spectra of trimetallic CuAgAu nanoclusters produced from MACS with different compositions.

The chemical information and the amount of different types of atoms also can be revealed from the RBS spectrum by the peak intensity, which is determined by the scattering cross section of elements $\sigma(\theta)$, which is the probability of a projectile particle with atomic number Z_1 scattered by the target atom with atomic number Z_2 into a solid angle Ω of the detector placed at the angle θ and it is deduced from the elastic close-impact scattering collisions with Coulomb repulsion as the central force, first derived by Ernest Rutherford in a gold foil scattering experiment,

$$\sigma(\theta) = \left(\frac{Z_1 Z_2 e^2}{4E_i} \right)^2 \frac{d\Omega}{\sin^4\left(\frac{\theta}{2}\right)}. \quad 2.22$$

Based on equation 2.22, with a number of projectile particles N_i scattered by a number of target particles N_t into the detector with a solid angle Ω , the total count of the scattered particles that will reach the detector is,

$$I(\theta, \Omega) = \sigma(\theta)\Omega N_i N_t. \quad 2.23$$

Considering a fixed detector position and constant number of projectile particles, the peak intensity is proportional to $Z_2^2 N_t$ and it explains why RBS is more sensitive to heavy elements. Although the amount of the Ag atoms is around 2.5 times that of Au atoms in the sample of $\text{Cu}_{0.75}\text{Ag}_{0.18}\text{Au}_{0.07}/\text{SiO}_2$, in Figure 2.16, the RBS intensity of the Au peak is still slightly higher than the peak of Ag. The squared ratio of the atomic number is $(Z_{\text{Au}}/Z_{\text{Ag}})^2 \approx 2.8$. In the case of $\text{Cu}_{0.79}\text{Ag}_{0.09}\text{Au}_{0.16}$ nanoclusters, with a reduced Ag amount, the RBS intensity of the Ag peak is dramatically decreased. In both cases, Cu is the most abundant element, however the atomic number of Cu is the lowest ($Z_{\text{Cu}} = 29$) and therefore it appears with lower intensity; in the case of $\text{Cu}_{0.75}\text{Ag}_{0.18}\text{Au}_{0.07}$, the atom number ratio $N_{\text{Cu}}/N_{\text{Au}} \approx 10.7$ with squared ratio of the atomic number $(Z_{\text{Au}}/Z_{\text{Cu}})^2 \approx 7.4$ and results the Cu peak intensity with a 1.4 times higher than Au peak intensity.

2.4 Scanning transmission electron microscopy

High-angle annular dark field scanning transmission electron microscopy (HAADF-STEM) is an advanced technique to image nanostructures with sub-Ångstrom resolution.⁶⁸ The basic principle of STEM is converting a high energy electron (200 KeV) beam into an aberration-corrected electron probe to interact with the nanostructures, such as nanoclusters. The electrons can interact with the atoms in the sample via various interactions. As the electrons are scattered by the atoms to a high angle ($> 3^\circ$ or 50 mrad, $1 \text{ mrad} = 0.0573^\circ$) and collected by a HAADF detector, an atomic number (Z) contrast HAADF-STEM image is recorded. The HAADF-STEM used in this thesis was a JEOL-2100F in NPRL, University of Birmingham. A schematic drawing and the mechanism of HAADF-STEM is shown in Figure 2.17.

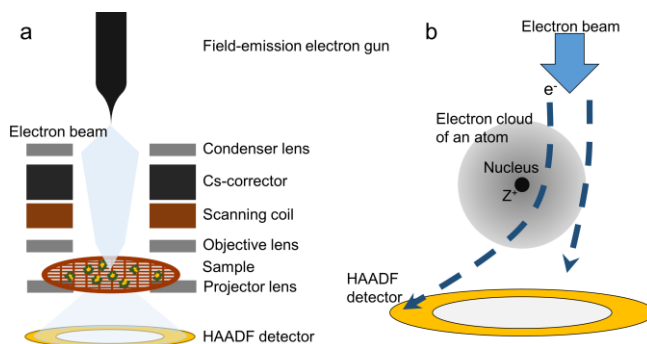


Figure 2.17 Schematic drawing (a) and the mechanism of HAADF-STEM (b).

The electrons are generated and emitted from an electric field E applied on the tip of a field-emission electron gun with narrow energy spread (0.3 eV at 100 kV); the electron beam is accelerated to high voltage (50–400kV) and focused and aberration-corrected by a set of electromagnetic condenser lenses and Cs-correctors, respectively. The direction of the electron beam is controlled by the scanning coil and introduced to the sample. The electrons can interact with the atoms of the sample with various possibilities, such as electrons scattered by the atomic nuclei and deflected to high angle to form dark-field images, electrons scattered by the electron cloud of atoms and deflected to low angle to form diffraction patterns and the unscattered electrons form the direct beam passing through the sample and contribute to bright-field images. In the ideal case, the mechanism of forming dark-field images can be explained by the Rutherford scattering discussed in section 2.3 and the intensity of the signal can be described by equation 2.23 with some modification,

$$I(\theta, \Omega) = \left(\frac{Ze^2}{4Ei}\right)^2 \frac{\Omega N_i N_t}{\sin^4\left(\frac{\theta}{2}\right)}. \quad 2.24$$

As a result, the HAADF-intensity is containing the information of the atomic number (Z) of the atoms and also the number of atoms in an atomic column; therefore, HAADF imaging is also called Z -contrast imaging. However, due to the incoherent nature of the high-angle signal, HAADF-STEM images carry little information about the crystallite orientation of the sample. Therefore, in reality, the HAADF-intensity is not proportional to Z^2 , but it will be proportional to Z^n where n is an instrument specific parameter in the range 1.4 - 1.9 for most cases.⁶⁹ The instrument specific parameter n can be determined by co-depositing two kinds of mass selected nanoclusters A_{N_A} , and B_{N_B} , with different elements A and B onto the same TEM grid and imaging these nanoclusters into the same image frames; therefore, if all the image settings are the same, the intensity ratio of the two cluster types will be,

$$\frac{I_A}{I_B} = \frac{N_A}{N_B} \left(\frac{Z_A}{Z_B}\right)^n. \quad 2.25$$

I_A and I_B can be obtained by integrating the HAADF intensities of the these two kinds of nanoclusters and with the known parameters of N_A , N_B , Z_A and Z_B , the instrument specific parameter n can be determined. For the STEM at the University of Birmingham, n was determined by examining Au_{923} and Pd_{923} nanoclusters and n is 1.46 ± 0.18 .⁷⁰ With this information, equation 2.25 can be generalized and can be used for cluster weighing by measuring the intensity ratio of nanoclusters to single atoms⁷¹ or for revealing the chemical composition and arrangement within nanoclusters.²² A detailed study of composition-dependent spatial atomic arrangement in Au_xAg_{1-x} bimetallic nanoclusters will be discussed in Chapter 3.

2.5 X-ray photoelectron spectroscopy

The catalytic properties of nanoclusters are strongly correlated with their electronic structure. Therefore, in order to reveal the detailed electronic structure of supported nanoclusters, the photo-electron spectroscopy (PES) technique is utilized to provide information of filled core states and filled valence states, using X-ray photo-electron spectroscopy (XPS, 10 – 1000 eV) and ultra-violet photo-electron spectroscopy (UPS, 5 – 20 eV), respectively.⁷² The photo-electrons ejected from the core levels carry valuable fingerprint information about the investigated samples. Especially, XPS is an ideal technique to obtain the information of binding energy and its variation as a function of the chemical environment of the element of interest. This binding energy variation is known as chemical shift.

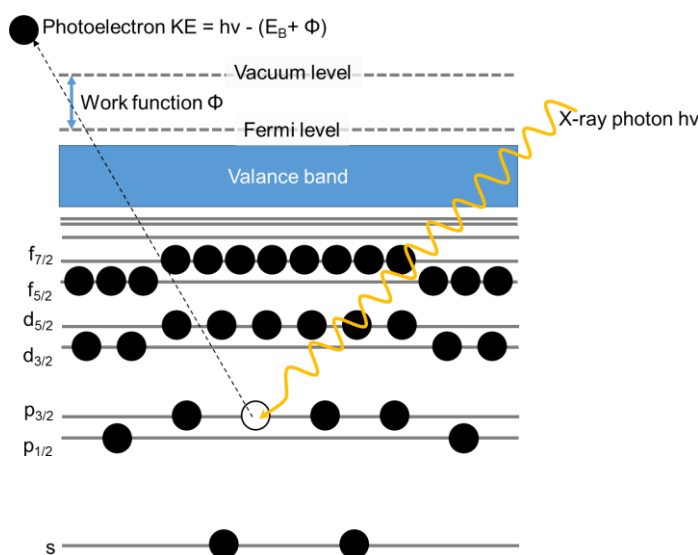


Figure 2.18 Illustration of X-ray photoelectric effect, the principle of X-ray photoelectron spectroscopy

As a photon impacts on an atom, the photon can be scattered by the orbiting electrons of the atom with partial energy transfer. It is also possible that the photon energy, which is higher than the binding energy of the electron, is totally transferred to the electron and results in the electron emitted from the atom to the vacuum state with kinetic energy. This is called the photoelectric effect and is the origin of the XPS process.⁷² The principle of the XPS process is illustrated in Figure 2.18 and it can be described by Einstein's photoelectron equation:

$$E_{kinetic} = h\nu - E_{binding\ energy} - \phi \quad 2.26$$

where $E_{kinetic}$ is the kinetic energy of the electron as measured by the instrument, $h\nu$ is the energy of the X-ray photons used, $E_{binding}$ is the binding energy of the emitted photoelectron and ϕ is the work function dependent on the material of the spectrometer. In practice, during the experiments, the sample and the spectrometer are grounded together and it shifts the Fermi level of both the sample and the spectrometer at the same level. As the $h\nu$ and the ϕ are known, the $E_{binding}$ can be obtained by measuring the $E_{kinetic}$:

$$E_{binding} = h\nu - E_{kinetic} - \phi. \quad 2.27$$

The variation of the binding energy is caused by the change of the charge state. In general, if the atoms are oxidized, the coulombic interaction between the photo-emitted core electron and the ion core will become stronger and results in a higher binding energy; on the other hand, as the atoms are reduced, the binding energy will become lower.

Due to the electron-matter interactions, the photoelectron escape depth (inelastic mean free path) is limited, and makes XPS a surface-sensitive analysis method. The intensity of the emitted electrons (I_d) is damped as a function of the distance (d) from its origin in a direction normal to the surface, given by the Beer-Lambert relationship:

$$I_d = I_0 e^{(-d/\lambda_E)}, \quad 2.28$$

where the I_0 is the electron intensity from the origin and the λ_E is the inelastic mean free path as a function of electron kinetic energy and it is described as the average distance travelled by an electron through a solid without losing energy.

To perform XPS experiments, a typical apparatus is composed of photon sources, an electron energy analyser and an electron detector. A schematic drawing of an XPS apparatus is shown in Figure 2.19. Since the photon energy range is within the soft X-ray range and the travel distance of the electron is around 1 meter, XPS measurements should be carried out in UHV to reduce X-ray absorption and photo-electron scattering. The photon source can be a He UV lamp for conducting UPS or, to generate X-ray fluorescence for XPS measurements, can be obtained by electron bombarding a metal target, Al target for example. Synchrotron radiation facilities can provide an ultra-high flux photon source for conducting XPS measurements. The electrons emitted from the sample surface then pass into an energy analyser. There are four types of electron energy analysers based on magnetic and electrostatic fields, which are magnetic double focusing spectrometer, the electrostatic retarding potential spectrometer, electrostatic cylindrical mirror analyser and electrostatic concentric hemispherical analyser. Behind the energy analyser, electrons are counted by an electron multiplier or a channel plate detector.

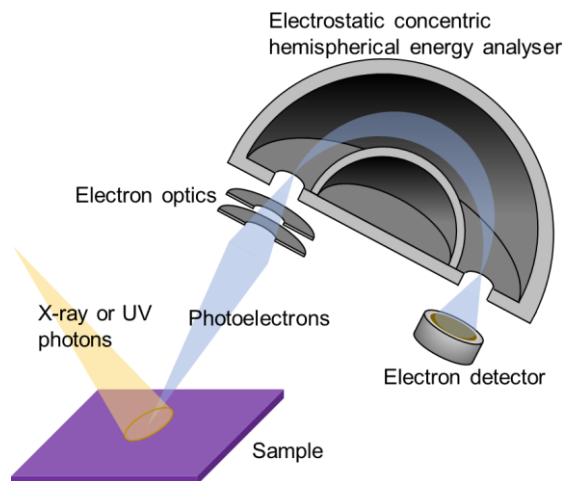


Figure 2.19 Schematic drawing of a typical experimental arrangement of XPS.

2.6 X-ray absorption fine structure spectroscopy

The electronic properties, oxidation states and local atomic structural information can be revealed by X-ray absorption fine structure spectroscopy (XAFS) measured at synchrotron X-ray sources. X-rays are absorbed by an atom at energies near and above a specific absorption edge.⁷³⁻⁷⁵ The X-ray absorption spectrum can be collected either in transmission mode by measuring the sample X-ray absorbance or in fluorescence mode by collecting the X-ray fluorescent photons. An X-ray absorption spectrum can be divided into two energy regions: the X-ray absorption near edge structure (XANES) which includes transitions from core electronic states of the atom to the empty electronic states and the extended X-ray absorption fine structure (EXAFS) measuring the atom core to continuum states transitions. These two regimes provide complementary information: the electronic and oxidation states can be obtained from XANES, while the local atomic structure of the element of interest, such as the type, coordination number and distance to neighbouring atoms, is revealed by EXAFS. Conventional transmission XAFS measurements for concentrated samples are carried out by placing the sample perpendicular to the X-ray beam direction. However, in order to study the structure of deposited nanoclusters without aggregation, the density of the nanoclusters present on a sample surface must be extremely diluted and the cluster coverage should be kept below 1 atomic ML. Therefore, the XAFS measurements carried out in this thesis were performed in fluorescent reflection mode XAFS (Refl-XAFS) at the BM08 LISA beamline at The European Synchrotron (ESRF). A schematic drawing of a typical experimental arrangement of Refl-XAFS is shown in Figure 2.20.

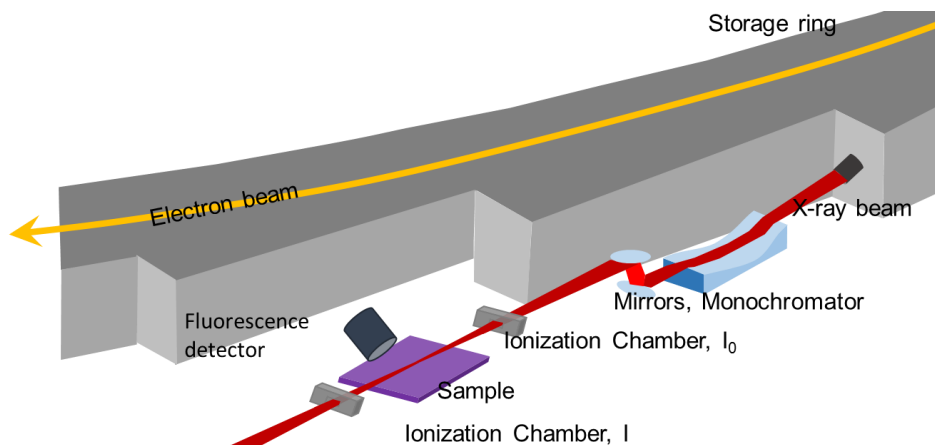


Figure 2.20 Schematic drawing of a typical experimental arrangement of Refl-XAFS.

X-rays are generated upon changing the direction of a high energy electron beam circulating in a storage ring of a synchrotron. Therefore, the light emission from the energetic electron beam perturbed by the magnetic field is called synchrotron radiation. The electrons are generated and accelerated to few GeV, for instance 6 GeV at ESRF, by the linear accelerator and the booster ring and the accelerated electron beam is transferred to the storage ring, which is utilized to maintain the energy of the electron beam and provide synchrotron radiation to the beamlines.⁷⁶ The direction of the electron beam in the storage ring is changed to emit synchrotron radiation, using bending magnets, undulators and/or wigglers. Undulators are located in straight sections of the storage ring, whereas bending magnets are used to direct the electron beam from one straight section to another. Once the synchrotron radiation is generated, it is guided into a beamline and then monochromatized and focused into a narrow distributed radiation beam by a series of optical elements. In XAFS measurements, the intensity I_0 of the incident X-ray is measured by an ion chamber which is filled with N_2 , Ar or Kr gas to absorb about 10% of the incident X-ray photons and convert it to current signal. Depending on the nature of the samples a number of different detectors are available to measure the intensity I of the X-ray interacting with the sample. In transmission mode, another ion chamber is used to measure the X-ray intensity directly. In fluorescence mode, a high purity Ge multi-detector array collects the fluorescence radiation peaks generated by the atom of interest in the sample. The fluorescence spectra can be converted to the X-ray absorption signal. With a fixed incident X-ray intensity I_0 , stronger X-ray absorption of the sample results in a stronger X-ray fluorescence signal. It can also be obtained by collecting the photoelectrons generated from the sample by electron detector in total-electron-yield (TEY) mode. The fluorescence and electron-yield signals are correlated to the X-ray

absorption and therefore can be converted to absorption signal. The mechanism of XAFS measurements is described below.

In transmission mode the intensity of the X-ray I after passing through a sample with thickness d can be described by the Beer-Lambert law first introduced in 2.39 and it can be rewritten as,

$$I = I_0 e^{(-\mu(E)d)}, \quad 2.29$$

where $\mu(E)$, the absorption coefficient of the sample material, is a function of incident X-ray photon energy E with wavelength λ , the sample density ρ , the atomic number Z and atomic mass A of the material,

$$\mu(E) \approx \frac{\rho Z^4}{AE^3} = \frac{\rho Z^4 \lambda^3}{A(hc)^3}. \quad 2.30$$

As the energy of the incident X-ray equals the binding energy of a core-level electron, a sharp rise of the X-ray absorption will occur which is called an absorption edge, and corresponds to an excitation of the core level electrons to the continuum. The kinetic energy of that excited electron is following Einstein's photoelectron equation described in 2.26. The decay of the excited atomic state follows two mechanisms: X-ray fluorescence and Auger electron emission, which are shown in Figure 2.21. It can be easily understood that once the absorption event occurs, the excited atom must decay to lower energy via these two mechanisms. Therefore, in both cases, the probability of X-ray fluorescence or Auger electron emission is directly proportional to the absorption probability.

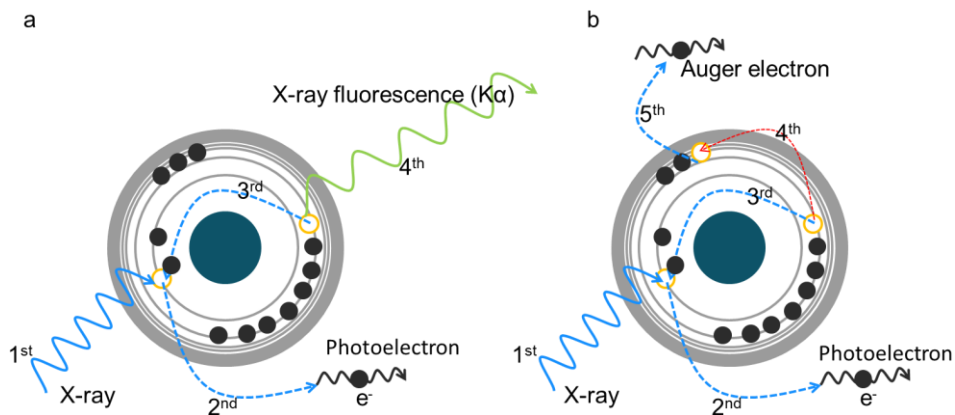


Figure 2.21 Schematic drawing of decay mechanisms of the excited atomic state: X-ray fluorescence (a) and the Auger effect (b).

The binding energy of an electron is determined by the combined effects of the attraction from the positive nucleus and the repulsion from the negatively charged electrons. Therefore, in general, with a higher oxidation state of the metal, the excitation energy required is higher which will result in a blue shift of the absorption edge in the XANES spectrum.

The excited photoelectron will propagate away from the absorbing atom with a wave number of

$$k = \sqrt{\frac{2m(E - E_{binding\ energy})}{\hbar^2}} = 0.512(E - E_{binding\ energy})^{1/2}, \quad 2.31$$

where m is the mass of an electron and E is the photon energy of the incident X-ray photon; therefore the wave number, wavelength, of the excited photoelectron is tuned by the photon energy of the incident X-ray photon. The outgoing photoelectron wave can be scattered by the neighbouring scattering atoms; the outgoing photoelectron wave interacts with the backscattered photoelectron wave and results in constructive or destructive interference, depending on the type, the number and the distance of the scattering atoms.

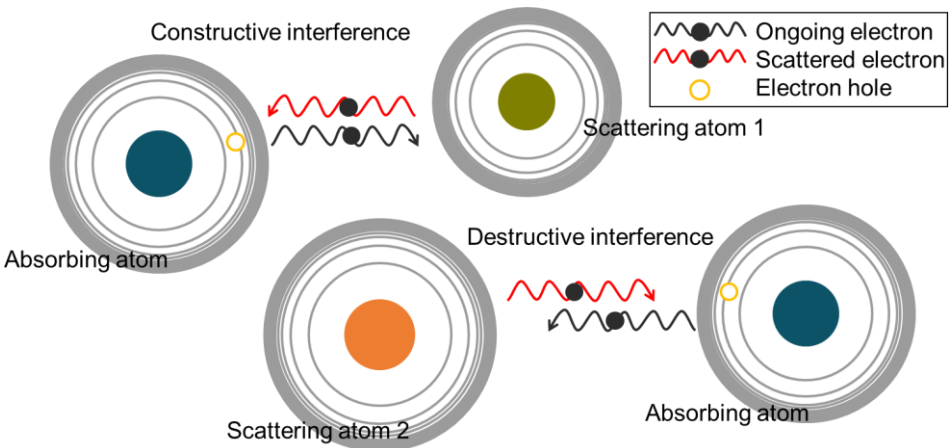


Figure 2.22 Schematic drawing of the constructive (top row) and destructive (bottom row) interferences of outgoing photoelectron wave and the backscattered electron wave.

A schematic drawing of this process is shown in Figure 2.22. The interference between the waves of outgoing and backscattered photoelectron modulates the EXAFS photoexcitation cross-section. If the outgoing and the backscattered photoelectron are in phase, it results in a constructive interference and a local maximum in the X-ray photon absorption cross-section is obtained (top row of Figure 2.22). However, a destructive interference between outgoing and backscattered photoelectron results in a local minimum in photon absorption cross-section (bottom row of Figure 2.22). This is the

origin of the oscillating portion of the absorption coefficient $\mu(E)$ and it is the main consideration of the EXAFS technique. Therefore, the XAFS signal can be described by a combination of the isolated-atom absorption $\mu_0(E)$ and the modulated absorption, EXAFS signal, $\chi(E)$ with the scattering contributions from the neighbouring atoms. The absorption coefficient $\mu(E)$ can be written as

$$\mu(E) = \mu_0(E)(1 + \chi(E)), \quad 2.32$$

and the fractional modulation of the XAFS signal, $\chi(E)$, can be defined as:

$$\chi(E) = \frac{\mu(E) - \mu_0(E)}{\mu_0(E)} \approx \frac{\mu_{exp} - \mu_{bg}}{\Delta\mu_{exp}}. \quad 2.33$$

These components of the XAFS signal introduced in equation 2.33 are illustrated in Figure 2.23. Due to the fact that the absorbing atoms always have neighbouring atoms in XAFS experiments, $\mu_0(E)$ is not experimentally accessible. Therefore, it can be approximated as in equation 2.33, where μ_{exp} is the measured absorption signal, $\Delta\mu_{exp}$ is the edge jump obtained through extrapolation of the pre-edge (green dashed line) and post-edge lines (blue dashed line) and μ_{bg} is a smooth background spline function fitted through the data.

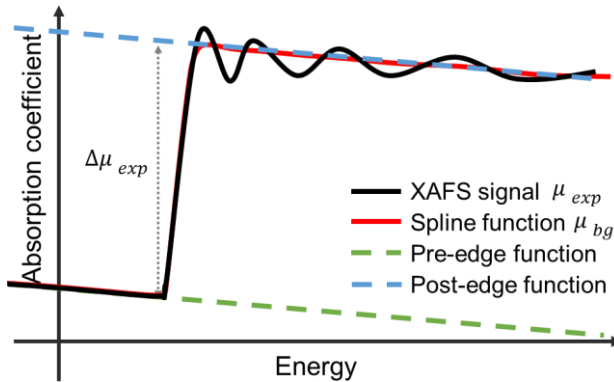


Figure 2.23 Illustration of the absorption signal, edge jump extrapolated from the pre- and post-edge lines and the spline function of the absorption background.

The EXAFS signal $\chi(E)$ is normally expressed as a function of wave number k and the $\chi(k)$ can be obtained from equation 2.31. Qualitatively speaking, the EXAFS oscillation amplitude is proportional to the number of neighbouring/scattering atoms, the frequency of the EXAFS oscillation is inversely proportional to the distance between absorbing atom to the scattering atom, and type of the scattering atom is revealed by the shape of the EXAFS oscillation.

For quantitative analyses, the EXAFS signal $\chi(k)$ contains all the contributions from all the N_j scattering atoms around the absorbing atom $\chi_j(k)$ at the j -shell on a distance R_j , and due to the wave property of the electrons, the EXAFS signal $\chi(k)$ from scattering atoms can be expressed as:

$$\chi(E) = \sum \chi_j(E) = \sum A_j(k) \sin[\Phi_j(k)], \quad 2.34$$

where $A_j(k)$ and $\sin[\Phi_j(k)]$ are the amplitude function and the oscillation function of EXAFS, respectively. They are expressed as:

$$A_j(k) = \frac{N_j}{kR_j^2} S_0^2 F_j(k) e^{-2k^2\sigma_j^2} e^{\frac{-2R_j^2}{k\lambda(k)}}, \quad 2.35$$

$$\Phi_i(k) = 2kR_i - \phi_i(k), \quad 2.36$$

where the S_0^2 is an amplitude reduction factor that considers many-body effects such as central atom shake-up and shake-off due to relaxation processes after the excitation event. $F_j(k)$ is the theoretical backscattering amplitude function, which is a function of the atomic number of the backscattering element j , $e^{-2k^2\sigma_j^2}$ is the Debye–Waller factor that considers the damping effects due to thermal motion and static disorder of the scattering atoms and $e^{\frac{-2R_j^2}{k\lambda(k)}}$ considers the amplitude loss resulting from photoelectron loss through inelastic scattering with the electron mean free path length $\lambda_j(k)$. $\phi_j(k)$ represents the phase shift function of the j th shell including the phase shift between the absorber and the backscattering atom j which occurs during the scattering process and in leaving and entering the absorber atom. $\phi_j(k)$ can be obtained from crystallography experiments of crystals with well-known structures or ab initio theoretical calculations.

It is useful to examine the EXAFS data in R-space by Fourier transforming the k-space data with a k^n weighting factor ($n = 1, 2, 3$) within a reliable k window of the EXAFS data and therefore,

$$\chi(R) = FT[\chi(k)] = \frac{1}{\sqrt{2\pi}} \int_{k_{min}}^{k_{max}} k^n \chi(k) e^{2ikR} dk \quad 2.37$$

The information of the scattering element, numbers of scattering atoms for each type of elements, distance between the absorbing atoms to the scattering atoms and the Debye–Waller factors of each shell can be extracted by least square EXAFS data refinement to find the best fits of the experimental spectra and to provide scientifically reasonable models. During the data analysis the parameters used to fit the EXAFS data should not exceed the number of independent parameters N_{ip}

$$N_{ip} \approx \frac{2\Delta k \Delta R}{\pi}. \quad 2.38$$

The EXAFS data analysis can be done with EXAFS program packages to obtain the structural parameters and in this PhD thesis the EXCURVE⁷⁷ software was utilized.

2.7 Gas flow reactor

In order to examine the catalytic activity of the designed and synthesized mono/bimetallic nanoclusters, the gas flow reactor in the Centre for Surface Chemistry and Catalysis (COK), KU Leuven was used. Continuous gas flow packed bed reactors allow good control over reaction conditions including temperature, temperature ramping rate, gas mixture and gas flow. The position of the catalyst is fixed inside the chemically inert quartz tube reactor. Due to the way the catalyst is installed inside the reactor, the gases have a higher chance to reach the catalyst surface resulting in a higher conversion per weight of catalyst than other catalytic reactors. The quartz tube reactor is installed inside a furnace and the temperature of the reactor is controlled by the furnace from room temperature to 300 °C with a desired ramping rate; the composition fine-tuned reactant gases are delivered by a series of gas flow controllers to the quartz tube reactor. The products of the reactions formed inside the quartz tube reactor are delivered to a mass spectrometer. A schematic drawing of the gas flow reactor is shown in Figure 2.24.

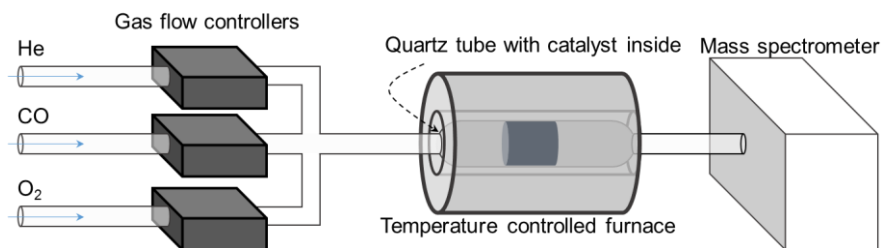


Figure 2.24 Schematic drawing of the gas flow reactor.

2.8 Temperature-Programmed Desorption

Temperature-programmed desorption (TPD), also called thermal desorption spectroscopy (TDS), is a straightforward technique to obtain information on the physisorption, chemisorption and chemical reactions occurring on surfaces by measuring the desorbed molecules from a sample surface as the surface temperature is increasing.⁷⁸ TPD experiments are usually conducted in an UHV environment to increase the sensitivity of molecule detection, using a mass spectrometer, gas dozer and temperature controller. First, the sample, kept at a certain temperature, is exposed to a gas, where the exposure in Langmuir units is controlled through a leak valve. Then the sample is heated linearly to drive the adsorbed molecules to desorb. Simultaneously the desorbing species are recorded as a function of the sample temperature by a quadrupole mass spectrometer (QMS). Measurement of desorption temperature and the quantification of specific species

enables the derivation of the desorption energy. A typical experimental arrangement of a TPD setup is shown in Figure 2.25 and a detailed description of a homebuilt TPD setup designed during my PhD is discussed in section 2.8.1.

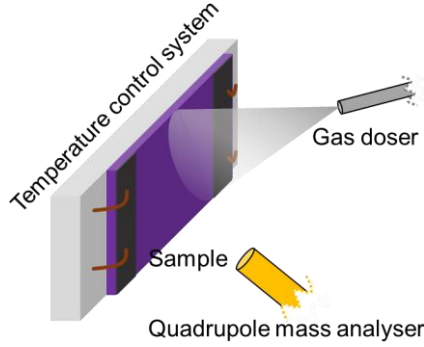


Figure 2.25 Schematic drawing of the temperature programmed desorption.

The general TPD process is described by the desorption rate, $r_d(\theta)$, which is the number of desorbing molecules per unit time and per unit area. It can be described by the Arrhenius equation:

$$r_d(\theta)A = -An_a \frac{d\theta}{dt} = -An_a \nu(\theta) \theta^m e^{-\frac{E_d(\theta)}{kT}}, \quad 2.39$$

where, A is the total area of the sample surface, n_a the number of adsorption sites per area, θ the molecule coverage, $\nu(\theta)$ the pre-exponential factor, m the order of desorption, $E_d(\theta)$ the activation energy for desorption given by $E_d = -\Delta H_{adsorption} = \Delta H_{desorption}$, K the ideal gas constant and T the temperature. In practice, experiments are conducted with the temperature increasing linearly as a function of time. Therefore the temperature T can be described as

$$T = T_0 + \beta t \quad 2.40$$

where T_0 is the initial temperature, β is the heating rate and t the time. The linear heating rate is related to the rate of desorption and $r_d(\theta)$ can be written as

$$r_d(\theta) = -n_a \frac{d\theta}{dT} \frac{dT}{dt} = -n_a \nu(\theta) \theta^m e^{-\frac{E_d(\theta)}{kT}} \quad 2.41$$

and the term of $\frac{d\theta}{dT}$ can be derived as

$$\frac{d\theta}{dT} = -\frac{dt}{dT} \nu(\theta) \theta^m e^{-\frac{E_d(\theta)}{kT}} = -\frac{\nu(\theta)}{\beta} \theta^m e^{-\frac{E_d(\theta)}{kT}} \quad 2.42$$

the maximum rate of desorption can be found at the temperature T_{max} at which $\frac{d^2\theta}{dT^2}$ is zero:

$$\frac{d^2\theta}{dT^2} = -\frac{d}{dT} \left(\frac{v(\theta)}{\beta} \theta^m e^{-\frac{E_d(\theta)}{KT}} \right) = 0 \quad 2.43$$

$$m\theta^{m-1} \frac{d\theta}{dT} = -\frac{\theta^m E_d(\theta)}{KT_{max}^2}. \quad 2.44$$

Substitution of the $\frac{d\theta}{dT}$ from equation 2.42 into equation 2.44 results in

$$m\theta^{m-1} \frac{dt}{dT} v(\theta) e^{-\frac{E_d(\theta)}{KT_{max}}} = \frac{E_d(\theta)}{KT_{max}^2}. \quad 2.45$$

The characteristics of molecular desorption from the sample surface can be described by equation 2.45. In general, the T_{max} decreases as the order of reaction m increases.

The behaviour of molecules desorbing from the surface determines the order of desorption. In the following, the zeroth order, first order and second order of desorption will be discussed. If the adsorbed molecules can rapidly diffuse on the sample surface and exchange the position of the other adsorbed molecules on the molecule island, which means the supply of desorption molecule isn't limited until the island disappeared at the sample surface. This type of desorption behaviour is the zeroth order desorption and is illustrated in Figure 2.26-a. The desorption curve in TPD is a convolution of the molecule coverage and the desorption rate. Therefore, the desorption rate goes up with temperature exponentially as $r_d(\theta) = -\frac{v(\theta)}{\beta} e^{-\frac{E_d(\theta)}{KT}}$ and the desorption rate is independent from the molecule coverage. Therefore, the raising edge of different coverages behaves the same. (Figure 2.26-b) The desorption rate will reach a maximum value when the molecules present on the surface are all consumed. Hence the temperature of the desorption peak, T_{max} , increases with the coverage θ . Beyond the desorption peak the falling edge drops quickly.

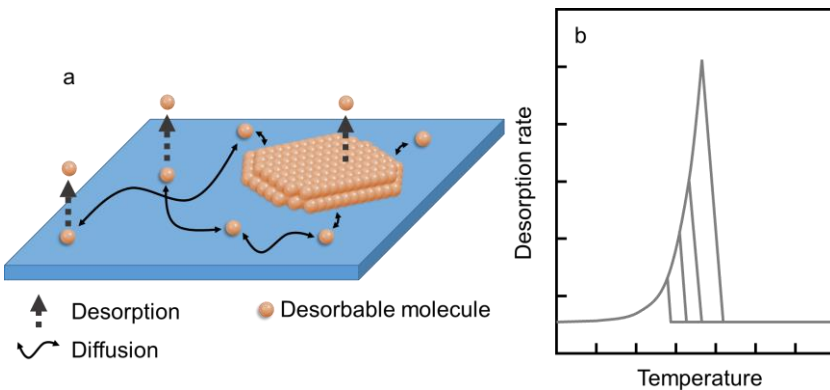


Figure 2.26 Illustration of zero order desorption mechanism (a) and desorption curves of zero order desorption with different coverages.

When a layer of molecules is present on the sample surface and all the molecule can desorb from any position of the single layer of molecule island without dissociating, illustrated in Figure 2.27-a, it is a first order desorption behaviour and $m = 1$. Therefore, the equation 2.45 can be rewritten as:

$$\frac{dt}{dT} v(\theta) e^{\frac{-E_d(\theta)}{KT_{max}}} = \frac{E_d(\theta)}{KT_{max}^2}, \quad 2.46$$

which means T_{max} is independent of the initial coverage. The expected desorption curves with different coverages are illustrated in Figure 2.27-b. The main features of the first order desorption character are: 1) same position of desorption peak with different coverages, 2) asymmetric peak shape with steady slope up to the peak and falling away rapidly at temperatures above the peak and 3) the shape of the desorption curves with different coverages is similar to each other.

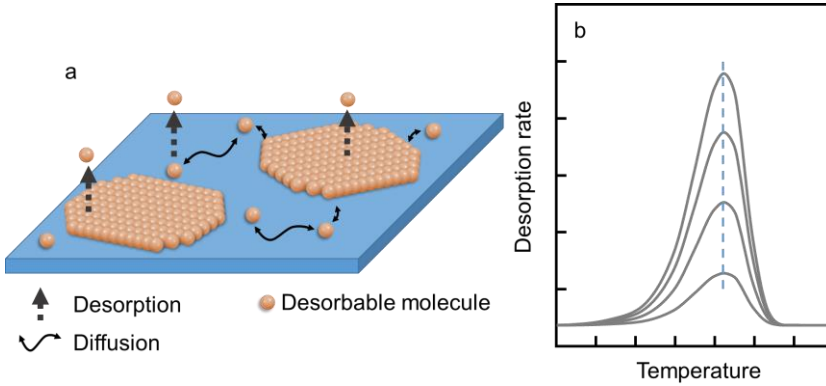


Figure 2.27 Illustration of first order desorption mechanism (a) and desorption curves of first order desorption with different coverages.

The second order desorption describes the associative desorption when A and B molecules are present at the sample surface. At least one of both species must be mobile on the surface; the desorption of molecules occurs when A and B combine into a single molecule AB. The process is illustrated in the Figure 2.28-a. The desorption rate is proportional to θ^2 and the desorption order corresponds to $m = 2$. Therefore, equation 2.45 can be rewritten as:

$$2\theta \frac{dt}{dT} v(\theta) e^{\frac{-E_d(\theta)}{KT_{max}}} = \frac{E_d(\theta)}{KT_{max}^2}, \quad 2.47$$

which shows the correlation between the temperature of maximum desorption T_{max} and the coverage θ . T_{max} decreases as θ increases and with different coverages the curves of desorption are symmetrical with shared trailing edges at the end of the desorption curve.

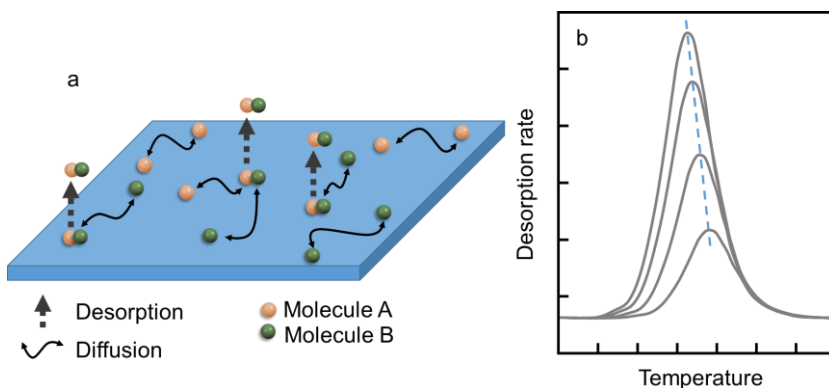


Figure 2.28 Illustration of second order desorption mechanism (a) and desorption curves of second order desorption with different coverages.

2.8.1 General description of the homebuilt TPD setup

In order to perform in situ TPD experiments with the nanoclusters deposited in Leuven, a new TPD setup was designed and constructed. The setup consists of two main parts, the TPD chamber and the sample transfer system compatible with the vacuum suitcase which allows to study in situ catalytic activity of nanoclusters produced from the different cluster sources and transferred in vacuum to limit the cluster oxidation and other effects from contaminations. A top and a side view of the TPD setup are shown in Figure 2.29. A sample can be loaded into the main TPD chamber via the load lock chamber. As the pressure in the load lock chamber is in the order of 10^{-8} mbar, the valves between load lock chamber, TPD chamber and vacuum suitcase can be opened and the sample can be transferred onto the temperature controlled sample stage. The sample is cooled down by a flow of liquid nitrogen inside the cooling box behind the sample stage and heated up by direct resistive heating.

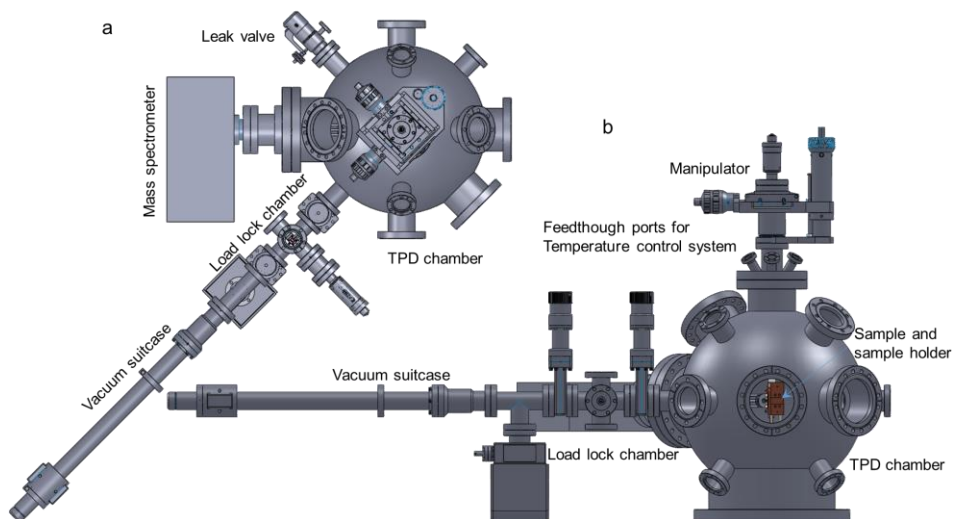


Figure 2.29 Top view (a) and a side view (b) of the TPD setup.

The sample is cleaned by a flash heating process to 700 K to desorb all contaminations on the silicon oxide surface in the TPD chamber with base pressure below 6×10^{-10} mbar. The cleaned sample is then transferred to the vacuum suitcase and kept inside the vacuum suitcase with base pressure below 1×10^{-10} mbar during the transfer between the TPD setup to the cluster source. The vacuum suitcase is composed of a transfer rod as a sample storage space, an ion pump, and a gate valve. Once the sample is prepared, the sample is placed back onto the sample holder. The molecule of interest is introduced into the TPD chamber by a leak valve and guided to the sample surface via a gas doser. The molecules are adsorbed on the sample at 100 K and the molecule coverage is fine-tuned by the molecule partial pressure and the exposure time. In order to obtain the conversion rate of the molecule on the sample surface, the sample is saturated with more than 1 Langmuir units ($1 \text{ L} = 1 \times 10^{-6}$ torr second) of molecule. The catalytic activity is evaluated by ramping the sample temperature with a linear ramping rate to 500 K and monitored by a QMS.

2.8.2 Sample holder and sample stage

A temperature controlled and transferable sample holder as well as a sample stage was designed and constructed. The guidelines of this design are: first, reducing the mass of the sample holder and sample stage to cool the sample efficiently; second, using chemically inert materials to minimize the influence from sample holder and sample stage; third, integrating temperature measuring and sample heating components onto the

transferable sample holder. A schematic drawing of the sample holder is shown in Figure 2.30.

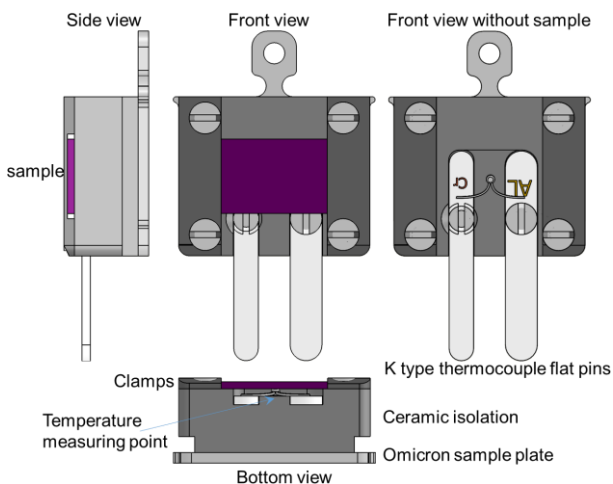


Figure 2.30 Schematic drawing of the sample holder with side, front and bottom views.

In order to make the sample holder compatible with the cluster sources, a stainless steel Omicron sample plate is used as a base. The sample is isolated by a ceramic block with built in thermocouple plugs to the sample stage and a measurement point in direct contact with the back side of the sample. The measurement point is composed of a set of welded k type thermocouple wires for wide temperature measurement range and is serving as a spring to have a proper contact with the sample. The signal of the thermocouple is transferred to a pair of thermocouple flat pins. The sample is clamped by two stainless steel plates to hold it in place and these two clamps are also used as electrodes allowing current to go through the sample. The power applied to the sample is proportional-integral-derivative (PID) controlled by a power supply via the clamps to perform linear temperature ramping.

The sample holder can be transferred inside the vacuum chambers and fitted in a sample holder slot on the sample stage. A schematic drawing of the sample holder is shown in Figure 2.31. The main components of the sample stage are a copper cooling box with two LN₂ flow tubes and a ceramic based sample slot.

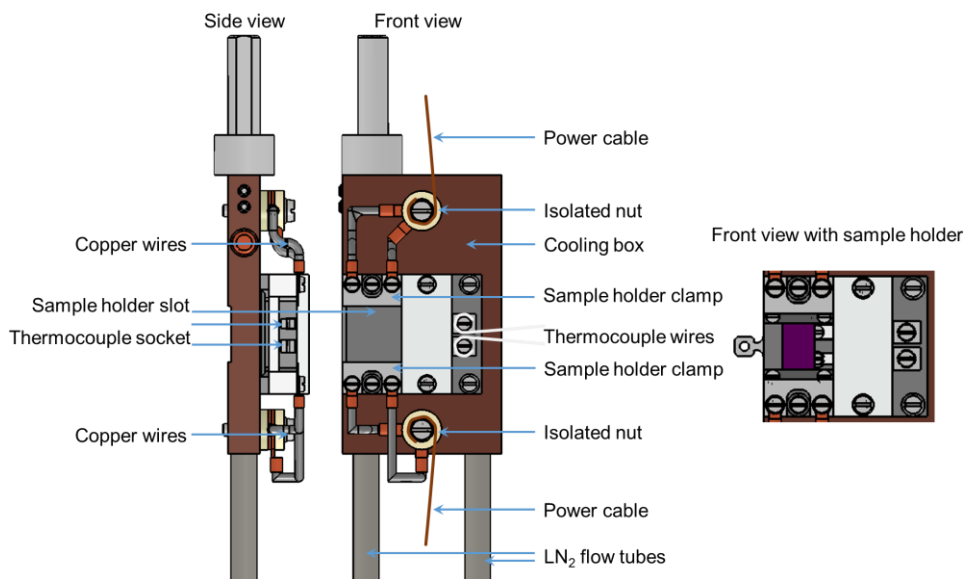


Figure 2.31 Schematic drawing of the sample holder with side and front views as well as a front view with sample holder in the sample slot.

The copper cooling box is cooled down by a flow of LN₂ introduced inside the box by two flexible stainless steel tubes. When the sample is inserted inside the sample holder slot, it is cooled by contact with the clamps on the sample holder and the four copper wires. These four wires are also used to transfer power to the sample. There is a thermocouple socket composed of two spring-like thermocouple slots inside the sample holder slot to connect with the flat pins for signal readout. The sample can be cooled down from room temperature to 100 K in 30 minutes and it can be ramped up to 900 K with 4 K/s ramping rate.

Chapter 3

Composition-dependent spatial atomic arrangement in $\text{Au}_x\text{Ag}_{1-x}$ bimetallic nanoparticles controlled at the nucleation stage

The results presented in this chapter are based on:

Unravelling the nucleation mechanism of bimetallic nanoparticles with composition-tunable core-shell arrangement

Ting-Wei Liao,^a Anupam Yadav,^a Kuo-Juei Hu,^{a,b} Johan van der Tol,^a Salvatore Cosentino,^a Francesco D'Acapito,^c Richard E. Palmer,^d Cristina Lenardi,^e Riccardo Ferrando,^f Didier Grandjean^a and Peter Lievens^a

Nanoscale, [DOI:10.1039/C8NR01481G](https://doi.org/10.1039/C8NR01481G) (2018)

- ^a Laboratory of Solid-State Physics and Magnetism, KU Leuven, Belgium.
- ^b Nanoscale Physics Research Laboratory, School of Physics and Astronomy, University of Birmingham, United Kingdom.
- ^c CNR-IOM-OGG c/o ESRF LISA CRG - The European Synchrotron, France.
- ^d College of Engineering, Swansea University, United Kingdom
- ^e CIMaNa and Physics Department, Università degli Studi di Milano, Italy
- ^f Dipartimento di Chimica e Chimica Industriale dell'Università di Genova, Italy

P. L., D. G. and T.-W. L. designed the project. T.-W. L. and A. Y. synthesized and deposited bimetallic nanoclusters. T.-W. L. and J. v. d. T. developed the method to extract the composition information from the RTof and the fitting program was written by J. v. d. T., K.-J. H. and R. P. carried out the STEM measurements. J. v. d. T. wrote a program to obtain the composition information of nanoclusters. T.-W. L. and C. L. carried out the XPS measurements and analysed the results. T.-W. L., A. Y., D.G. and F. D'A. carried out and analysed the results of the EXAFS measurements. R. F. performed the DFT calculations. All authors contributed to writing and proofreading of the manuscript.

Abstract The structure and atomic ordering of Au-Ag nanoparticles grown in the gas phase are determined by a combination of HAADF-STEM, XPS and Refl-XAFS techniques as a function of composition. It is shown consistently from all the techniques that an inversion of chemical ordering takes place by going from Au-rich to Ag-rich compositions, with the minority element always occupying the nanoparticle core, and the majority element enriching the shell. With the aid of DFT calculations, this composition-tunable chemical arrangement is rationalized in terms of a four-step growth process in which the very first stage of the cluster nucleation plays a crucial role. The four-step growth mechanism is based on mechanisms of general character, likely to be applicable to a variety of binary systems besides Au-Ag.

3.1 Introduction

To extend the range of properties of intermetallic nanomaterials and their performance, a detailed understanding of their structures and mechanisms behind their formation is needed. In particular, the influence of the very initial stage of nanoparticle nucleation, in which few atoms meet and form a small growing nucleus, has not yet been studied experimentally at the atomic level. An important issue, which arises in this context, is whether this initial nucleation stage can be decisive for determining the atomic arrangement of the resulting nanoparticles at the end of their growth process. Here, we consider the growth of $\text{Au}_x\text{Ag}_{1-x}$ bimetallic nanoclusters⁷⁹⁻⁸⁰ (BNCs) produced by cluster beam deposition (CBD), in which a binomial theorem composition analysis method is proposed to precisely determine and adjust the composition, for x from 0.1 to 0.9, prior to deposition. Combination of scanning transmission electron microscopy (STEM), X-ray photoelectron spectroscopy (XPS) and reflection X-ray absorption fine structure spectroscopy (Refl-XAFS) indicate that the resulting nanoparticles always have mixed cores and nearly pure shells, with the minority component always enriching the core but being scarce in the shell. This surprising inversion of chemical ordering depending on composition is explained by a four-step growth process of general character in which the very initial stage of the growth plays a major role. This explanation is supported both by mass spectrometry experiments and Density Functional Theory (DFT) calculations.

BNCs⁷⁹⁻⁸⁰ have long been a subject of intense study for their unique plasmonic,⁸¹ catalytic,^{34, 82} electronic and magnetic⁸³ properties distinct from those of the bulk materials and their monometallic counterparts. These properties not only depend on BNP size⁸⁴⁻⁸⁵ and composition⁸⁶⁻⁸⁷ but also on their structural organization at the atomic level.⁸⁷⁻⁸⁸ Spatial atomic distribution in BNCs plays a pivotal role in defining the geometric and electronic structure of their surface, which in turn determines their physicochemical properties.⁸⁹⁻⁹⁰ As a large variety of chemical arrangements,⁷⁹⁻⁸⁰ such as mixed alloy, core-shell, segregated subcluster, and onion-like, are possible for nanoalloys,

it is essential to understand and control the molecular mechanisms of synthesis to produce BNCs with the desired structure.⁹¹

Although BNCs with relatively uniform size, composition, and atomic arrangements can nowadays be synthesized by various colloidal synthetic protocols,⁹²⁻⁹³ very little is known of the underlying particle growth mechanisms. Recently, a clear impact of the nature of the pre-nucleation species in solution on the final BNCs composition and spatial arrangement was demonstrated.⁹⁴ However, due to the complexity of the growth process in solution,⁹⁵ uncovering the atomistic details of BNCs growth processes experimentally is still difficult^{94, 96} and theoretical models are rare.⁹⁷⁻⁹⁸ Experimental structural characterization of the (pre)nuclei and seeds formed during the nucleation process as well as of the final BNCs indeed remains a very challenging task.

To uncover the role composition plays on the final particle architecture, we have used a new synthesis approach allowing the production of BNCs free of surfactant with a precise control of composition and of nucleation and growth processes. CBD indeed greatly benefits from producing nanoclusters in a well-controlled noble gas environment and then soft-landing them on supports, while maintaining their preformed structure with excellent control over size and shape due to structural stability of the species present during the (pre)nucleation and growth stages in the gas phase.^{23, 99} Moreover, the CBD setup is equipped with RTof-MS that allows a very fine control over the composition (see experimental methods).

Among the large number of bimetallic systems Au-Ag¹⁰⁰⁻¹⁰¹ is widely studied for its full miscibility¹⁰² and its unique optical⁸¹ and catalytic^{34, 82} properties. The excellent plasmonic properties of Au NCs¹⁰³ can be further enhanced and tuned as a function of composition through alloying with Ag.^{87, 92} Enhanced catalytic activity and selectivity due to the synergistic effect of combining gold and silver has been reported.^{87, 104-105} Plasmon-mediated catalysis¹⁰⁶⁻¹⁰⁷ shows a clear “volcano type” relationship between chemical composition and catalytic activity of Au-Ag BNCs.¹⁰⁸ Finally Au-Ag BNCs are increasingly prominent in biomedicine¹⁰⁹ due to their photothermal properties,¹¹⁰ combined with the antibacterial properties of silver¹¹¹ and the easy functionalization of gold.¹¹² This suggests that a precise control over their composition and atomic arrangement could allow a fine-tuning of Au-Ag BNP properties.

Due to identical lattice constants for Au and Ag,¹¹³ direct lattice imaging of Au-Ag BNCs using TEM is not very informative and experimental reports on quantitative surface enrichment are rare.¹¹⁴⁻¹¹⁵ Element selective HAADF-STEM, XPS and XAFS spectroscopies have proven to be the most appropriate techniques to characterize with high accuracy the structure of Au-Ag BNCs.^{114, 116-117} In parallel, the stable atomic arrangements of the final BNCs have been extensively modelled theoretically¹¹⁸ with

unclear and sometimes contradictory results while no studies have been reported on their nucleation and growth processes.

In this work we use the build-in RTof-MS to determine the composition of the deposited BNCs with high precision using a method based on the binomial combination theorem. By using a combination of HAADF-STEM, XPS and Refl-XAFS, the tunable spatial architecture and the interatomic charge transfer in the final Au-Ag BNCs as a function of composition is unravelled. The role of the nucleation stage in controlling this final spatial architecture of the BNCs is highlighted with the aid of DFT-based theoretical calculations and a four-step growth process is proposed.

3.2 Experimental details

Production of composition controlled nanoclusters. Composition controlled Au-Ag BNCs are produced by pulsed laser (7 ns, 10 Hz, Nd:YAG lasers, Spectra Physics, INDI) ablation of Au (purity 99.995%) and Ag (purity 99.95%) or Au-Ag alloy (35 at% Au and 65 at% Ag, purity 99.95%) plate targets and inert gas (He, purity 99.9999%) condensation. The hot gas of metal monomers resulting from the pulsed laser ablation of the adequate metal targets confined in a small chamber undergoes aggregation upon cooling down in a 125 μ s pulse of high-purity He (9 bar). Figure 3.1 is a full mass spectrum of $\text{Au}_x\text{Ag}_{1-x}$ nanoclusters and it shows the production of a majority of large nanoclusters and a small number of their small and ultra-small counterparts.

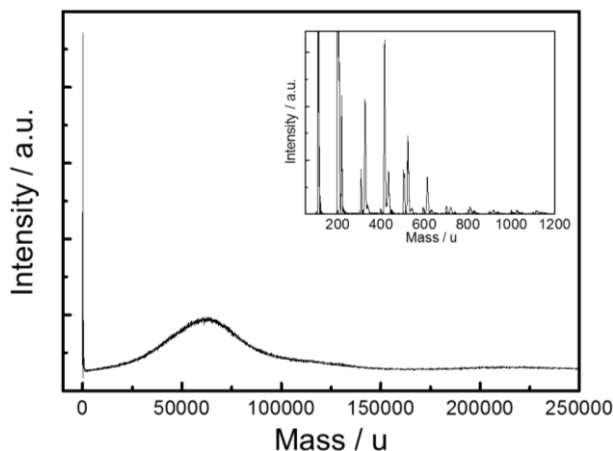


Figure 3.1 Full RTof mass spectrum of $\text{Au}_x\text{Ag}_{1-x}$ nanoclusters taken from Au-Ag alloy target 35 at% Au and 65 at% Ag from few atoms region to the main production region.

Without mass selection, nanoclusters are formed with sizes ranging from a few atoms to 1000 atoms.⁵² In this study, the cluster production is optimized for nanoclusters of

about 1000 atoms. By fine-tuning the laser powers, the abundance of the two elements can be controlled and composition controlled BNCs are formed. The cluster source is cooled by liquid nitrogen, resulting in nanoclusters with a temperature of about 100 K. After expansion into vacuum, a molecular beam of nanoclusters with different charge states is obtained, which is then soft-landed (~ 500 m/s) on an inert amorphous carbon film (~ 20 nm) covering a 200 mesh Cu TEM grid commercially available from EMS for STEM characterization or on 5 cm long \times 2 cm wide SiO₂ wafers in a UHV cluster beam deposition chamber with a base pressure below 5×10^{-10} mbar.¹¹⁹ Most of the nanoclusters (up to 90%) forming the cluster beam are neutral. The cluster beam size is 1 cm in diameter and the typical cluster flux is around 0.1 ML/min at the deposition stage 1 m downstream of the source. The dimension of the Refl-XAFS samples is 5 cm long \times 2 cm wide, therefore, the depositions require movement of the sample stage to cover the 5 cm wafer, with a motorized 1 mm/s travel speed.

Reflectron time of flight mass spectrometry. Charged nanoclusters formed directly in the source or neutral nanoclusters that are post-ionized by pulsed F₂ excimer laser (10 Hz, Lambda Physik OPTEx) photons (photon energy 7.9 eV, wavelength 157 nm) are subsequently accelerated electrostatically and mass analysed by reflectron time-of-flight mass spectrometry with a mass resolution $M/\Delta M \approx 150$ at 591 u and $M/\Delta M \approx 250$ at 1970 u. A detailed description of RTofF is presented in section 2.2. A composition analysis method based on the binomial theorem analysis of the ultra-small cluster region of the mass spectra was developed to determine the composition of the Au-Ag nanoclusters with high precision. With the direct proportionality of the intensity of each MS peak to the abundance of each type of BNCs and by assuming an identical ionization probability for nanoclusters with the same number of atoms N , such as Au _{N} , Au _{$N-1$} Ag₁, Au _{$N-2$} Ag₂, Au _{$N-3$} Ag₃..., the intensity, $I_{Au_{N_{Au}}Ag_{N_{Ag}}}$ of the Au _{N_{Au}} Ag _{N_{Ag}} cluster with N_{Au} number of Au atoms and N_{Ag} number of Ag atoms can be described by a binomial combinatorial relationship:

$$I_{Au_{N_{Au}}Ag_{N_{Ag}}} \propto \frac{(N_{Au}+N_{Ag})!}{N_{Au}!N_{Ag}!} [Au]^{N_{Au}} [Ag]^{N_{Ag}}, \quad 3.1$$

where $[Au]$ and $[Ag]$ are the normalized atomic fractions of Au and Ag elements, respectively.

Experimental RTofF-MS spectra for each cluster composition were fitted to equation (1) using an in-house developed program to determine with high precision the global average composition of 4 to 15-atom ultra-small nanoclusters. An example of the excellent match between the experimental and the simulated spectra corresponding to a global composition of $73.8 \pm 0.4\%$ Au and $26.2 \pm 0.4\%$ of Ag (Au_{0.7}Ag_{0.3}) is shown in Figure 3.2.

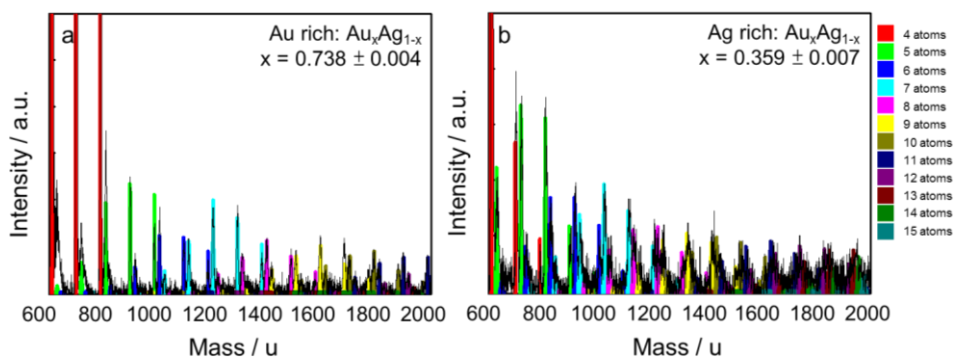


Figure 3.2 RTOf-MS of deposited $\text{Au}_x\text{Ag}_{1-x}$ nanoclusters, (a) and (b) mass spectra of 73.8 ± 0.4 at% Au and 26.2 ± 0.4 at% Ag as well as 35.9 ± 0.7 at% Au and 64.1 ± 0.7 at% Ag combined with simulation spectra.

Similarly simulation of the mass spectrum corresponding to nanoclusters produced by laser ablation of an $\text{Au}_{0.4}\text{Ag}_{0.6}$ alloy target of defined composition (35.4% Au and 64.6% Ag, ACI alloy) (Figure 3.2b) shows that the simulated composition of $\text{Au}_{0.4}\text{Ag}_{0.6}$ ($35.9 \pm 0.7\%$ Au and $64.1 \pm 0.7\%$ Ag), closely matches the original stoichiometry of the alloy targets supporting the validity of our approach.²³⁻²⁴ A very close composition ($38\% \pm 4\%$ Au and $62\% \pm 4\%$ Ag) was also determined for the corresponding Au-Ag BNCs deposited on SiO_2 wafer by Rutherford backscattering spectrometry (RBS) confirming the conservation of the composition of Au-Ag gas-phase nanoclusters upon their soft landing as Au-Ag BNCs onto SiO_2 wafers.

Based on the developed method, the composition of BNCs can be monitored in real time by assuming a regular binomial distribution of the cluster compositions, and a series of simulated spectra from 0% to 100% of Ag with a 0.1% increment is made. The simulated spectra are then least-square-fitted to the measured mass spectrum, with the Au-Ag composition as the unknown fit parameter, using an in-house developed program. A validation of the fitting method applied on a series of mass spectra of $\text{Au}_x\text{Ag}_{1-x}$ is shown in Figure 3.3.

Rutherford backscattering spectroscopy. Rutherford backscattering spectroscopy experiments were performed to confirm the composition of the deposited $\text{Au}_x\text{Ag}_{1-x}$ BNCs by using a collimated mono-energetic He^+ beam accelerated by a dual Pelletron and steered into a scattering chamber. In this study, the 10 nA He^+ beam was focused to 2 mm^2 with kinetic energy in 1.57 MeV. The scattered He^+ beam was detected by a silicon surface barrier detector located at 15° to the surface normal. The RBS results of deposited $\text{Au}_x\text{Ag}_{1-x}$ BNCs are shown in Figure 3.4. A detailed description of RBS is presented in section 2.3.

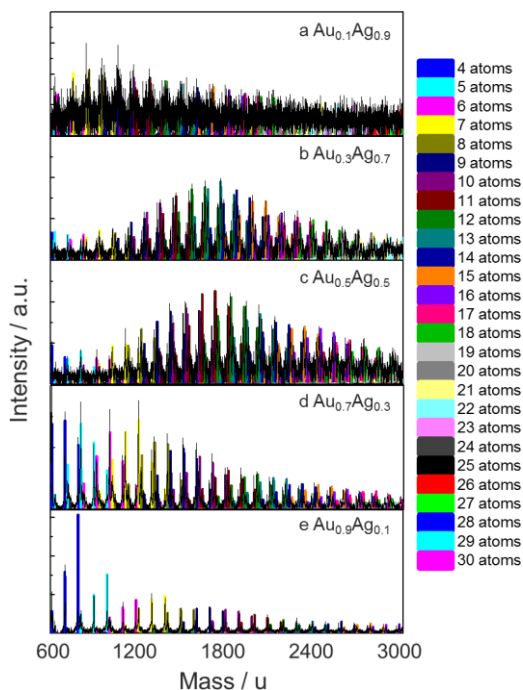


Figure 3.3 Validation of the fitting based on binomial theorem composition analysis method was done with additionally compositions obtained from the analysis of the mass spectra within the mass range from 600 u to 3000 u (4 atoms to 30 atoms) of a series Au_xAg_{1-x} nanoclusters produced from Au_xAg_{1-x} alloy targets of known stoichiometries ($x = 0.1, 0.3, 0.5, 0.7$ and 0.9). It is showed always a very good agreement with the target composition. The corresponding composition fitting are shown above in the mass range from 600 u to 3000 u, $x = 0.9$ (a), 0.7 (b), 0.5 (c), 0.3 (d) and 0.1 (e).

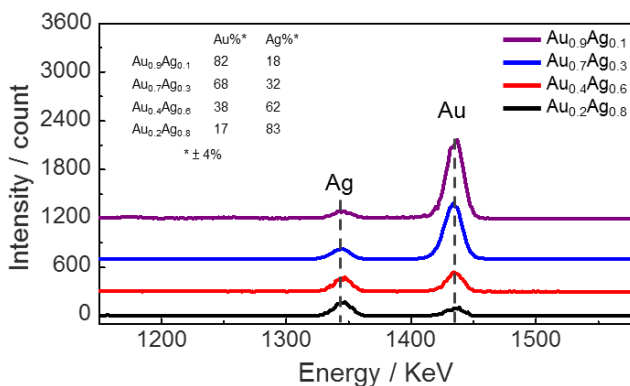


Figure 3.4 RBS spectra of deposited Au_xAg_{1-x} BNCs from gold rich to silver rich on SiO_2 wafers. The inset table shows the overall composition of deposited nanoclusters as determined by RBS.

STEM measurements. Atomic resolution STEM imaging was performed by a JEOL JEM 2100F STEM instrument operating at 200 keV equipped with a spherical aberration (Cs) probe corrector (CEOS GmbH) and high-angle annular dark-field (HAADF) detector, with inner and outer collection angles of 62 and 164 mrad. The cluster size distribution of the Au-Ag BNCs were measured with low magnification images for more than 100 BNCs. The cluster size was determined by measuring the diameter cross-section of individual nanoclusters. Assignment of core-shell structure was possible because of the Z-contrast of HAADF-STEM (Z is the elemental atomic number). The HAADF-STEM intensity is proportional to $Z^{1.46}$ with the camera length employed.¹²⁰ The large difference of the atomic number between Au and Ag ($Z_{\text{Au}} = 79$; $Z_{\text{Ag}} = 47$) allows us to distinguish the elemental atomic arrangement within the nanoclusters directly from HAADF-STEM image intensity contrast. The STEM image analyzes were carried out with the imageJ Fiji software.¹²¹ The intensity profile of each single cluster was obtained by first finding the position of the centre through averaging, and then binning the intensity in polar coordinates as a function of the radial distance to the centre.

XPS measurements. XPS experiments were performed at room temperature under UHV conditions (Leybold LHS 10/12, $5 \cdot 10^{-9}$ mbar) by using an Al $K\alpha$ X-ray source operated at 10 kV and 25 mA and the spectra were collected by hemispherical analyser with passing energy 30 eV and energy step 0.025 eV. The spectra were aligned to the adventitious carbon peak C 1s placed at 284.8 eV. The fitting of the peaks was done with Unifit software. Following spin-orbit coupling constrains were considered: peaks separation 6.0 eV and 3.65 eV as well as peak area ratio 2/3 and 3/4 for Ag and Au, respectively.

XAFS measurements. XAFS experiments were performed in total reflection in fluorescence detection mode at Ag K-edge (25514 eV) on BM08-LISA beamline at The European Synchrotron (ESRF, Grenoble, France). 5 cm long \times 2 cm wide SiO_2 ultra-flat wafers covered with 0.3 atomic monolayer (ML) nanoclusters were mounted on a z - θ goniometer with the sample surface parallel to the ring orbital plane. The impinging beam was about 50 μm (v) \times 2mm (h) and its intensity before and after the sample was collected with ion chambers filled with Ar gas. For each sample a reflectivity spectrum was collected and the data collection angle was defined as about 80% of the critical value for total external reflection. In this way the X-ray beam probes only a few nm below the surface enhancing the signal from the overlayer and minimizing that of the substrate.

The X-ray fluorescence yield from the Ag- K_{α} line was collected using a multi-element HP-Ge detector array. Due to the limited fluorescent yield of Au L_3 edge, that would have required excessive measurement times, no data could be obtained at Au L_3 edge with this dilution.

Data reduction of the experimental X-ray absorption spectra was performed with the program EXBROOK.⁷⁷ Background subtraction and normalization was carried out by fitting (i) a linear polynomial to the pre-edge region in order to remove any instrumental background and absorption effects from other edges and (ii) cubic splines simulating the absorption coefficient from an isolated atom to the post-edge region. XAFS refinements were performed with the EXCURVE package.⁷⁷ Phase shifts and backscattering factors were calculated ab initio using Hedin-Lundqvist potentials. Fourier-transformation was applied to convert the k space spectra to r space with k^3 weighting to compensate for the dampening of the XAFS amplitude with increasing k. The structural models were built up with silver and surrounding atoms such as silver, gold and oxygen. The fitting results are presented in Table 3.1 and Figure 3.5. The amplitude reduction due to many-electron processes (AFAC) was set to 0.9 after calibration with a silver metal foil.

Table 3.1 Summary of structural results of Ag K-edge XAFS refinements of Au-Ag BNCs on SiO₂ wafer measured in full reflection and fluorescence-detection mode.

	Shell	Coordination number N	Bond distance R (Å)	Debye-Waller factor A (Å ²)	E _f (eV)
Au _{0.9} Ag _{0.1}	Ag-Ag	0.9 (1)	2.91 (3)	0.03 (2)	0.0(9)
	Ag-Au	3.6 (5)	2.84 (2)	0.013 (4)	
	Ag-O	0.4 (1)	2.23 (2)	0.008 (4)	
Au _{0.7} Ag _{0.3}	Ag-Ag	1.0 (4)	2.89 (3)	0.012 (5)	-0.4(9)
	Ag-Au	1.7 (4)	2.88 (3)	0.012 (6)	
	Ag-O	0.2 (1)	2.22 (6)	0.01 (1)	
Au _{0.5} Ag _{0.5}	Ag-Ag	1.0 (1)	2.85 (2)	0.010 (3)	-1.2(9)
	Ag-Au	1.1 (1)	2.88 (2)	0.011 (4)	
	Ag-O	0.4 (1)	2.23 (3)	0.022 (6)	
Au _{0.3} Ag _{0.7}	Ag-Ag	4.0 (2)	2.83 (1)	0.016 (1)	-1.6(6)
	Ag-Au	3.0 (2)	2.88 (1)	0.013 (2)	
	Ag-O	0.4 (1)	2.24 (2)	0.019 (6)	
Au _{0.1} Ag _{0.9}	Ag-Ag	1.2 (2)	2.83 (3)	0.020 (8)	2.6(9)
	Ag-Au	1.6 (3)	2.86 (2)	0.017 (6)	
	Ag-O	1.2 (2)	2.20 (2)	0.02 (1)	

E_f = contribution of the wave vector of the zero photoelectron relative to the origin of k [eV]

N = number of atoms in the shell

R = radial distance of atoms in the shell [Å]

A = Debye-Waller term of the shell ($A = 2\sigma^2$ with σ = Debye-Waller factor)[Å²]

R factors were ranging from 39 to 73 %.

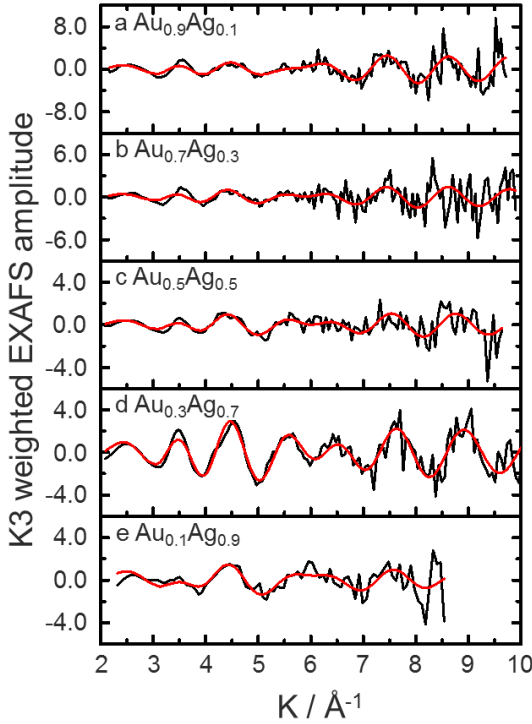


Figure 3.5 k^3 weighted XAFS spectra of the Au_xAg_{1-x} BNCs on SiO_2 wafers from $x = 0.9$ to 0.1 . The corresponding phase-corrected Fourier transformed EXAFS spectra are shown in Figure 3.10-a.

DFT calculations. Spin unrestricted calculations were performed within the Density Functional Theory (DFT) approach implemented in the Quantum-Espresso package¹²² with available ultrasoft pseudopotentials.¹²³ For exchange and correlation, the spin unrestricted Generalized Gradient Approximation in the Perdew–Burke–Ernzerhof¹²⁴ implementation was used. For the selection of the plane waves, energy cutoffs of 40 and 160 Ry were chosen to describe the wave function and the electronic density, respectively. Convergence tests were made using cutoffs of 60 and 240 Ry. The mixing energy is defined here as the binding energy of mixed nanoclusters with reference to the binding energy of the corresponding monometallic nanoclusters, and hence can be written as:

$$E_{mix(Au_mAg_n)} = E_{b(Au_mAg_n)} - \frac{m}{N}E_{b(Au_N)} - \frac{n}{N}E_{b(Ag_N)}, \quad 3.2$$

where E_b is the binding energy and $N = m + n$ is the total number of atoms. If $E_{mix(Au_mAg_n)} < 0$, the formation of a collection of N Au_mAg_n BNCs is energetically more favorable than that of a collection of m $Au_N + n$ Ag_N monometallic nanoclusters. By

contrast, if $E_{mix(Au_mAg_n)} > 0$, the formation of a collection of monometallic nanoclusters is energetically more favourable than that of their bimetallic counterparts.

3.3 Production of composition controlled Au_xAg_{1-x} bimetallic nanoclusters

A series of Au_xAg_{1-x} nanoclusters from gold rich to silver rich stoichiometries were produced in the gas-phase by dual-laser ablation of pure Ag and Au metal targets and condensation in high pressure (~ 9 bar) helium gas.²¹ The nanoclusters were carried out of the source by the helium pulse at supersonic speeds and the formed beam is directed into the extraction region of the RToF-MS, where the nanoclusters are photoionized with an excimer laser. The obtained mass spectrum was used to determine with high precision the cluster sizes and compositions present in the chamber at the end of the nucleation / growth process (Figure 3.1). The precise required composition of Au-Ag nanoclusters was obtained by modulating the laser intensities ablating the two targets independently to produce $Au_{0.9}Ag_{0.1}$, $Au_{0.7}Ag_{0.3}$, $Au_{0.5}Ag_{0.5}$, $Au_{0.4}Ag_{0.6}$, $Au_{0.3}Ag_{0.7}$, $Au_{0.2}Ag_{0.8}$, and $Au_{0.1}Ag_{0.9}$ by a composition analysis of the ultra-small cluster region of the mass spectra based on the binomial theorem (see experimental details).

The average diameter of the BNCs, measured for more than 100 NCs, was 3.0 ± 0.7 nm in Au rich BNCs and 3.4 ± 0.7 (3.7 ± 0.8) nm in Ag rich $Au_{0.4}Ag_{0.6}$ ($Au_{0.2}Ag_{0.8}$) BNCs. Histograms of diameter distributions of Au_xAg_{1-x} BNCs, Figure 3.6, show a sharp increase of the BNP diameter in silver-rich compositions due to their flattening on the support.

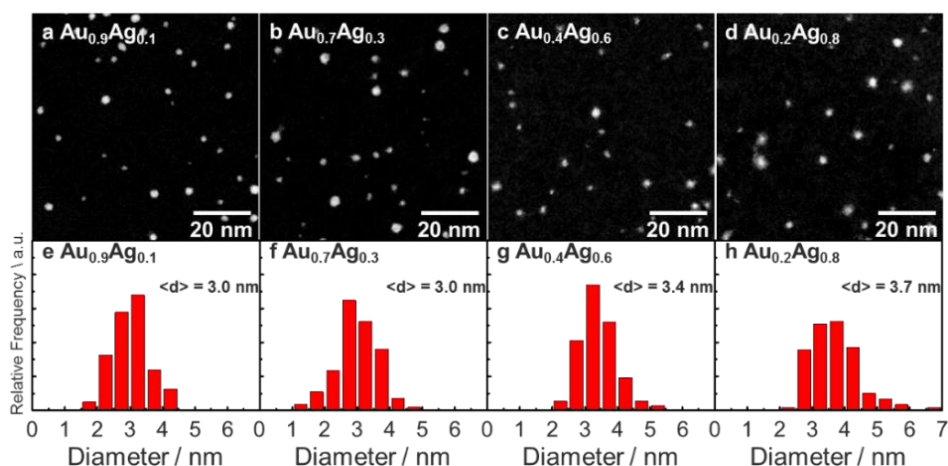


Figure 3.6 STEM images and histograms of diameter distributions of Au_xAg_{1-x} BNCs: (a, e) $Au_{0.9}Ag_{0.1}$; (b, f) $Au_{0.7}Ag_{0.3}$; (c, g) $Au_{0.3}Ag_{0.7}$; (d, h) $Au_{0.2}Ag_{0.8}$.

3.4 Phase segregated $\text{Au}_x\text{Ag}_{1-x}$ bimetallic nanoclusters

To unravel the atomic arrangements of Au and Ag atoms in Au-Ag BNCs as a function of their composition, gas-phase $\text{Au}_x\text{Ag}_{1-x}$ nanoclusters ($x = 0.2, 0.4, 0.5, 0.7$ and 0.9) were deposited directly on TEM grids to yield random arrays of Au-Ag BNCs. They were investigated by STEM-HAADF, whose signal brightness is proportional to $Z^{1.46}$.¹²⁰ Due to the large Z difference between Au (79) and Ag (47) a strong contrast between brighter gold-rich and darker silver-rich areas is expected in the STEM images.

Figure 3.7 presents STEM images of Au-Ag BNCs along with their normalised quantitative radial intensity profile integrated over the polar coordinate and simulated STEM radial profiles corresponding to pure Au NPs, pure Ag NPs and phase segregated structures. Detailed inspection of the STEM images shows that for all compositions except $\text{Au}_{0.5}\text{Ag}_{0.5}$ a contrasted dark core / bright shell or bright core / dark shell pattern is observed, while for the case of $\text{Au}_{0.5}\text{Ag}_{0.5}$, a uniform intermediate intensity prevails over the whole cluster. This indicates different levels of mixing and atomic arrangements are occurring in the deposited nanoclusters as a function of their composition.

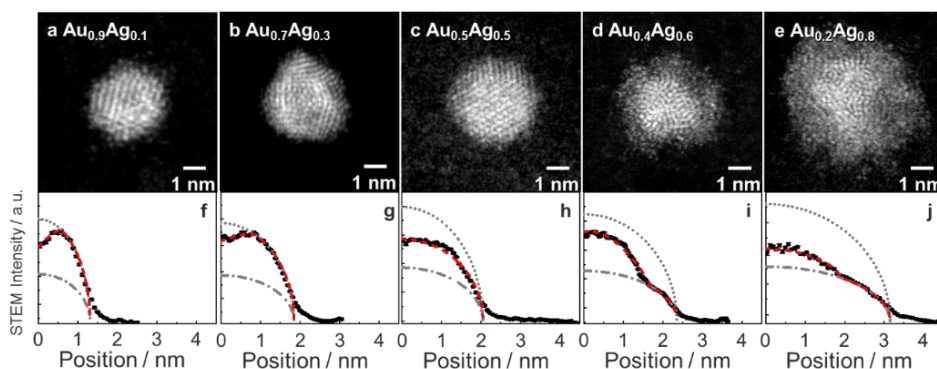


Figure 3.7 Example of detailed HAADF-STEM images of $\text{Au}_x\text{Ag}_{1-x}$ BNCs with simulation results also shown alongside: (a, f) $\text{Au}_{0.9}\text{Ag}_{0.1}$; (b, g) $\text{Au}_{0.7}\text{Ag}_{0.3}$; (c, h) $\text{Au}_{0.5}\text{Ag}_{0.5}$; (d, i) $\text{Au}_{0.4}\text{Ag}_{0.6}$; (e, j) $\text{Au}_{0.2}\text{Ag}_{0.8}$. The HAADF-STEM radial intensity profiles are taken from the center to the edge of the cluster and integrated from 0° to 360° . The red dash lines are the simulations of cluster STEM intensity with gradient composition evolution. The grey dotted lines and grey dash dotted lines are simulated STEM intensities with pure Au nanoclusters and pure Ag nanoclusters, respectively.

For gold rich BNCs the core appears darker than the shell, while for silver rich ones the reverse is observed showing a composition-tunable atomic arrangement. This is corroborated by the STEM profiles of the BNP cores that lie systematically between the simulated profiles of pure gold and pure silver indicating that the composition of the cluster core is always enriched by the minority element, i.e. silver in gold rich BNCs ($x = 0.9$ and 0.7) and gold in silver rich nanoclusters ($x = 0.4$ and 0.2).

Detailed information on the composition variation along the radius of each BNP was obtained by simulating³² the STEM signal intensity with different Au-Ag compositions from the centre to the edge of the BNCs. The obtained results are presented in Figures 1f to 1j and indicated with red dash lines. In all the investigated BNCs, except in Au_{0.5}Ag_{0.5}, the core composition varies as a function of the position along the BNP radius. In gold rich Au_{0.9}Ag_{0.1} the centre of the cluster is composed of ca. 95% of Ag and the silver concentration decreases along the radius to reach 0% at a distance of 0.7 nm from the BNP centre. On the other hand, in silver rich Au_{0.2}Ag_{0.8}, the centre core is composed of ca. 90% Au and the Au concentration reaches 0% at 1.8 nm from the BNP centre.

The predominant location of Ag at the surface of the BNP in silver-rich compositions is further confirmed by the presence of an amorphous and highly dispersed phase around the NP metallic core in the STEM images of Au_{0.1}Ag_{0.9} and to a lesser extent of Au_{0.3}Ag_{0.7} BNCs (see Figure 3.7-i and Figure 3.7-j). The absence of this phase in gold-rich BNCs is likely due to the presence of a majority of gold atoms at the surface of the BNCs, forming sharp atomic planes and edges observed in the STEM images. This is also in line with the BNP size analysis shown in Figure 3.6, where an increase in the apparent average diameter in Au_{0.1}Ag_{0.9} is observed, likely due to the presence of this amorphous oxide outer shell.

Detailed analysis of the STEM-HAADF images clearly shows the presence of a stable composition-tunable spatially segregated atomic arrangement in ca. 3 nm bimetallic Au_xAg_{1-x} with the minority element always preferentially located in the core of the particle. When the two elements are in equal amounts a full mixing of Au and Ag is observed.

Additional information on the composition-tunable arrangement and the charge transfers occurring between Ag and Au atoms in Au_xAg_{1-x} ($x = 0, 0.1, 0.3, 0.5, 0.7, 0.9$ and 1) BNCs was obtained by XPS. Ag 3d and Au 4f split due to spin-orbit coupling into Ag 3d_{3/2}, Ag 3d_{5/2}, Au 4f_{5/2} and Au 4f_{7/2} peaks, respectively, and O 1s spectra with best fits are presented in Figure 3.8. Analysis of O 1s peaks shows that the main signal is from the SiO₂ support and a contribution of Ag oxide (AgO ca. 530 eV, Ag₂O ca. 529 eV) is only present in Ag rich BNCs ($x = 0$ and 0.1) with a contribution never exceeding 1% of the total O 1s peak. Analysis of the binding energy (BE) peak positions of Au 4f_{5/2}, Au 4f_{7/2}, Ag 3d_{3/2} and Ag 3d_{5/2} as a function of composition show that Ag 3d BE in all Au_xAg_{1-x} BNCs are always smaller than that of pure Ag NPs. As the Ag BE decreases with increasing oxidation state due to its core-level photoemission,¹²⁵⁻¹²⁶ this evolution points out a systematic partial electron transfer from Ag to Au atoms or to the SiO₂ support in all BNCs. This is further confirmed by the BEs of the Au 4f contribution showing the reduction of Au atoms by Ag in Au rich BNCs and their oxidation by electron

transfer to the support through the silver outer shell in their Ag rich counterparts, as reported previously.¹²⁷⁻¹²⁹

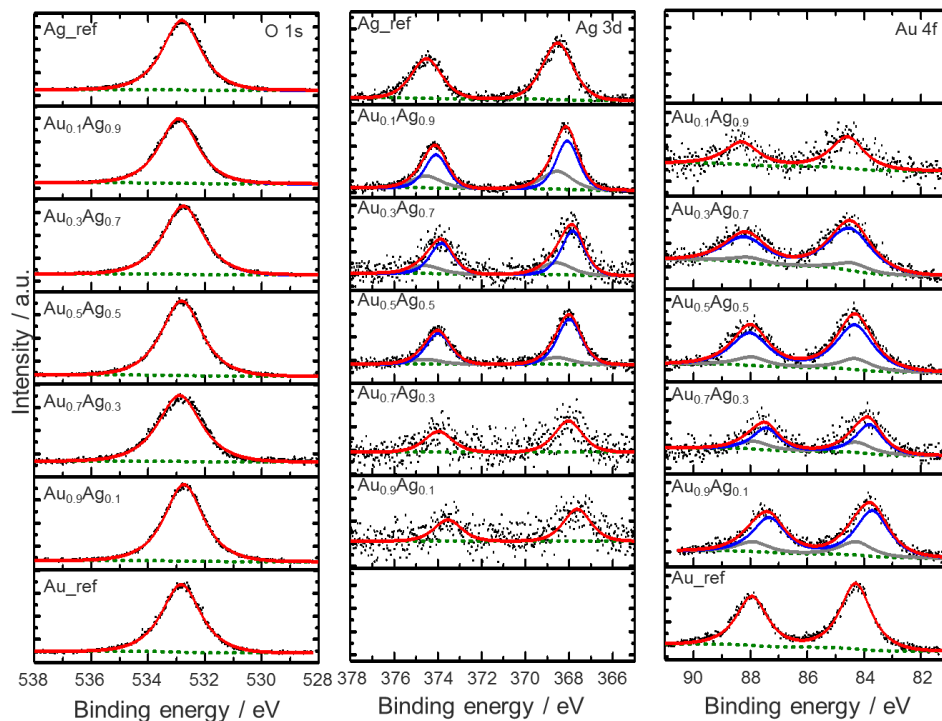


Figure 3.8 O 1s, Ag 3d and Au 4f XPS spectra of the $\text{Au}_x\text{Ag}_{1-x}$ BNCs on SiO_2 wafers from $x = 0.9$ to 0.1. The green dash lines are the Shirley backgrounds, the blue lines are pure phase of Au and Ag and the grey lines are the Au-Ag alloy phases.

The respective fractions of pure Au, pure Ag and Au-Ag alloyed phases present in all BNCs were examined by deconvoluting and fitting the Ag 3d and Au 4f peaks with two Ag and Au chemical components assigned to pure-phase Ag(0) and Au(0) peaks and an Au-Ag alloyed phase (Ag(δ) and Au(δ) peaks). The integrated peak area ratio of Ag(0) (368.5 eV and 374.5 eV) and Ag(δ) contributions (368.0 eV and 374.0 eV) in Ag 3d spectra and those of Au(0) (84.3 eV and 87.9 eV) and Au(δ) (83.7 eV to 84.6 eV and 87.3 eV to 88.3 eV) in Au 4f spectra, respectively, are presented in Figure 3.9. The results indicate that the minority element always tends to form an alloyed phase, while a large fraction (up to 40%) of the majority element forms a pure phase.

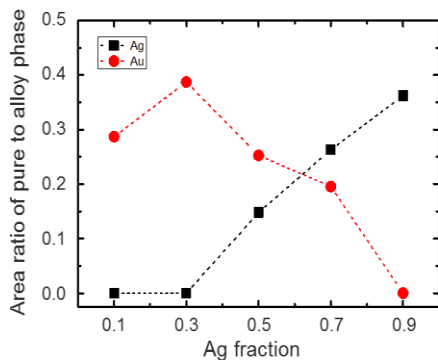


Figure 3.9 Integrated peak area ratio of the XPS of Ag(0), pure phase, to Ag(δ), alloy phase, (black square) plotted with those of Au(0), pure phase, to Au(δ), alloy phase, (red circle) from Au rich to Ag rich BNCs compositions.

3.5 Atomic arrangement in $\text{Au}_x\text{Ag}_{1-x}$ bimetallic nanoparticles

To further characterize the BNCs atomic arrangement, identify the different phases, and quantify the exact levels of mixing and segregation corresponding to the dark and bright regions in the final Au-Ag BNCs, we carried out a XAFS investigation of $\text{Au}_{0.9}\text{Ag}_{0.1}$, $\text{Au}_{0.7}\text{Ag}_{0.3}$, $\text{Au}_{0.5}\text{Ag}_{0.5}$, $\text{Au}_{0.3}\text{Ag}_{0.7}$, and $\text{Au}_{0.1}\text{Ag}_{0.9}$ nanoclusters deposited on inert SiO_2 at the Ag K-edge. Unlike XRD and conventional TEM, XAFS can detect alloying even in a few-atom size Au-Ag bimetallic system and even when the interatomic distances of the alloy and the pure metal are very similar.¹¹⁶ In the Au-Ag system, the interference between Ag and Au phase shifts indeed generates a characteristic beat in the XAFS that appears as a doublet in the Fourier transform.¹¹⁶ Moreover, analysis of the X-ray Absorption Near-edge Structure (XANES) can provide valuable information on the electronic properties of the BNCs and in particular on the electron transfer that is likely to occur between Au and Ag atoms.¹³⁰ The XAFS technique is also complementary to electron microscopy since it allows, as a bulk technique, the investigation of a more representative amount of nanoclusters. However, to ensure that the BNCs always stay isolated on the SiO_2 support, their coverage was kept to a very low value of 0.3 ML corresponding to an average inter BNP separation of around 7 nm. Due to this exceptionally high level of dilution the XAFS signal of the Au-Ag BNCs needed to be collected in total reflection mode. Although the relatively weak signal that was collected for this exceptionally high level of dilution (0.3 ML) produced a moderate signal-to-noise ratio, a reliable XAFS signal still could be obtained up to $k = 9.5 \text{ \AA}^{-1}$. Phase corrected Fourier Transforms (Figure 3.10-a) of the k^3 -weighted XAFS (Figure 3.5) show a doublet

between 2 and 3 Å that is characteristic of Au-Ag alloys with distinct shape and intensity ratios for each compound, evidencing that a significant level of Au-Ag atomic mixing exists in most of the investigated compositions.

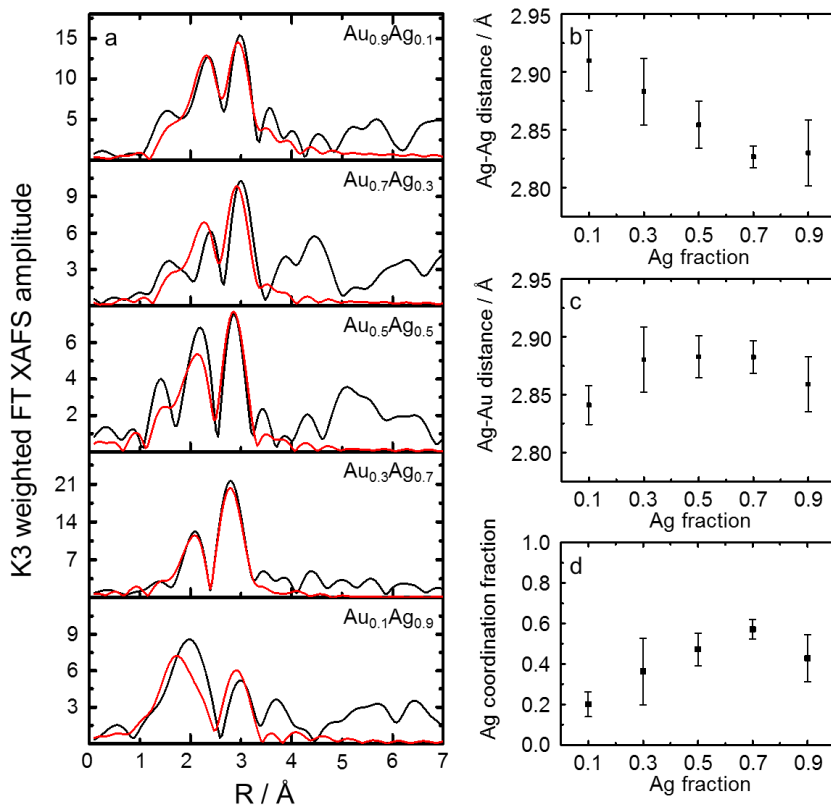


Figure 3.10 (a) Phase-corrected Fourier transformed XAFS spectra from gold rich to silver rich nanoclusters. Bond distances of Ag-Ag (b) and Ag-Au (c), and Ag coordination fraction (Ag coordination number over the sum of Ag and Au coordination numbers) as a function of composition (d).

Detailed fitting of the data was carried out with a 3-shell structure model based on Ag-Ag, Ag-Au, and Ag-O interactions. In general, the major part of the XAFS signal could be fitted with a combination of Ag-Ag and Ag-Au contributions with Ag-Au and Ag-Ag contributions dominating in gold-rich and silver-rich compositions, respectively. Metallic coordination numbers ($N_{\text{Ag-Ag}}$ and $N_{\text{Ag-Au}}$), obtained for these sizes in the spherical shape approximation, were generally smaller than expected, in particular in silver rich BNCs (see Table 3.1). This may indicate that BNCs have a significant level of segregation with a pure Au region in line with the XPS results and/or that the Au-Ag BNCs are rather disordered and/or flattened onto the support in line with AFM

measurements (Figure 3.11) that show a significant flattening of the Ag rich BNCs on the SiO₂ surface compared to their Au-rich counterparts. This is likely resulting from the formation of a superficial oxide phase, whose presence is evidenced by the minor Ag-O contributions detected mostly in Ag-rich BNCs with XPS. As Ag-O long bond distances ($R_{\text{Ag-O}} = 2.24$ to 2.20 Å) do not match those found in Ag₂O nor in AgO (2.04 Å),¹¹³ this oxide likely corresponds to an amorphous phase resulting from the interaction with the SiO₂ support of the large fraction of surface Ag atoms in absence of ligands. In silver rich Au_{0.1}Ag_{0.9} this O contribution was 3 times stronger than ($N_{\text{Ag-O}} = 1.2$) in the other BNCs compositions, while Ag-O distances were shortened. This points out the formation of *ca.* 60% ($N_{\text{Ag-O}} = 1.2 / N_{\text{Ag-O}}$ in Ag₂O or Ag/Si oxides¹¹³ = 2) of an highly dispersed Ag oxide phase at the BNP/support interface. This is also visible in the STEM-HAADF image of Au_{0.1}Ag_{0.9} and to a lesser extent of Au_{0.3}Ag_{0.7}. In gold-rich BNCs a limited amount of Ag oxide is found confirming the preferential location of silver in the BNP core where it is protected from oxidation by an outer shell of more noble gold metal. This Au shell confers gold-rich BNCs the compact shapes and sharp surface edges observed with STEM.

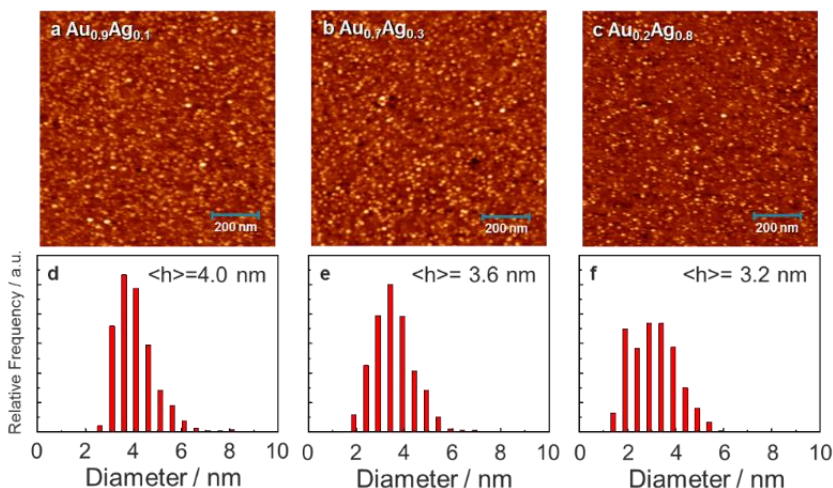


Figure 3.11 AFM images and height histograms of the 0.1 ML Au-Ag BNCs with different composition, Au_{0.9}Ag_{0.1} (a,d), Au_{0.6}Ag_{0.4} (b,e), Au_{0.2}Ag_{0.8} (c,f) deposited on SiO₂ wafers.

The evolution of metal-metal bond distances $R_{\text{Ag-Ag}}$ and $R_{\text{Ag-Au}}$ in Au-Ag BNCs as a function of Ag fraction are presented in Figures 3.10b and 3.10c. Whereas $R_{\text{Ag-Au}}$ is close to the bulk values of both metals (2.88 Å)¹¹³ for all compositions, $R_{\text{Ag-Ag}}$ is unusually long (2.91 Å) in gold-rich Au_{0.9}Ag_{0.1}, unusually short (2.83 Å) in silver-rich Au_{0.1}Ag_{0.9}, and close to the typical silver metal bulk value in Au_{0.5}Ag_{0.5}.¹³¹ These strong variations of bond distances suggest that the silver rich metal phase, unlike the Au-Ag alloy, might be located in very different spatial locations in the BNP depending on the composition. In

the core of $\text{Au}_{0.9}\text{Ag}_{0.1}$ the Ag-Ag bond distance is affected by charge transfer to the surrounding more electronegative Au atoms depleting their electron density and resulting in weaker and longer Ag-Ag bonds in line with the XPS results.

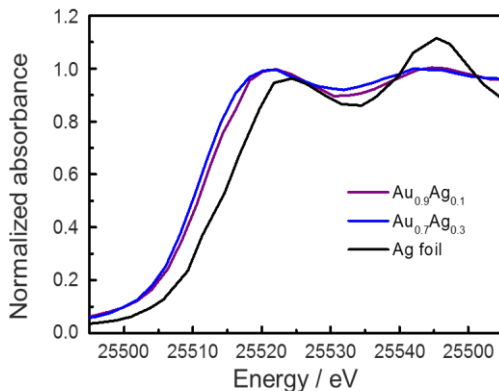


Figure 3.12 XANES spectra of gold-rich $\text{Au}_{0.9}\text{Ag}_{0.1}$ and $\text{Au}_{0.7}\text{Ag}_{0.3}$ BNCs along with Ag foil reference.

The charge transfer from Ag to Au atoms is indeed clearly visible in the XANES analysis of gold-rich $\text{Au}_{0.9}\text{Ag}_{0.1}$ and $\text{Au}_{0.7}\text{Ag}_{0.3}$ BNCs spectra presented in Figure 3.12. A strong white line corresponding to the presence of a larger amount of empty states in the 5p band that is shifting the edge position to lower energies (25510.2 eV) compared to that of metal foil (25514.0 eV). In the meantime, both BNCs feature a strong resonance at 25545.2 eV characteristic of Ag metal, confirming that in both BNCs the large majority of Ag atoms does not form an oxide. In line with the Ag 3d XPS results, this XANES red-shift indicates the formation of electron-depleted alloyed metallic Ag due to their transfer to gold atoms. This charge transfer, that is stronger in Au rich BNCs, is likely stabilizing the Ag core against the galvanic replacement reaction, which explains the stability of this atomic arrangement.^{127, 129} In contrast, in Ag-rich BNCs the nearly pure silver phase located in the outer shell of the BNP is likely undergoing a large surface tension that is shortening the Ag-Ag distances.¹³²⁻¹³³ The Ag coordination fraction number (ratio of Ag to the sum of Ag and Au coordination number) (Figure 3.10-d) increases monotonically as expected with the Ag fraction in gold rich nanoclusters and reaches a plateau in Ag rich compositions corresponding to the formation of an increasing amount of amorphous oxide phase.

Combining STEM-HAADF with XPS and XAFS spectroscopies allowed us to characterize the detailed atomic arrangements in Au-Ag BNCs deposited with CBD onto TEM carbon grids and SiO_2 wafers. Au-Ag BNCs are predominantly segregated with a

composition-tunable inversion of the relative position of Ag and Au, *i.e.*, the less abundant element is always located in the core forming an alloy while the most abundant one is in the outer shell of the BNP with a significant fraction (up to 40%) forming a pure phase at the surface. Due to the lack of protecting ligands, a limited fraction of the Ag atoms located at the BNP surface forms a dispersed amorphous oxide phase. Although two different supports were used for STEM and for XPS and Refl-XAFS spectroscopies, all techniques show for each composition similar structures. This suggests that the atomic arrangement of Au and Ag atoms in metallic BNCs is not significantly influenced by the deposition but may be determined at an earlier stage of the nucleation and growth stage occurring in the gas-phase before their deposition.

To test this hypothesis and better understand how the composition directly tunes the very different atomic arrangements observed in the final structures of Au-Ag BNCs we investigated the mechanism of Au and Ag atom mixing at the (pre)nucleation stage both theoretically using DFT and experimentally using RTof-MS. Although gas-phase cluster formation is believed to proceed *via* fast collision of hot vaporized metal atoms from the target with inert gas atoms, very little is known on the details of the nucleation and growth process.¹³⁴ It is generally accepted that the first step of the cluster growth comprises the formation of embryos^{24, 135} consisting of ultra-small nanoclusters of a few atoms¹³⁶ through three-body collisions. Upon embryo stabilization, the cluster may then further grow *via* cluster-cluster collision and/or atomic vapour condensation.¹³⁷

3.6 Cluster formation mechanism

To get more insight into the energy of formation of Au-Ag bimetallic embryos we have evaluated their tendency to form mixed or pure nanoclusters¹³⁸ by calculating the Au-Ag mixing energy in dimer, trimer, and tetramer nanoclusters using spin-unrestricted density functional theory with the PBE functional (see section 3.2).

Figure 3.13-a shows that, in the case of tetramer nanoclusters, the mixing energy of Au₂Ag₂ corresponds to a clear minimum. This value is 0.8 eV lower than for the monometallic nanoclusters and implies that the formation of bimetallic Au₂Ag₂ nanoclusters is energetically most favourable. Although this observation is made here specifically for four-atom nanoclusters, this behaviour also applies to other small cluster nuclearities. It can also be generalized to other types of alloys since strongly negative mixing energy in small nanoclusters have been reported in several bimetallic systems. These calculations concern miscible systems such as for example PdCo¹³⁹ and AuPd,¹⁴⁰ and even systems whose mixing energy is positive in the bulk, but not at the nanoscale, such as AgCu¹⁴¹ and AgNi.¹⁴² A consequence of this behaviour is that the relative abundance of the ultra-small BNCs present at the (pre)nucleation stage will always be higher than that of their monometallic counterparts.

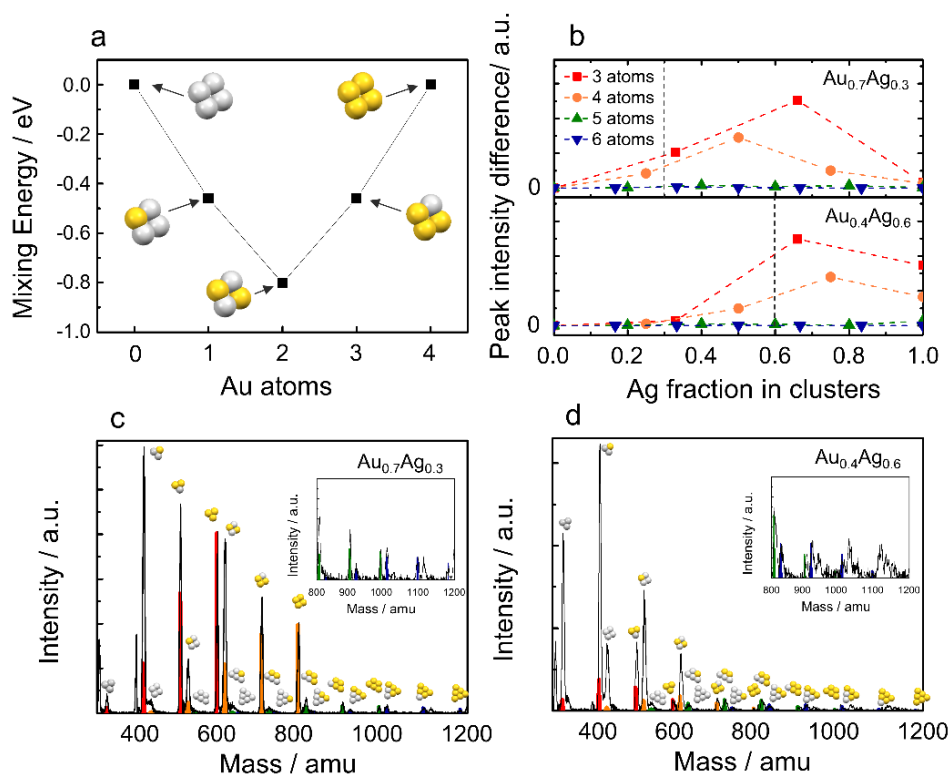


Figure 3.13 (a) DFT calculations of the mixing energy of tetramers: Ag₄, Au₁Ag₃, Au₂Ag₂, Au₃Ag₁, and Au₄. RTof-MS peak intensity difference of the relative abundance of trimers to hexamers, which are calculated from Au_{0.4}Ag_{0.6} and Au_{0.7}Ag_{0.3} RTof-MS. Vertical dash lines represent the global compositions and the 0 in y-axis corresponds to no abundance difference between the experimental and simulated MS (b). The corresponding RTof-MS of Au_{0.7}Ag_{0.3} and Au_{0.4}Ag_{0.6} with binomial combinatorial calculations of trimer (red), tetramers (orange), pentamer (green) and hexamer (blue) are shown in (c) and (d), respectively.

This hypothesis is nicely supported experimentally by the mass spectra collected during the gas-phase formation of Au_{0.7}Ag_{0.3} and Au_{0.4}Ag_{0.6} in the ultra-small cluster size range of less than 1200 u. As the peak intensities are proportional to the nanoclusters abundance, the excess abundance for each specific cluster composition is calculated by comparing the simulated peak intensities from the binomial combination theorem with the measured ones. RTof mass spectra peak intensities of Au₃, Au₄, Au₅, and Au₆ are taken as references, for the 3, 4, 5, and 6 atom nanoclusters, respectively. The excess abundance for the 3, 4, 5, and 6 atom nanoclusters during the nucleation of Au_{0.4}Ag_{0.6} and Au_{0.7}Ag_{0.3} BNCs are calculated by the peak intensity difference and plotted in Figure 3.13-b, and the corresponding mass spectra are shown as Figure 3.13-c and Figure 3.13-d. In the analysed size range from trimer to hexamer nanoclusters formed during the Au_{0.7}Ag_{0.3} and Au_{0.4}Ag_{0.6} productions, the bimetallic trimers and tetramers are present in

significant excess compared to the abundance expected for the binomial combination (Figure 3.13-b). On the other hand, larger nanoclusters nicely match the expected global composition indicating that the mixing energy is only playing a major role in the formation of the smallest nanoclusters. Significant excess of pure Ag₃ and Ag₄ nanoclusters observed in Au_{0.4}Ag_{0.6} likely originates from the slight overstatement of the abundance of pure Ag nanoclusters caused by the lower ionization energy of silver compared to gold.

Computational modelling in combination with experimental mass abundance spectrometry suggests that the Au-Ag mixing energy favouring the formation of ultra-small BNCs, dimers to tetramers, during the gas phase (pre)nucleation stage is responsible for the composition-tunable segregation behaviour of Ag and Au in the Au-Ag BNCs deposited on supports. Energetically favourable ultra-small BNCs are likely to form before their monometallic counterparts from the gas mixture of Au and Ag monomers present in the chamber during laser ablation and this process results in depleting the atoms of the minority element.¹⁴³ These small BNCs may then rapidly agglomerate by cluster-cluster collisions into larger nuclei, keeping a similar average composition. These nuclei could form the core of BNCs that will appear systematically enriched with the minority element, except obviously for Au_{0.5}Ag_{0.5}. Monometallic nanoclusters and /or atoms of the majority element aggregate later *via* cluster-cluster collision and atomic vapor condensation to form an outer shell enriched with the majority element. This process is in line with the formation of a partially segregated core-shell structure including a significant degree of alloying observed in the final structure of the Au-Ag BNCs.

Interestingly, similar processes have been reported for monometallic¹⁴⁴⁻¹⁴⁵ and bimetallic⁹⁴ gold-based NPs growth in solutions. For monometallic NPs, formation of small nanoclusters from the Au monomers after partial reduction of the gold precursor was identified as the first step of the growth process. These nanoclusters then formed seed particles with radii > 1.5nm attracting the remaining gold ions in two steps on top of the seed particles' surfaces until the precursor is fully consumed. In mixed-metal pre-nucleation of multinuclear metal-thiolate complexes, ultra-small tetramer bimetallic Au-Cu nanoclusters were found to play a critical role in obtaining alloyed Au-Cu BNCs in solution, similar to the observations we here make for gas-phase growth in the laser ablation cluster source. Conversely, in two-phase syntheses, where these mixed metal-thiolate pre-nucleation species were absent, the formation of core-shell architectures was observed.¹¹²

DFT modelling supported by mass spectrometry suggests that, as for colloidal synthesis in solution, the chemical structure of the ultra-small nanoclusters (less than 5 atoms) present in the gas-phase during the bimetallic cluster nucleation is likely tuning the final spatial atomic organization of the BNCs deposited onto supports. We propose a

4-step schematic representation of the growth process of Au-Ag nanoclusters in the gas phase of a CBD source based on our combined investigation of the gas-phase nucleation stage and the post deposition BNCs final structures.

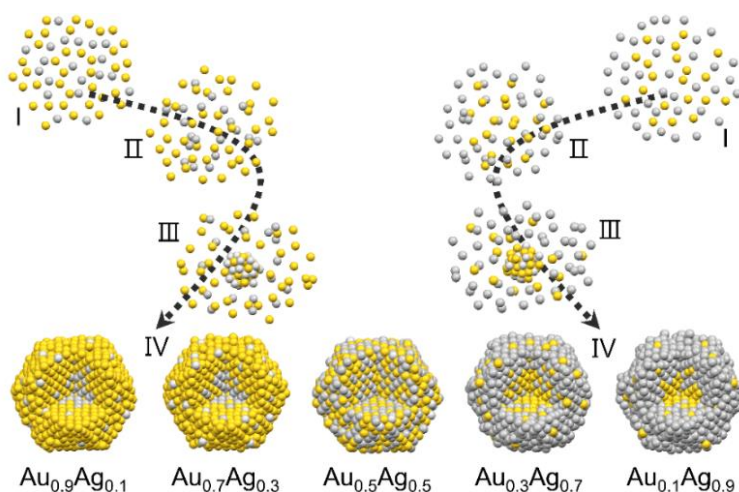


Figure 3.14 Schematic representation of the 4-step growth process of Au-Ag nanoclusters in the gas-phase before deposition: (I) Au and Ag atoms are generated by laser ablation of the targets; (II) ultra-small BNCs form and the minority element is depleted from the metal gas; (III) the small BNCs serve as embryos or building blocks for the further growth of nuclei/seeds and the majority element atoms also condense on the bimetallic core to form the cluster shell; (IV) formation of nanoclusters, with alloy cores enriched by the minority element and shell enriched by the majority element. A full alloy is formed in $Au_{0.5}Ag_{0.5}$.

As depicted in Figure 3.14, in the gas of monomers produced immediately after the laser ablation of two pure metal targets (I), the embryos or building blocks appearing in the monomers nucleation are bimetallic ultra-small nanoclusters (up to 4 atoms) whose excess abundance is detected with mass spectrometry (II). In a third stage, these BNCs aggregate immediately into bimetallic nuclei/seeds that will form the alloyed core of the BNCs enriched in the minority element observed by STEM (III). The remaining part of the nanoclusters or monomers enriched in the majority element that were formed later due to their less favourable mixing energy aggregate onto the preformed nuclei/seeds to form the pure and alloyed majority element outer shell of the BNCs (IV).

The proposed growth process may explain why the final atomic arrangement of Au-Ag BNCs presents a unique composition-tunable core-shell inversion with a systematic location of the minority and majority elements, respectively, in the alloyed core and in the rather pure outer shell of BNCs observed with STEM, XPS and Refl-XAFS. When the fraction of each element is equal, as in $Au_{0.5}Ag_{0.5}$, the (pre)nucleation mixed cluster composition reflects the global composition and remains constant during the whole

growth process and no segregation is observed. This mechanism suggests that the final architecture and the properties of Au-Ag BNCs may be tuned by controlling the composition of the cluster species present in the gas-phase prior to NP nucleation.

We believe that similar processes may also apply to the synthesis of a large variety of bimetallic systems in the gas-phase but also in solution, since the main ingredient for obtaining this kind of behaviour is simply a strongly negative mixing energy for small nanoclusters that also has been reported in other binary systems.^{139-142, 146} This prospect may lead to major advances in the atom-scale control over multimetallic NP atomic arrangements and the surface atoms that are largely responsible for their catalytic and optical performance.

3.7 Conclusions

To uncover the role composition plays on the final particle architecture, Au-Ag BNCs of relatively uniform sizes, *ca.* 3 nm in diameter, and very precise compositions spanning the Au-Ag miscibility range were prepared by a new approach based on the CBD technology equipped with mass spectrometry enabling in-flight tuning of the cluster stoichiometry prior to deposition. Their combined structural characterization carried out by HAADF-STEM, XPS and Refl-XAFS, showed that both Au rich and Ag rich Au-Ag BNCs compositions are segregated with the minority element systematically predominant in the alloyed core of the BNP; the majority element is located in the outer shell with a significant fraction of pure phase. This composition-tunable core-shell arrangement is explained by the lower mixing energy of bimetallic ultra-small nanoclusters that favours their formation over their pure counterparts in the early stage of the gas phase nucleation process. As favourable mixing energy of bimetallic ultra-small nanoclusters is common to many bimetallic systems the proposed 4-step growth mechanism leading to composition-tunable chemical ordering inversion is likely applicable to other BNCs besides AuAg.

In summary, we showed that the overall compositions of the gas phase synthesized BNCs directly control their atomic arrangements. Precise control of the compositions of the nucleation species during the synthesis of BNCs may contribute further to designing novel BNCs with tailored atomic arrangements and their high performance properties for a wide range of applications.

Chapter 4

CO oxidation on oxide supported $\text{Au}_x\text{Ag}_{1-x}$ bimetallic nanoclusters

Bimetallic nanoclusters (BNCs) exhibit various structures, electronic, optical and chemical properties distinct from their monometallic counterparts.¹⁴ Controlling the composition of BNCs opens up an opportunity to investigate their physical and chemical properties more fundamentally. An in depth understanding of BNCs properties is important to improve the current catalyst systems. In this chapter, preliminary CO oxidation catalytic activity studies of phase segregated and fully alloyed $\text{Au}_x\text{Ag}_{1-x}$ BNCs supported on various supports are reported.

4.1 Introduction

Au-Ag BNCs have been widely investigated in the last decade. One of their most remarkable properties is the synergistic effect of the two elements on the CO oxidation reaction,^{41, 105} in which the structure of the Au-Ag bimetallic cluster plays an important role.¹⁵ Due to the identical lattice constants of Au and Ag,¹¹³ a lot of possible structures of Au-Ag bimetallic nanoclusters have been reported, such as core-shell, Janus and intermixing structures.^{79, 147-148} We have demonstrated in Chapter 3 that in Au-Ag BNCs produced by dual-target-dual-laser ablation method that the formation mechanism is governed by the preferential formation of binary few-atom nanoclusters. Composition dependent phase segregated core-shell structures were observed: in gold rich nanoclusters the core is silver enriched and the outer shell is composed of a gold rich alloy, while for silver rich nanoclusters the opposite is found. On the other hand, in this investigation, Au-Ag BNCs produced by MACS were shown by STEM to possess alloy structures for all the compositions.

The catalytic activity of these two types of $\text{Au}_x\text{Ag}_{1-x}$ BNCs produced respectively by a laser ablation cluster source (KU Leuven) and by MACS (University of Birmingham) and deposited on SiO_2 , TiO_2 and MgO from Au rich to Ag rich compositions were investigated under realistic CO oxidation conditions in an industrial relevant reactor. Although the amount of core-shell $\text{Au}_x\text{Ag}_{1-x}$ BNCs supported on SiO_2 wafer is in the nano-gram range, a clear CO_2 production is detected for all the investigated compositions. Furthermore, it is shown that after the first reaction cycle, the reaction onset temperature of Au-rich BNCs decreased from 280 °C to 210 °C while the catalytic activity was enhanced in the second reaction cycle compared to the silver rich case. The support effect was also investigated in $\text{Au}_{0.5}\text{Ag}_{0.5}$ BNCs supported on SiO_2 wafers and TiO_2 powders. It was found that the catalytic activity of the BNCs was highly enhanced when they were

supported on TiO₂ anatase powders. However, since a limited amount of nanoclusters were supported on the SiO₂ thin film, most of the CO molecules did not interact with the BNCs and therefore the consumption of CO could not be quantified. Therefore, MACS was used to scale-up the amount of BNCs deposited on MgO powder surface to increase the contact time between the CO molecules and the BNCs. 2 micro-gram of copper contaminated fully alloyed Au-Ag BNCs were produced and deposited with 0.001 wt% from gold rich to silver rich compositions. Both CO₂ production and CO consumption were observed, while the silver rich BNCs presented the highest catalytic activity in both reaction cycles, with an onset temperature decreasing from 230 °C to 200 °C in the first and second cycle respectively.

4.2 Phase segregated Au_xAg_{1-x} nanoclusters deposited on SiO₂ wafers and TiO₂ powders produced by laser ablation cluster source

A series of phase segregated Au_xAg_{1-x} BNCs from Au rich to Ag rich, produced by laser ablation cluster source from one alloy target or two pure targets, were deposited on SiO₂ wafers and TiO₂ anatase powders. The detailed synthesis methods and characterization of the composition dependent phase segregated BNC structures with various techniques are described in Chapter 3. Four circular areas of 1 cm diameter were deposited with 1 ML coverage with Au_xAg_{1-x} BNCs on 2 cm × 2 cm SiO₂ wafers. The deposited wafers were then cut into small pieces and inserted into a quartz tube flow reactor to test their catalytic activity under CO oxidation conditions. The CO oxidation catalytic activity of Au_xAg_{1-x} BNCs supported on SiO₂ was characterized by loading the entire SiO₂ wafer into the quartz. Both ends of the reactor were then closed by quartz wool. The reactor was purged with 25 ml/min He flow at room temperature for 15 mins to remove the air remaining in the reactor and the gas lines. A gas mixture with 1% CO, 20% O₂ and 79% He was then introduced in the reactor at room temperature and the reactor was purged for 30 mins to stabilize the gas flow and composition. The composition of the exhaust gas was analysed by introducing a small fraction of the gas into a QMS mass analyser. The reactor heating was provided by a temperature controlled furnace operating from room temperature to 300 °C with a 3 °C/min ramping rate. The production of CO₂ in the first and second reaction cycles with Au rich to Ag rich BNCs is shown in Figure 4.1-a and the inset of Figure 4.1-a, respectively.

The BNCs were active towards CO oxidation for all the investigated compositions. In the first cycle of reaction, the onset temperature of catalytic activity for all the Au-Ag BNCs was around 280 °C. As the temperature reached 300 °C, the sample with Au_{0.9}Ag_{0.1} BNCs was the most active, while the catalytic activity of Au_{0.4}Ag_{0.6} and Au_{0.5}Ag_{0.5} BNCs were similar in the investigated temperature range. After the first reaction cycle, the gas

flow in the reactor was replaced by a He flow at 300 °C that was maintained until the reactor was cooled down to room temperature. Then, the gas mixture with 1% CO, 20% O₂ and 79% He was introduced in the reactor for the second reaction cycle. It was found that the catalytic activity of Au_{0.9}Ag_{0.1} BNCs was further enhanced after the first reaction cycle with an onset temperature reduced to 210 °C. On the other hand, the catalytic activity of Au_{0.4}Ag_{0.6} BNCs was slightly reduced, while keeping a similar onset temperature. The catalytic activity variation upon reaction cycling can be attributed to a change in the atomic rearrangement occurring during the CO oxidation reaction.

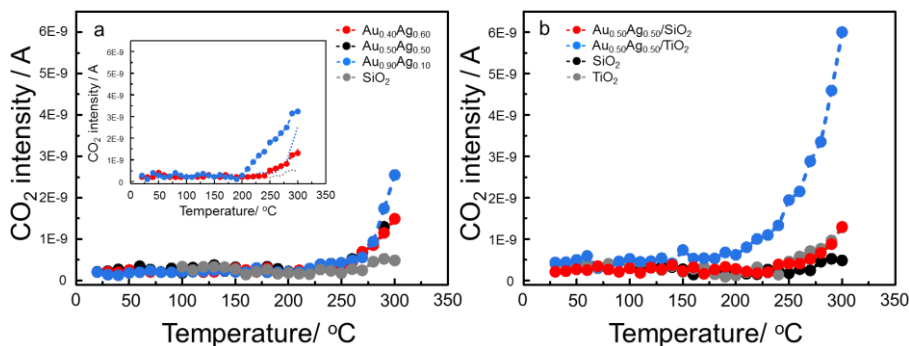


Figure 4.1 CO₂ production of 4 deposition areas of 1 ML Au_xAg_{1-x} ($x = 0.4, 0.5, 0.9$) BNCs supported by 2 cm × 2 cm SiO₂ wafer in the first of reaction cycle of CO oxidation (a), second reaction cycle in the inset of panel (a) with the first reaction cycle results shown in small dots for comparison. Catalytic activity of powder supported Au_{0.5}Ag_{0.5} BNCs on SiO₂ wafer and TiO₂ (b).

In order to investigate the effect of the support, Au_{0.5}Ag_{0.5} BNCs were deposited on thin layers of TiO₂ anatase powder supported on SiO₂ wafers with the same coverage and deposition area to maintain a similar amount of nanoclusters in the gas flow reactor. Thin films of TiO₂ anatase powder were deposited on the Si wafers by first suspending the powders into methanol and placing the 2 cm × 2 cm SiO₂ wafers into the suspension for one day. The wafer supported TiO₂ powder were then dried overnight in vacuum with a pressure around 5×10^{-8} mbar. The weight of TiO₂ anatase powder covering the wafer was around 6 mg. Au_{0.5}Ag_{0.5} BNCs were then deposited on the TiO₂ film in the laser ablation cluster source.

The cluster deposited TiO₂ powders were then scratched from the SiO₂ wafer surface and the obtained powder was placed at the bottom part of the quartz tube reactor to reach a gas flow similar to that used for the catalytic test of BNCs supported on SiO₂ wafers. The catalytic activity of Au_{0.5}Ag_{0.5} BNCs supported on SiO₂ and TiO₂ as well as their reference samples is presented in Figure 4.1b. 6 mg of TiO₂ powders reference sample was shown to be as active as the sample of Au_{0.5}Ag_{0.5} BNCs supported on SiO₂ wafer surface. However, the catalytic activity of Au_{0.5}Ag_{0.5} BNCs supported on TiO₂ powder

presented a five-fold increase compared to the same $\text{Au}_{0.5}\text{Ag}_{0.5}$ BNCs supported on SiO_2 wafer.

Although the production of CO_2 was clearly observed for all these four Au-Ag samples, the consumption of CO could not be quantified with the mass analyser. This is likely due to the very limited amount of catalyst present in the reactor that strongly restricts the portion of the gas flow interacting with the supported catalysts.

4.3 Fully alloyed $\text{Au}_x\text{Ag}_{1-x}$ nanoclusters deposited on MgO powders produced by matrix assembly cluster source

In order to scale up the density of nanoclusters in the catalytic reactor, a series of $\text{Au}_x\text{Ag}_{1-x}$ BNCs were deposited on MgO powders using the matrix assembly cluster source (MACS) and their activity tested under CO oxidation. The detailed description of the MACS system can be found in section 2.1.3. A series of Au-Ag bimetallic nanoclusters were deposited on thin layers of MgO powder, supported on glass slides. $\text{Au}_{0.75}\text{Ag}_{0.25}$, $\text{Au}_{0.5}\text{Ag}_{0.5}$ and $\text{Au}_{0.25}\text{Ag}_{0.75}$ BNCs were produced by controlling the evaporation rate of each element in the two thermal evaporators. The pressure of Ar was kept at 6×10^{-6} Torr and the metal atom-Ar matrix was condensed on the copper matrix support cooled down to 25 K. After 80 minutes of matrix formation, the matrix was subsequently sputtered with an Ar^+ beam for 5 minutes and the nanoclusters were deposited on 21 glass slides covered by a thin MgO powder layer, positioned on a rotating carousel.

The size distributions and the structures of the $\text{Au}_x\text{Ag}_{1-x}$ BNCs were revealed by imaging direct cluster deposition samples. The cluster-support interaction in $\text{Au}_x\text{Ag}_{1-x}/\text{MgO}$ supported on TEM grid was investigated by STEM and examples of the images are presented in Figure 4.2. The size distribution of $\text{Au}_x\text{Ag}_{1-x}$ BNCs from gold rich to silver rich compositions were evaluated by analysing more than 1000 nanoclusters. Without mass selection, a relatively narrow size distribution was still obtained with an average cluster size of around 1.1 nm in diameter for all the compositions, highlighting the specific process of cluster production in MACS.⁵⁵ Analysis of the HAADF-STEM intensity of the gold rich to silver rich BNCs compositions showed that each BNC possessed a uniform composition distribution from the center to the edge of the cluster, with no apparent phase segregation. The cluster coverage in these three samples was kept at 0.08 nanoclusters/ nm^2 . STEM images of $\text{Au}_x\text{Ag}_{1-x}$ BNCs supported on MgO powder, presented in the insets of Figure 4.2-a, b and c, showed no marked shape, size and structure difference with the BNCs on carbon TEM grids. This indicates that the

interaction between BNCs and the MgO support has no major influence on the cluster structure that is similar whether the nanoclusters are supported on carbon or on MgO.

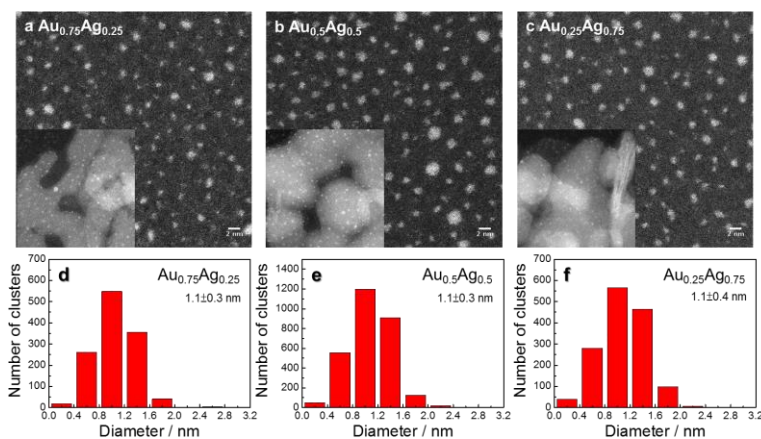


Figure 4.2 STEM images of the $\text{Au}_{0.75}\text{Ag}_{0.25}$, $\text{Au}_{0.5}\text{Ag}_{0.5}$ and $\text{Au}_{0.25}\text{Ag}_{0.75}$ nanoclusters on MgO powders.

In order to assess the precision of the composition control in the MACS system, RBS measurements were carried out on these samples and the results are presented in Figure 4.3. Although the gold-silver ratio in each of these three samples reflects well the expected values from gold rich to silver rich, Cu was surprisingly the dominant contribution at the powder surface. The compositions obtained from RBS measurements are summarized in the inset of Figure 4.3. The presence of Cu can be attributed to the Ar^+ sputtering of the copper matrix support after the pre-formed metal-Ar matrix was consumed. In future experiments this will be prevented by precisely controlling the sputtering time of the metal-Ar matrix to avoid sputtering of the support.

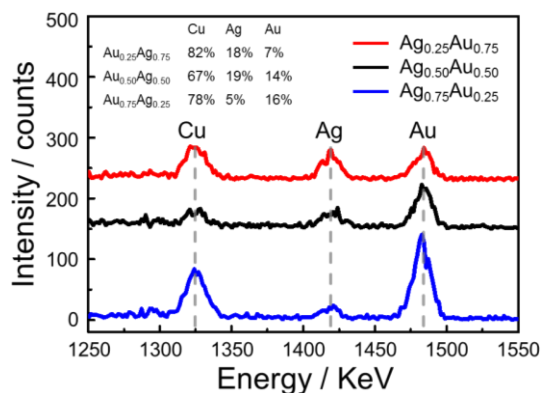


Figure 4.3 RBS spectra of deposited $\text{Au}_x\text{Ag}_{1-x}$ BNCs from gold rich to silver rich on MgO powders.

Although a significant amount of copper was present at the sample surface, Cu is believed not to alloy with $\text{Au}_x\text{Ag}_{1-x}$ BNCs because the Cu atoms were sputtered out from the matrix support after the Au-Ag-Ar matrix was consumed. Therefore, Cu nanoclusters are more likely present as monometallic nanoclusters only located at the top most layer of the sample surface suggesting that the interaction and the formation of a mixed phase between Cu and $\text{Au}_x\text{Ag}_{1-x}$ BNCs may be neglected.

The CO oxidation catalytic activity of MgO supported $\text{Au}_x\text{Ag}_{1-x}$ BNCs was characterized by loading 50 mg of catalyst into the quartz reactor at a position fixed by quartz wool closing both ends of the reactor. The reactor was purged with 25 ml/min He flow at room temperature for 15 mins to evacuate the air in the reactor and in the gas lines. Similar reaction conditions as those used in the tests reported in the section 4.2 were then applied with a gas mixture of 1% CO, 20% O_2 and 79% He and a temperature ramping rate of 3 °C/min. The production of CO_2 and the consumption of CO in the first and second reaction cycles are shown in Figure 4.4.

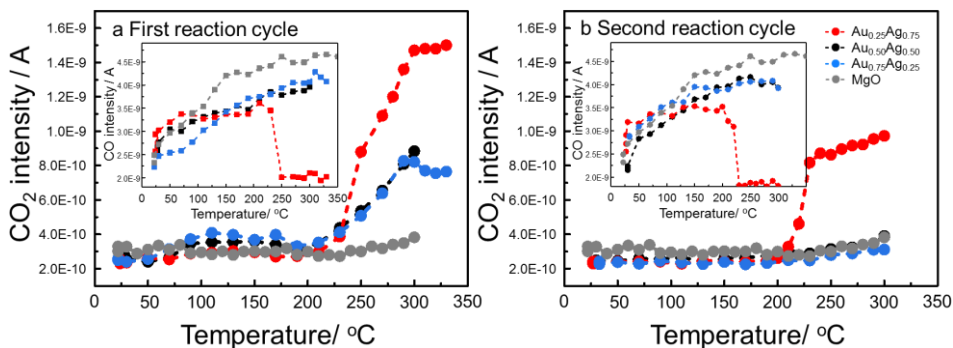


Figure 4.4 Production of CO_2 and the consumption of CO in the first (a) and second (b) reaction cycles with MgO supported $\text{Au}_x\text{Ag}_{1-x}$ BNCs.

Pristine MgO powder showed a limited catalytic activity under CO oxidation in the investigated temperature range. CO_2 was only formed at temperatures above 200 °C for all the Au-Ag compositions. In the three investigated compositions, the gold rich and equal amount samples showed a similar catalytic activity. However, silver rich $\text{Au}_{0.25}\text{Ag}_{0.75}/\text{MgO}$ presented a catalytic activity that was twice that of the other two samples containing a higher Au fraction. Only $\text{Au}_{0.25}\text{Ag}_{0.75}/\text{MgO}$ sample consumed all the CO molecules and converted them to CO_2 at temperatures above 250 °C. After the first reaction cycle, the gas flow in the reactor was replaced by a He flow at 300 °C that was maintained until the reactor was cooled down to room temperature. A gas mixture of 1% CO, 20% O_2 and 79% He was introduced into the reactor again for the second reaction cycle experiments. In the second cycle, only the silver rich sample showed a catalytic

activity identical to that observed in the first cycle. In contrast, the gold rich and equal amount samples show no catalytic activity in the studied temperature range.

4.4 Conclusions

The catalytic CO oxidation activity of phase segregated and fully alloyed $\text{Au}_x\text{Ag}_{1-x}$ BNCs produced by laser ablation cluster source and MACS supported on various supports were tested in industrial relevant quartz tube gas flow reactors. It was found that all the $\text{Au}_x\text{Ag}_{1-x}$ BNCs are catalytically active with an activity strongly depending on the BNCs compositions and supports. Among the phase segregated BNCs, $\text{Au}_{0.9}\text{Ag}_{0.1}$ BNCs are the most active and after the first CO oxidation reaction cycle, their catalytic activity is even enhanced with an onset temperature reduced to 210 °C. This might be assigned to a re-organization of the spatial arrangement of Au and Ag atoms within the BNCs during the first reaction cycle: Ag atoms segregating to the BNC surface and forming an alloy with the surface Au atoms. Further studies, such as in situ EXAFS or environmental TEM, are required to fundamentally understand the dynamics of the atomic structure re-arrangement under catalytic reactions and the mechanism at the origin of this phenomenon. The support of the BNCs can also strongly influence their catalytic activity as shown by $\text{Au}_{0.5}\text{Ag}_{0.5}$ BNCs whose catalytic activity was substantially enhanced by using a TiO_2 anatase support instead of SiO_2 .

It has been demonstrated that the MACS can produce a sufficient amount of BNC catalyst for industrial relevant catalysis investigations. The 2 micro-gram of MgO powder supported copper contaminated $\text{Au}_{0.25}\text{Ag}_{0.75}$ sample was shown to have the ability to reach 100 % conversion at 250 °C. However, further studies regarding the proper control of the sputtering time are required to prevent copper atoms to be sputtered out from the matrix support. In order to design a better catalyst, the inert MgO support can be replaced by more active oxide supports such as TiO_2 or CeO_2 .

Chapter 5

Methanol decomposition on CO poisoning reduced $\text{Pt}_x\text{Ni}_{1-x}$ nanoparticles supported by SiO_2

The results presented in this chapter are based on:

Reducing of CO poisoning of Pt nano-catalyst by alloying with Ni

Ting-Wei Liao,^a Anupam Yadav,^a Piero Ferrari,^a Yubaio Niu,^b Jerome Vernieres,^b Xian-Kui Wei,^c Marc Heggen,^c Rafal Dunin-Borkowski,^c Kuo-Juei Hu,^a Didier Grandjean,^a Richard E. Palmer^b, Kari Laasonen,^d Ewald Janssens,^a and Peter Lievens^a

To be published

^a Laboratory of Solid-State Physics and Magnetism, KU Leuven, Belgium.

^b College of Engineering, Swansea University, United Kingdom.

^c Ernst Ruska-Centre for Microscopy and Spectroscopy with Electrons and Peter Grünberg Institute, Forschungszentrum Jülich GmbH, Germany.

^d Department of Chemistry and Materials Science, Aalto University, Finland.

P. L., D. G., E. J. and T.-W. L. designed the project. T.-W. L. and A. Y. synthesized and deposited bimetallic nanoclusters. Y. N., X.-K. W., M. H., R. D.-B. and R. P. carried out the STEM measurements. J. V. carried out the XPS measurements and T.-W. L. analysed the results. K. L. and P. F. performed the DFT calculations. T.-W.L wrote the first draft of the manuscript and all authors contributed to writing and proofreading.

Abstract Direct methanol fuel cells are a promising renewable energy source that uses methanol as an excellent on-board hydrogen source in a liquid form. Currently, platinum is the most commonly used material as anode catalyst owing to its high activity. However, Pt is prone to CO poisoning, which limits the lifetime of the catalyst. Here, we show how alloying Pt nanoclusters with Ni can substantially reduce the CO poisoning effect at room temperature, without affecting the methanol dehydrogenation activity. Pt_xNi_{1-x} bimetallic nanoclusters of different compositions were investigated using high-angle annular dark-field scanning transmission electron microscopy (HAADF-STEM), temperature programmed desorption (TPD) and X-ray photoelectron spectroscopy (XPS), to examine their composition dependent atomic arrangements, methanol dehydrogenation catalytic activity, and electronic structure. We then combined the experimental results with density functional theory (DFT) calculations to demonstrate that local d-band modifications induced by subsurface Ni atoms weaken the interaction of platinum with CO. These findings provide a new route towards enhancing the lifetime of Pt-based anode catalysts.

5.1 Introduction

Electrochemical devices such as low temperature proton exchange membrane fuel cells (PEMFC) and high temperature solid oxide fuel cells (SOFC) are emerging as efficient, low cost and ecologically-friendly solutions to harvest energy from diverse renewable and clean sources, such as hydrogen, hydrocarbons, water, bio-alcohols and bio-fatty acids. Moreover, bio-alcohol (methanol, ethanol, etc.) based fuel cells, such as the direct methanol fuel cell (DMFC), are more reliable than gas fed (H₂ or HCs) fuel cells, as they generate H₂ directly from a liquid fuel that is easier to store and transport.¹⁴⁹⁻¹⁵⁰ The catalytic dehydrogenation of methanol (CH₃OH) is an important anode reaction of DMFCs, which decomposes methanol into hydrogen and generates energy.¹⁵¹⁻¹⁵² Although platinum is a widely used material as an anode reaction catalyst due to its high activity, the performance of fuel cells is limited by its activity, stability, and selectivity.¹⁵³⁻¹⁵⁵ The three main drawbacks of platinum catalysts-based anodes are their high cost, their low selectivity to generate hydrogen as end product and their low stability in the presence of carbon monoxide, i.e. the CO poisoning effect.¹⁵⁶⁻¹⁵⁷ These crucial issues require remediation in order to design future high performance fuel cell catalysts, for which a fundamental understanding of the reaction kinetics at the atomic and molecular level is required. For this purpose, model catalyst systems such as single Pt atoms,¹⁵⁸ Pt single crystals,¹⁵⁹⁻¹⁶¹ oxide supported Pt thin films¹⁶² and Pt nanoparticles¹⁵⁴⁻¹⁵⁵ have been investigated intensively under ultra-high vacuum conditions to reveal the reaction kinetics.

Recent studies have shown that fuel cells using Pt-alloy nanoparticles as catalysts featured a better performance than those using pure Pt. This was attributed to the enhanced tolerance to CO poisoning of Pt-alloy nanoparticles, compared to their mono metallic counterparts. Among other alloying materials, Sn, Ru, Mo, Nb, W, Ag, and Ni have been

investigated.¹⁶³⁻¹⁶⁶ However, the underlying mechanism for the alloy-induced tolerance to the CO poisoning effect is still under debate. Co-adsorption of CO and OH groups,¹⁵⁶ and/or the alteration of the electronic structure of platinum, induced by alloying may be responsible for this effect.¹⁶⁷⁻¹⁶⁹ Although density functional theory calculations (DFT)^{160, 170-172} and experiments on few-atom nanoclusters in the gas phase¹⁷³⁻¹⁷⁴ support the latter interpretation, fundamental aspects such as the direction of the electron transfer between Pt and Ni atoms in small nanoclusters and nanoparticles is controversial.¹⁷⁵⁻¹⁷⁶

Nanoclusters are typically composed of less than a thousand atoms and have dimensions smaller than a few nanometres. They have unique optical,⁸¹ catalytic,^{34, 82, 103, 177} and magnetic⁸³ properties, distinct from those of the bulk phase, which make them promising candidates for numerous applications in fields such as energy harvesting and magnetic storage. Designing new fuel-cell catalysts by depositing preformed metal nanoclusters, with well-defined size and composition, on oxide supports, could be one of the key solutions to obtain better catalysts.¹⁷⁸ Cluster Beam Deposition (CBD) technology is the most suitable technique to deposit preformed bimetallic nanoclusters/nanoparticles onto supports. It allows the deposition of precisely controlled nanoparticles in size and composition with various levels of cluster-support interactions and controlled coverages.^{17, 22, 59, 103} The properties of deposited nanoclusters could be further enhanced by a synergistic combination of different metals to ultimately enhance the dehydrogenation reactivity, and at the same time reduce both CO poisoning and the amount of platinum used.

In this study, we used CBD with a laser ablation cluster source¹⁷⁹ to produce and deposit $\text{Pt}_x\text{Ni}_{1-x}$ bimetallic nanoclusters (BNCs) with an accurate control of their chemical composition. The nanoclusters were deposited on two different supports, carbon TEM grids and native SiO_2 surfaces, with different coverages ranging from 1 to 5 atomic monolayers (ML). Using a combination of STEM, TPD and XPS, their atomic arrangement, catalytic activities toward methanol decomposition and CO poisoning as well as their oxidation states and electronic structures were revealed. Based on the STEM and TPD results, the most interesting nanoclusters with diameter around 2.5 nm and 75% of Pt fraction, $\text{Pt}_{417}\text{Ni}_{144}$ and $\text{Pt}_{353}\text{Ni}_{106}$, were selected and modelled. Various chemical arrangements (alloy-core-Pt-enriched-shell, Ni-core-Pt-shell and full alloy) were considered. With local structure optimization, it was found that the alloy core with Pt enriched shell is the lowest energy structure. DFT calculations carried out on $\text{Pt}_{353}\text{Ni}_{106}$ and $\text{Pt}_{417}\text{Ni}_{144}$ nanoclusters demonstrate that the reduced CO poisoning by alloying Pt with Ni can be attributed to local Pt d-band modifications, induced by subsurface Ni atoms.

5.2 Experimental details

Production of $\text{Pt}_x\text{Ni}_{1-x}$ nanoclusters. Composition controlled $\text{Pt}_x\text{Ni}_{1-x}$ ($x = 0, 0.1, 0.3, 0.5, 0.7, 0.9, 1$) BNCs were produced by a combination of pulsed laser (10 Hz, Nd:YAG lasers, Spectra Physics, INDI) ablation of $\text{Pt}_x\text{Ni}_{1-x}$ (ACI alloy, purity 99.5%) plate targets and inert gas (He, purity 99.9999%) condensation. The size distribution of the BNCs monitored by reflectron time-of-flight (RTof) mass spectrometry and their average size optimized around $2.0 \text{ nm} \pm 0.7 \text{ nm}$. The cluster source was cooled by liquid nitrogen, resulting in a production temperature of about 100 K. Following a supersonic expansion into vacuum of the helium carried molecular beam, the cationic $\text{Pt}_x\text{Ni}_{1-x}$ BNCs were guided to the deposition chamber and soft-landed ($\sim 500 \text{ m/s}$) on TEM grids and $\text{SiO}_2/\text{Si}(100)$ substrates for STEM and TPD measurements, respectively.¹¹⁹ The substrates were held at room temperature and equivalent atomic coverages of 1 ML for TEM and 5ML for TPD were respectively deposited. The flux of the BNCs was monitored by a quartz crystal microbalance and the BNC coverage was controlled by the deposition time assuming a constant cluster flux.

Atomic structures of $\text{Pt}_x\text{Ni}_{1-x}$ nanoclusters. Atomic resolution STEM imaging was performed by FEI Titan G2 80-200 CREWLEY operating at 200 keV and equipped with spherical aberration (Cs) probe corrector and high-angle annular dark-field (HAADF) detector. The cluster size distributions of the $\text{Pt}_x\text{Ni}_{1-x}$ BNCs were obtained by measuring at low magnification more than 300 BNCs. The cluster size was determined by measuring the diameter cross-section of individual nanoclusters. Identification of a possible core-shell structure was obtained by the Z-contrast of HAADF-STEM (Z is the elemental atomic number). The HAADF-STEM intensity is proportional to $Z^{1.5}$ with the camera length employed.¹²⁰ The large difference of atomic number between Pt and Ni ($Z_{\text{Pt}} = 78$; $Z_{\text{Ni}} = 28$) allowed us to distinguish the elemental atomic arrangement within the nanoclusters directly from the HAADF-STEM image intensity contrast. STEM image analysis was carried out with the imageJ Fiji software.¹²¹ The intensity profile of each cluster was obtained by first identifying the position of the centre through averaging, and then binning the intensity in polar coordinates as a function of the radial distance to the centre.

Methanol decomposition on $\text{Pt}_x\text{Ni}_{1-x}/\text{SiO}_2/\text{Si}$ (100). Boron doped amorphous $\text{SiO}_2/\text{Si}(100)$ wafers were heated up with direct resistive heating and cleaned more than three times by a flash-heating process to 700 K to desorb all contaminations in an UHV chamber (base pressure 6×10^{-10} mbar) dedicated to the TPD experiments. The desorbed contaminations were monitored by a quadruple mass spectrometer (QMS), considering the masses of H_2O (18), CO/N_2 (28), O_2 (32), Ar (40), CO_2 (44). The sample cleaning process was terminated at the point the signal of the listed masses was reduced to the noise level. Methanol-d4 (CD_3OD) was purified in an UHV compatible glass test tube by

repeated freeze–pump–thaw cycles to remove all the gases in the test tube and the vacuum gas lines. It was then introduced into the UHV chamber by a leak valve and guided to the sample surface by a dozer tube. The cleaned sample was exposed to methanol-d4 at 100 K until and adsorption of 5 Langmuir units ($1 \text{ L} = 1 \times 10^{-6} \text{ torr second}$) on the SiO_2 surface was obtained. Methanol-d4 desorption was conducted using PID controlled linear heating with 4 K/s ramping rate and the molecule desorption was monitored by the QMS considering all possible cracking patterns of methanol-d4. It was found that SiO_2 surface is inert towards methanol decomposition, by comparing the desorption feature of the methanol-d4 cracking pattern. No C-H, C-O or OH bond scission was observed.

The cleaned SiO_2/Si (100) samples were then transferred in a home-built UHV transport vessel with base pressure in the 10^{-10} mbar range to the CBD chamber with base pressure in the 10^{-9} mbar range. After deposition of $\text{Pt}_x\text{Ni}_{1-x}$ BNCs on the SiO_2/Si (100) substrates, the samples were transferred back to the TPD setup for methanol decomposition experiments. The samples were cooled down to 100 K by a flow of liquid nitrogen (LN_2) in flexible stainless steel tubes and exposed to 5 L methanol-d4 for a saturated adsorption of methanol-d4 on the surface. TPD spectra were taken in the 100 K to 500 K temperature range with a 4 K/s ramping rate. The catalytic experiments were repeated 3 times for each sample to characterize the catalytic activity and stability.

Electronic structure and oxidation state characterizations. XPS experiments were performed at room temperature after exposure to air and under UHV condition (Kratos Axis Supra system, base pressure of 1.6×10^{-9} mbar) by using a monochromatized Al $K\alpha$ X-ray source (1486.6 eV) operated at 10 mA. The spectra were collected by a hemispherical analyser with passing energy of 160 eV and 20 eV for the wide scan and high-resolution spectra, respectively. The spectra were aligned to the adventitious carbon peak C 1s placed at 284.8 eV. The deconvolution and fitting of the peaks was done with the Unifit software.¹⁸⁰ The following spin-orbit coupling constrains were considered: peaks separation 17.3 eV and 3.35eV as well as the peak area ratios of 2/3 and 3/4 for Pt 4d and Pt 4f, respectively.

DFT calculations on the electronic structures and CO-Pt interactions. Pt_{459} , Pt_{561} , $\text{Pt}_{417}\text{Ni}_{144}$ and $\text{Pt}_{353}\text{Ni}_{106}$ nanoclusters were modelled with the CP2K code.¹⁸¹⁻¹⁸³ $\text{Pt}_{417}\text{Ni}_{144}$ and $\text{Pt}_{353}\text{Ni}_{106}$, nanoclusters were selected to represent the produced $\text{Pt}_{0.7}\text{Ni}_{0.3}$ nanoclusters with observed size. The BLYP functional with GTH pseudopotentials¹⁸⁴ with 18 active electrons and the DZVP-MOLOPT-SR basis were used for both Ni and Pt. All nanoclusters were placed in a sufficiently large periodic box. For the 459 and 561 atom nanoclusters, cube with edge sizes of 29 Å side and 27 Å were used. The local atomic structure and the total spin were optimized. Due to the metallic nanoclusters the diagonalization method with the Kerker mixing was used in the electronic structure

optimization. The charge analysis was done with the Hirshfeld,¹⁸⁵ Bader, Löwdin and Mulliken methods.

5.3 Morphology of $\text{Pt}_x\text{Ni}_{1-x}$ nanoclusters

The size distribution of $\text{Pt}_x\text{Ni}_{1-x}$ BNCs with $x = 0.9, 0.7, 0.5, 0.3$ and 0.1 was characterized by scanning transmission electron microscopy (STEM). The distribution of average diameters for each composition was measured on a sample of more than 300 BNCs for each $\text{Pt}_x\text{Ni}_{1-x}$ composition. A comparable size distribution was found for the different compositions, with average diameters around 2.0 nm and FWHMs of the size distributions of 0.7 nm (Figure 5.1). In order to characterize the atomic arrangement of the two elements within the $\text{Pt}_x\text{Ni}_{1-x}$ BNCs, STEM images with high resolution were taken for all compositions. Given the large atomic number difference between Pt (78) and Ni (28), the atomic arrangement of these two elements within the BNCs can be revealed by their HAADF intensity line profile.¹²⁰ If phase segregation happens inside the BNCs, the brighter and darker parts of the BNC can be assigned to Pt-rich and Ni-rich areas, respectively. Figure 5.2 presents selected STEM images of $\text{Pt}_x\text{Ni}_{1-x}$ BNCs along with their normalised quantitative radial intensity profile integrated over the polar coordinate. Detailed inspection of the STEM images shows that for all compositions, except $\text{Pt}_{0.5}\text{Ni}_{0.5}$ BNCs, atomic arrangements are phase segregated, while for the case of $\text{Pt}_{0.5}\text{Ni}_{0.5}$, a uniform intermediate intensity prevails over the whole cluster. This indicates that a composition-dependent level of mixing with different atomic arrangements exist in the deposited nanoclusters.

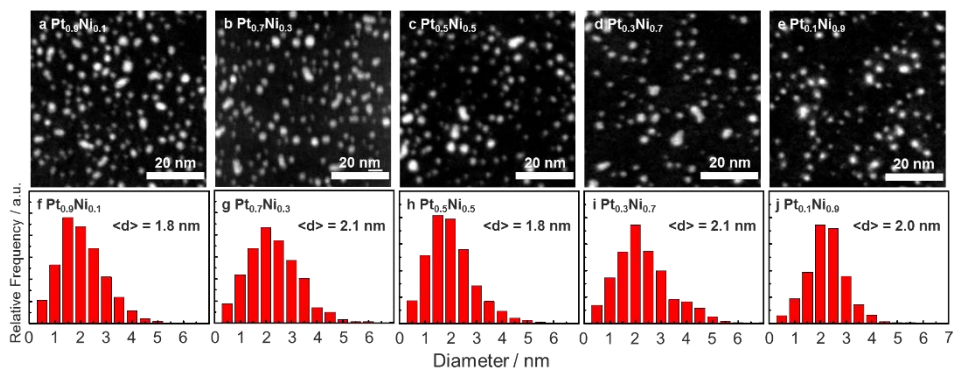


Figure 5.1 STEM images and histograms of diameter distributions of $\text{Pt}_x\text{Ni}_{1-x}$ BNCs: (a, f) $\text{Pt}_{0.9}\text{Ni}_{0.1}$; (b, g) $\text{Pt}_{0.7}\text{Ni}_{0.3}$; (c, h) $\text{Pt}_{0.5}\text{Ni}_{0.5}$; (d, i) $\text{Pt}_{0.3}\text{Ag}_{0.7}$; (e, j) $\text{Pt}_{0.1}\text{Ag}_{0.9}$.

The composition-tunable phase segregated atomic arrangement, with cores enriched in the minority element and shells enriched in the majority element, suggests that the cluster formation mechanism is governed by the preferential formation of binary few-

atom nanoclusters in the nucleation stage. DFT modelling showed that the mixing energy of all the binary tetramer cases (Pt_3Ni_1 , Pt_2Ni_2 and Pt_1Ni_3) is lower than their monometallic counterparts (Pt_4 and Ni_4), indicating that the formation of binary tetramers is energetically favourable (Figure 5.3). The formation mechanism of similar phase segregated structures in $\text{Au}_x\text{Ag}_{1-x}$ BNCs, produced with the same source, were discussed in Chapter 3.²²

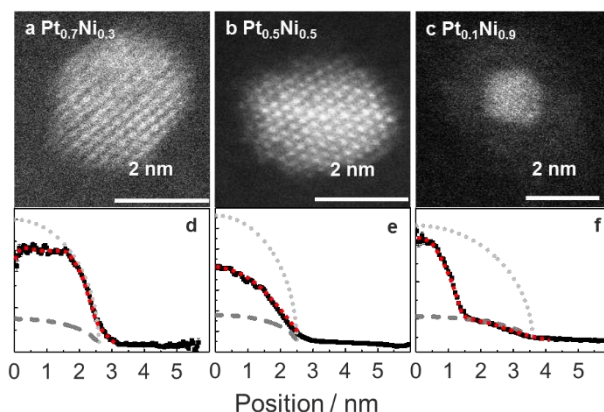


Figure 5.2 Examples of HAADF-STEM images of $\text{Pt}_x\text{Ni}_{1-x}$ BNCs: (a, d) $\text{Pt}_{0.7}\text{Ni}_{0.3}$; (b, e) $\text{Pt}_{0.5}\text{Ni}_{0.5}$; (c, f) $\text{Pt}_{0.1}\text{Ni}_{0.9}$. The HAADF-STEM radial intensity profiles (d, e, f) are taken from the centre to the edge of the cluster and integrated from 0° to 360° . The red dash lines correspond to simulations of cluster STEM intensity profiles with gradient composition evolution. The light grey dotted lines and dark grey dash lines are simulated STEM intensities with pure Pt nanoclusters and pure Ni nanoclusters, respectively.

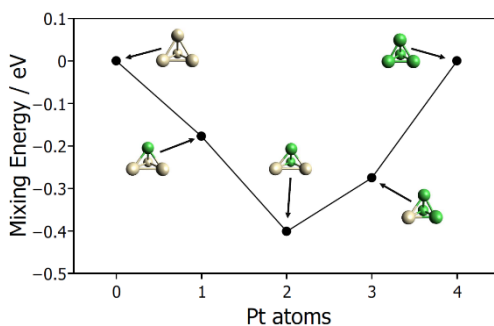


Figure 5.3 DFT calculations of the mixing energy of tetramers: Ni_4 , Pt_1Ni_3 , Pt_2Ni_2 , Pt_3Ni_1 , and Pt_4 .

5.4 Catalytic activity of $\text{Pt}_x\text{Ni}_{1-x}$ nanoclusters

The methanol decomposition reaction on $\text{Pt}_x\text{Ni}_{1-x}$ ($x = 1, 0.9, 0.7, 0.5, 0.3, 0.1, 0$) was tested by ramping the temperature from 100 K to 500 K with 3 reaction cycles, in

order to understand the catalytic activity and stability of the BNCs. The amount of hydrogen desorption (desired product of a DMFC) is related to the catalytic activity of the BNCs, whereas the desorption temperature of the CO molecules is correlated to the CO poisoning effect.

Amorphous SiO₂/Si(100) wafers doped with boron were loaded into the TPD chamber and cleaned by a direct flash heating process up to 700 K, in order to desorb all possible contaminations. The detailed sample preparation process can be found in the method section. The cleaned SiO₂ samples were exposed to 5 Langmuir units (1 L = 1 × 10⁻⁶ torr second) of methanol-d₄ at 100 K to examine the catalytic activity of the SiO₂ support alone. The desorption of methanol from SiO₂ wafers with selected masses is shown in Figure 5.4; all the possible decomposed and recombined species are monitored in the mass spectrum, such as CD₃OD (36), CD₃O (34), CD₂O (32), CDO (30), CO (28), CD₃ (18), CD₂ (16), CD (14), C (12), D₂ (4), CD₄ (20), D₂O (20) and CO₂ (44). It was found that the main methanol (36) desorption occurs at 133 K while a side desorption peak appears around 150 K. These two peaks at 133 and 150 K can be assigned to a multilayer and monolayer methanol desorption from the SiO₂ surface, respectively. The detected desorption features of CO, CD₄/CD₃ and D₂ from SiO₂ wafers were also observed around 133 K and 150 K, meaning these detected molecules were methanol cracking species but not catalytic decomposed molecules of methanol. Thus, SiO₂ was shown to be an inert support showing no catalytic C-O, C-D and O-D bond scission nor C-D and C-O bond formation, within the investigated temperature range. The desorption of methanol was tested on all the cleaned SiO₂ supports, to ensure the cleanness of the samples. No catalytic activity from the SiO₂ support was found, prior to BNC deposition.

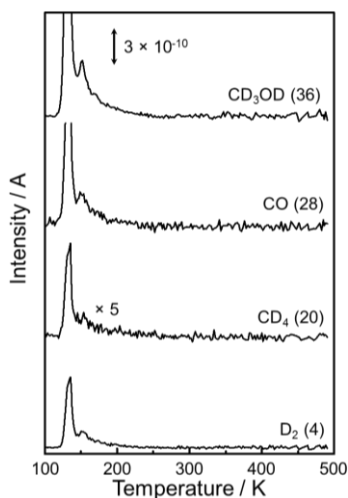


Figure 5.4 Methanol desorption from the cleaned amorphous SiO₂ surface for selected masses stemming from cracking: CD₃OD, CO, CD₄, D₂.

After the cleaning and examination process, the samples were transferred via a home-built UHV transport vessel (base pressure in the 10^{-10} mbar range) to the cluster beam deposition source. The $\text{Pt}_x\text{Ni}_{1-x}$ BNCs were then deposited onto the cleaned SiO_2 supports with 5 ML coverage and transferred under UHV conditions back to the TPD setup; the BNCs deposited samples were also exposed to 5 L methanol at 100 K for methanol adsorption. The TPD results of CO and D_2 from 3 cycles of methanol decomposition, as well as a summary of the temperature of CO desorption peaks and the amount of D_2 desorption for different BNC compositions, are shown in Figure 5.5-a, b, c and d, respectively. CO and D_2 are the only two detectable products by the quadrupole mass spectrometer (QMS), meaning that the C-D bond scission (methanol dehydrogenation) is the dominant reaction. However, due to the detection limit of our QMS, other reactions such as C-O bond scissions, which could occur on the sample surface, cannot be excluded. From the amount of CO and D_2 desorption it is found that, except for the pure Pt nanoclusters, all BNCs show a stable methanol dehydrogenation catalytic activity over the three reaction cycles. For the pure Pt nanoclusters, a high activity was found in the first reaction cycle that dropped to a catalytic activity level similar to those observed in the other Pt-rich BNCs after the first cycle. The CO desorption feature for all the compositions shows one desorption peak, at a temperature that decreases as the Ni fraction increases. For the BNCs with Ni fraction higher than 0.3, the CO desorption temperature is around room temperature, which implies that the CO poisoning effect can be reduced by alloying Pt with Ni for the considered particle size (Figure 5.5-c). Remarkably, the D_2 desorption peak temperature is found in the 260-300 K range and shows no clear dependence on the BNC composition, so the Ni alloyed Pt nanoclusters are still catalytically active. In the Pt-rich BNCs, the D_2 desorption feature is extends to 400 K. The D_2 molecules desorbed at high temperature can be attributed to the D_2 molecules desorbed from the Pt surface,¹⁸⁶ while no desorption feature is observed in the Ni-rich BNCs due to the presence of a Ni enriched shell at their surface. The catalytic dehydrogenation activity of methanol is stable for all the $\text{Pt}_x\text{Ni}_{1-x}$ BNCs and pure Ni NCs during the three reaction cycles. The pure Pt NCs showed the highest catalytic activity in the first cycle, but their activity decreased by about 50% in the subsequent cycles, while the CO desorption temperature remained around 410 K. This reduced activity may be assigned to the lower accessibility of the methanol molecules to the active reaction sites on the cluster surface.¹⁵⁵ Interestingly a low CO desorption temperature is observed in Ni rich nanoclusters and pure Ni clusters. However, the typical strong CO-Ni interaction results in a high CO desorption temperature at around 400 K.¹⁸⁷⁻¹⁸⁸ The low temperature of CO desorption feature indicates that the clusters can interact with the trace O_2 molecules present inside the UHV chambers whereas Ni oxides are formed on the cluster surface.¹⁸⁹ Therefore, CO molecules are desorbed from the Ni oxide surface at room temperature, resulting in room temperature desorption of CO molecules.

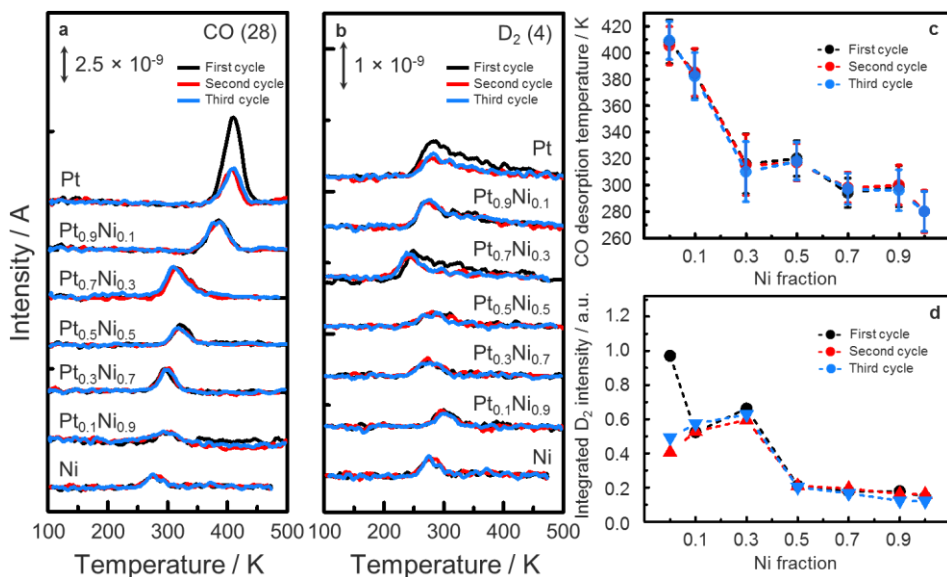


Figure 5.5 TPD spectra of methanol decomposition on Pt_xNi_{1-x} BNCs of different compositions on SiO₂ supports, showing the desorption of (a) CO and (b) D₂. Overviews of the (c) CO and (d) D₂ desorption temperatures as a function of the Ni fraction in the BNCs.

5.5 Oxidation states and atomic structure of Pt_xNi_{1-x} nanoclusters

XPS measurements were conducted on the BNCs with Pt rich to Ni rich compositions. The composition and the presence of oxidized components as well as their amount can be revealed by deconvolution of the Pt 4f and Ni 2p peaks. The best fits of the high-resolution XPS core-level spectra in the Pt 4f and Ni 2p energy region, as well as the summary plots of Pt 4f and Ni 2p peaks with different phases are presented in Figure 5.6. It was found that Pt atoms within the BNCs mainly remained metallic and that a large fraction of Ni atoms was oxidized into Ni hydroxide/oxide phases after the samples were exposed to air. Furthermore, a structure dependent oxidation rate is observed. Pt 4f peaks can be deconvoluted into three sets of Pt 4f_{7/2} and Pt 4f_{5/2} peaks, from pure Pt NCs to Pt_{0.5}Ni_{0.5} BNCs corresponding to metal Pt (71.3 eV and 74.6 eV), PtO (72.4 eV and 75.7 eV) and PtO₂ (73.8 eV and 77.1 eV). There is a broad peak appearing between 66 eV and 69 eV, when the Ni fraction is above 0.5. This can be assigned to convoluted Ni 3p peaks. The intensity evolution of these Ni 3p peaks is consistent with the BNC composition. The pure Pt sample is the most oxidized. Its oxidation rate slightly trends down as the Ni fraction increases in the Pt rich cases. However, when the Ni fraction is higher than 0.5, the oxidation rate drops significantly. This observation is consistent with the STEM observation that the Pt atoms are

predominantly present in the BNC core. This indicates that their oxidation is prevented by the Ni atoms forming the BNC outer shell. Similarly the Ni atom oxidation state varies with the BNC composition. The Ni $2p_{3/2}$ and Ni $2p_{1/2}$ peaks can be deconvoluted into Ni metal (852.5 eV and 869.6 eV), NiO (853.2 eV and 870.7 eV), Ni(OH)₂ (855.9 eV and 873.4 eV) and NiOOH phases (860.7 eV and 878.0 eV). The peaks centred around 863.6 eV and 880.8 eV are assigned to the satellite peaks of Ni $2p_{3/2}$ and Ni $2p_{1/2}$. In the Ni rich BNCs, more than 70% of the Ni atoms are oxidized. Their oxidation rate tends to increase with the Ni fraction, reaching a maximum in Pt_{0.3}Ni_{0.7} BNCs. This can be attributed to the fact that Ni oxide and Ni hydroxide are stable oxide phases; with the alloying effect, the electronic structure of Ni atoms is modified by neighbouring Pt atoms favouring the Ni atoms oxidation when Ni atoms are present at the BNC shell.^{168-169, 190} As the Ni fraction in BNCs further decreases, the cluster structure consists of a Ni enriched core and Pt enriched shell, resulting in an oxidation rate of Ni decreasing rapidly.

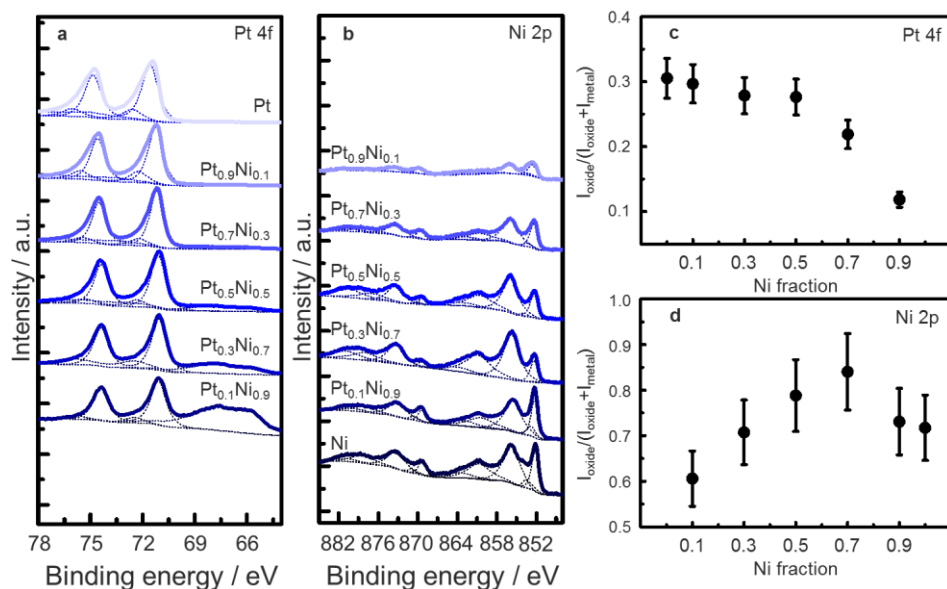


Figure 5.6 Pt 4f (a) and Ni 2p (b) XPS spectra of the Pt_xNi_{1-x} BNCs on SiO₂ wafers from x = 0.9 to 0.1 with pure Pt and Ni NPs. The Pt 4f peaks of Pt 4f_{7/2} and Pt 4f_{5/2} are deconvoluted into Pt metal phase (71.3 eV and 74.6 eV) and Pt oxide phases (72.4 eV, 75.7 eV, 73.8eV and 77.1 eV); the Pt 4f XPS intensity ratio of the oxide phase is summarized in (c). The Ni 2p peaks of Ni 2p_{3/2} and Ni 2p_{1/2} are deconvoluted into a Ni metal phase (852.5 eV and 869.6 eV) and Ni hydroxide/oxide phases (853.2 eV, 870.7 eV, 855.9 eV, 873.4 eV, 860.7 eV, 878.0 eV, 863.6 eV and 880.8 eV); the Ni 2p XPS intensity ratio of the oxide phase is summarized in (d).

5.6 DFT calculations of the electronic band structure of $\text{Pt}_x\text{Ni}_{1-x}$ nanoclusters and CO-Pt interactions

In order to understand the origin of the decrease in CO desorption temperature with an increasing Ni fraction, a systematic band structure analysis was performed with DFT calculations in the representative nanoclusters Pt_{459} , Pt_{561} , $\text{Pt}_{417}\text{Ni}_{144}$ and $\text{Pt}_{353}\text{Ni}_{106}$ with two types nanoclusters. The 459 atom nanoclusters (Pt_{459} and $\text{Pt}_{353}\text{Ni}_{106}$, ca. 2.4 nm in diameter) was constructed the Wulff construction to obtain nanoclusters with small (100) facets, while the 561 atom nanoclusters (Pt_{561} and $\text{Pt}_{417}\text{Ni}_{144}$, ca. 2.7 nm in diameter) was generated with larger (100) facets. Two types of nanoclusters with different structures are shown in Figure 5.7. The Pt-Ni nanoclusters were constructed with a Pt surface (with few Ni atoms) while the inner structure was modelled with a random Pt-Ni alloy as observed by HAADF-STEM in $\text{Pt}_{0.7}\text{Ni}_{0.3}$ nanocluster (Figure 5.2-a, d). Other possible atomic orderings were also considered such as random Pt-Ni core with Pt shell, two different fully random alloy nanoclusters and Ni-core/Pt-shell cluster were locally optimized. The random core-Pt shell structure had the lowest energy. The Ni-core/Pt-shell the next lowest with a 15.1 eV higher in total energy (or 32.9 meV/atom) compared to the random core-Pt shell structure. The two random configurations had almost the same energy, 16.5 and 16.6 eV (or 35.9 and 36.2 meV/atom) higher than the random core-Pt shell structure. These total energy calculation results are in very good agreement with the experimental result in Figure 5.2. Therefore, further calculations were performed with random core-Pt shell structures nanoclusters.

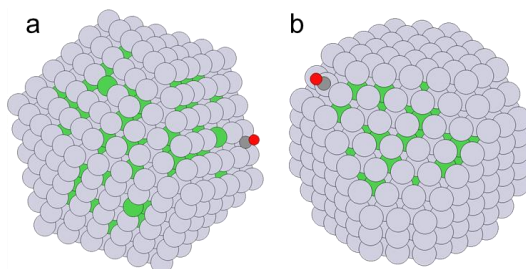


Figure 5.7 nanoclusters with smaller (100) surface was modelled with $\text{Pt}_{417}\text{Ni}_{144}$ nanocluster using Wulff construction (a) and $\text{Pt}_{353}\text{Ni}_{106}$ nanocluster with larger (100) surface (b). The CO adsorption on bridge sites are also illustrated. The grey, green, dark grey, and red balls represent, Pt, Ni, C, and O atoms, respectively.

It was consistently found that the direction of the electron transfer is always from Pt to Ni atoms, with all the charge analysis methods. A summary of the average charge on Pt and Ni atoms with the different charge analysis methods is listed in Table 5.1. A d-electron population analysis also revealed that the electronic structure of Pt atoms is

modified by the neighbour Ni atoms. The Löwdin population analysis¹⁹¹ was performed on the Pt₃₅₃Ni₁₀₆ and Pt₄₁₇Ni₁₄₄ nanocluster as implemented in the CP2K code for Pt with a maximum electron population of 10.0. The results clearly show that the d-electron population of the Pt atoms is reduced by the nearby Ni atoms. In Pt₃₅₃Ni₁₀₆ BNCs, the d-electron population of Pt atoms at the (111) surface that is 8.13 with subsurface Pt atoms is reduced to 7.96 with subsurface Ni atoms. A similar d-electron population reduction trend was observed for Pt atoms at (100) and (111) surfaces as well as at edge sites in Pt₄₁₇Ni₁₄₄ cluster. (Table 5.2)

Table 5.1 Summary table presenting the charge of Pt and Ni atoms using Hirchfeld, Bader, Löwdin and Mulliken analysis methods. The Mulliken analysis was not performed for the larger nanocluster. The unit of transferred charge presented here is elementary charge.

	Pt ₃₅₃ Ni ₁₀₆		Pt ₄₁₇ Ni ₁₄₄	
	Ni	Pt	Ni	Pt
Hirchfeld method	-0.141	0.042	-0.154	0.053
Bader method	-0.284	0.085	-0.289	0.101
Löwdin method	-1.053	0.316	-1.13	0.389
Mulliken method	-0.046	0.014		

Table 5.2 Summary table of d-electron population calculation based on the Löwdin and Mulliken methods. The <Ni> and <Pt> are the averages value of Ni or Pt atoms in the nanoclusters and Pt/Ni (Pt/Pt) denotes Pt atoms on the 111 surface (results for Pt on the (100) surface is given for the larger nanocluster), with a Ni or Pt subsurface atom. The Pt/X numbers are an average of few sites. The Mulliken analysis was done only for the Pt₃₅₃Ni₁₀₆ nanocluster.

		Pt ₃₅₃ Ni ₁₀₆				Pt ₄₁₇ Ni ₁₄₄			
		<Ni>	<Pt>	Pt/Ni	Pt/Pt	<Ni>	<Pt>	Pt/Ni	Pt/Pt
Löwdin method	(111)	8.39	8.00	7.96	8.13	8.41	7.97	8.05	8.19
	(100)							7.92	8.23
Mulliken method	(111)	8.67	8.65	8.60	8.66				

Table 5.3 Summary table of the CO-Pt binding energies of Pt atoms on various sites. Some of the sites with no number given are either unstable or have not been calculated. The unit of CO-Pt binding energy here is eV.

		Pt ₃₅₃ Ni ₁₀₆		Pt ₄₅₉	Pt ₄₁₇ Ni ₁₄₄		Pt ₅₆₁
		Pt/Ni	Pt/Pt	Pt	Pt/Ni	Pt/Pt	Pt
Edge	Bridge	-1.76	-1.93	-1.94	-1.77	-2.02	-2.00
100	Bridge	-1.65	-1.72	-1.69	-1.80	-1.95	-2.06
111	Bridge	-1.21	-1.57				
	Hollow	-1.10		-1.53	-1.36	-1.50	-1.57
	Top	-1.06	-1.46				-1.52

In $\text{Pt}_{353}\text{Ni}_{106}$ nanoclusters, the d-band centre of the Pt atom with subsurface Pt atom is -2.57 eV, with respect to the Fermi level, whereas for Pt with a Ni subsurface atom it is -2.81 eV while the average Pt d-band centre is -2.67 eV. It is generally considered that a lower d-band centre results in a lower molecule binding energy.¹⁶⁹ The surfaces of transition metals and noble metals do not only present open sp bands to form bonds with adsorbates, but also d states that enables a further bonding interaction between the metal d states and the adsorbate related states. The bonding interaction is determined by the degree of occupation of the antibonding state between the adsorbate state and the metal d states. The higher the d state energy relative to the Fermi level, the emptier are the antibonding states available for bond formation and the stronger the adsorption bond is.¹⁹² Therefore d-electrons are important in the binding of CO with metal atoms, implying that reducing the d-band population and lowering its centre should lead to a lower CO-metal binding. In order to verify this argument, calculations in which CO molecules are placed on various surface sites of the nanoclusters were performed. For each situation the binding energy of CO onto Pt was calculated. The correlation between the d-band populations and the CO binding energies presented in Figure 5.8 and clearly shows that the behaviour is consistent with the d-band theory. A summary of the calculated CO binding energies on different surface sites with Ni or Pt as subsurface atoms is presented in Table 5.3. In general, no matter whether the Pt atoms are located at the (100) or the (111) surfaces, or at edge sites, the CO binding energy is always lowered when a Ni atom is present below the investigated Pt atom. Therefore, the decreased CO desorption temperature on $\text{Pt}_x\text{Ni}_{1-x}$ BNCs can be assigned to a local modification of the Pt d-band induced by Ni atoms, which results in a weakened CO-Pt interaction.

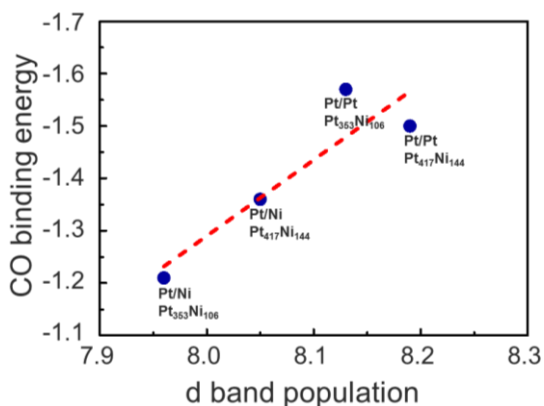


Figure 5.8 Plot of the d-band population and CO binding energy on the Pt atom at the (111) surface of the $\text{Pt}_{353}\text{Ni}_{106}$ and $\text{Pt}_{417}\text{Ni}_{144}$ cluster with Pt or Ni subsurface atoms (blue cycles). The linear fit is presented as a dashed red line.

5.7 Conclusions

The atomic arrangement, the catalytic activity and the electronic structures of $\text{Pt}_x\text{Ni}_{1-x}$ BNCs with diameter centred around 2.0 nm synthesized by the laser ablation method are studied by HAADF-STEM, TPD and XPS. It is shown by HAADF-STEM that these BNCs feature a composition-tunable atomic arrangement with minority element enriched cores and majority element enriched shell. The TPD methanol dehydrogenation experiments show that C-D and O-D bond scission occur on the cluster surface with CO and D_2 as products. The CO poisoning effect is reduced by alloying Pt with Ni. The underlying mechanism is revealed by DFT calculations and is strongly validated by several analysis methods can be described by a significant local Pt d-band structure modification by subsurface Ni atoms, resulting in a weakened Pt-CO interaction and a reduced CO desorption temperature. From the catalytic point of view, $\text{Pt}_x\text{Ni}_{1-x}$ BNCs are shown to be stable under methanol dehydrogenation after several reaction cycles. Furthermore, the catalytic activity of Pt rich BNCs is preserved, which means that Pt atoms prefer to be located at the surface of the nanoclusters and that the active sites are not blocked by the presence of Ni atoms on the BNC surface.

Chapter 6

Au nanoclusters modified TiO₂ films toward stearic acid degradation as self-cleaning surfaces under visible light

The results presented in this chapter are based on:

TiO₂ films modified with Au nanoclusters as self-cleaning surfaces under visible light

Ting-Wei Liao,^a Sammy W. Verbruggen,^{b,c} Nathalie Claes,^d Anupam Yadav,^a Didier Grandjean,^a Sara Bals^d and Peter Lievens^a

Nanomaterials, [DOI:10.3390/nano8010030](https://doi.org/10.3390/nano8010030) (2018)

^a Laboratory of Solid-State Physics and Magnetism, KU Leuven, Belgium.

^b Sustainable Energy, Air & Water Technology (DuEL), University of Antwerp, Belgium.

^c Centre for Surface Chemistry and Catalysis, KU Leuven, Belgium.

^d Electron Microscopy for Materials Research (EMAT), University of Antwerp, Belgium.

S.W.V., T.-W.L., A.Y., D.G. and P.L. conceived and designed the experiments; S.W.V., T.-W.L. and A.Y. prepared Au nanoclusters modified films. N.C. and S.B. performed the SEM experiments. The photocatalysis experiments were conducted by S.W.V. T.-W.L. and S.W.V. wrote first draft of the manuscript and all authors contributed to writing and proofreading.

Abstract In this chapter, we applied cluster beam deposition (CBD) as a new approach to produce highly efficient plasmon-based photocatalytic materials. Au nanoclusters synthesized in gas phase were deposited on TiO₂ (P25)-coated silicon wafers at different coverages, ranging from 2 to 8 atomic monolayer (ML) equivalents. Scanning Electron Microscopy (SEM) images of the Au nanoclusters modified P25 films show that the TiO₂ surface is uniformly covered by Au nanoclusters that remain isolated at low coverage (2 ML, 4 ML) in contrast to the higher coverage (8 ML). A distinct relation between Au cluster coverage and their photocatalytic activity towards stearic acid photo-oxidation was measured, both under UVA and green light illumination. The 4 ML coverage Au nanoclusters sample showed the best photo-oxidation performance under green light illumination (FQE 1.6×10^{-6} stable at least for 93 hours). This result demonstrates that the proposed gas phase Au cluster deposition technique is a new and valuable tool for the fabrication of visible light active plasmonic photocatalysts.

6.1 Introduction

Various semiconductor-based photocatalysts, such as TiO₂, ZnO, SrTiO₃, Fe₂O₃, FeOOH, WO₃, CdS and III–V compound semiconductors, have drawn considerable attention in recent years,¹⁹³⁻²⁰⁴ due to their multiple promising applications in solar energy harvesting,²⁰⁵⁻²⁰⁷ water cleaning,²⁰⁸⁻²¹⁰ anti-bacterial surfaces,²¹¹ organic pollutants removal²¹² and self-cleaning surfaces²¹³ as new construction materials for the improvement of the urban environment. The main factors that determine the photocatalytic properties of semiconductor-based photocatalysts are band gap, position of conduction band and valence band, mobility of photo-generated charge carriers and material stability.⁴⁵ Although titanium dioxide (TiO₂) is a good photocatalyst towards oxidation of organic compounds under ultraviolet (UV) light,⁴⁷ its photocatalytic properties need to be improved significantly in the visible range, especially under green light that corresponds to the maximum output range of the sun's total irradiance spectrum. Surface modification with metal nanoparticles improves the photoabsorption rate in the visible range by (amongst other phenomena) hot electron injection effects produced by their localized surface plasmon resonance (LSPR).²¹⁴⁻²¹⁶

Most of the metal nanoparticle-TiO₂ composites nowadays are synthesized in solution by various wet chemistry synthesis protocols that generally include inorganic acid in the particle synthesis, toxic ligands to protect the metal particles and functional groups that stabilize the nanoclusters (NCs) on the TiO₂ surface.^{206, 217-218} It has been shown that the performance of the NPs is highly affected by the chemical environment during the preparation processes. Therefore, the use of acids and ligands in wet chemistry synthesis methods can have a significant inference on the NCs.²¹⁹ Furthermore, by ensuring the NCs are only present at the surface can reduce the usage of the amount of noble metals. Cluster beam deposition (CBD) greatly benefits from producing

nanoclusters in a well-controlled noble gas environment and then soft landing them on supports while maintaining their preformed structure with excellent control over size, shape, and composition.²³ In order to produce clean and controllable photocatalytic systems with only desired materials, physical cluster beam deposition methods that produce size-selective NCs in noble gas environments, free of unwanted ligands or functional groups, present a very attractive alternative.

In this study, we report on the significant improvement of the photocatalytic activity of TiO₂ P25 films modified with AuNCs produced by the laser ablation cluster beam deposition technology, with equivalent coverage ranging from 0 ML to 8 ML (1 ML $\sim 1.5 \times 10^{15}$ atoms/cm², ~ 0.5 $\mu\text{g}/\text{cm}^2$) towards stearic acid degradation under UV (365 nm) and green LED light (515 nm) irradiation. The photocatalytic efficiency of AuNCs modified TiO₂ films with an equivalent cluster coverage of 4 ML was enhanced by a factor of 4 compared to pristine TiO₂ P25 under green LED irradiation while no significant effect of AuNCs on the activity was noticed under UV exposure.

6.2 Sample preparation and methods

The preparation of TiO₂ P25 power films on SiO₂ surfaces and the surface modification of AuNCs on the oxide films are described in the current section. The experimental methods are also introduced in this section.

6.2.1 Preparation of Au nanoclusters modified films

TiO₂ P25 powder (Evonik, Hanau-Wolfgang, Germany, 70% of anatase and 30% of rutile) films were prepared by spin coating 1 wt % of titania powder ethanol suspension at 1500 rpm onto low-doped Si wafers with a length of 3 cm and a width of 1.5 cm. The samples are subsequently dried overnight at 70°C. Next, TiO₂ P25 powder films were modified with AuNCs with equivalent atomic coverages of 0 ML, 2 ML, 4 ML and 8 ML by depositing gas phase AuNCs produced with a laser ablation cluster source. The nanoclusters are produced by pulsed laser (10 Hz, Nd:YAG lasers, Spectra Physics, Santa Clara, CA, USA, INDI) ablation of Au (ACI Alloy, San Jose, CA, USA, purity 99.995%) plate targets and condensation in a high pressure (9 bar) of inert gas (He, purity 99.9999%).⁵⁹ The cluster source was cooled by liquid nitrogen, resulting in a NC temperature of about 100 K. In this study, the cluster size distribution was optimized for sizes in the order of 1000 atoms. Following a supersonic expansion into vacuum of the helium carried NC molecular beam, AuNCs were soft-landed (~ 500 m/s) on the P25 films in a ultra-high vacuum (UHV) cluster deposition chamber under a base pressure below 5×10^{-10} mbar.¹¹⁹ The cluster flux was monitored by a quartz crystal microbalance (QCM) and the cluster coverage controlled by the deposition time assuming a fixed cluster flux.

6.2.2 Film characterization

Secondary electron SEM images of TiO₂ P25 films and AuNCs modified P25 films were acquired using a FEI Quanta 250 FEG environmental scanning electron microscope (Thermo Fisher Scientific - FEI, Hillsboro, OR, USA). The microscope was operated at 15 kV with a chamber pressure of 130 Pa. UV-Vis absorption spectra of the AuNCs were collected as-deposited on the films using a double beam UV2600 spectrophotometer (Shimadzu, Kyoto, Japan) equipped with film holders attached to a BaSO₄ coated integrating sphere of 60 mm in diameter. A pristine TiO₂ P25 film was used as a background sample.

6.2.3 Photocatalysis towards stearic acid degradation

AuNCs modified films were then spin coated with 100 μ L of a 0.25 wt % stearic acid solution in chloroform at 1000 rpm for 1 min and the stearic acid coated films dried in an oven at 70 °C for 15 min. Finally the samples were exposed to the ambient overnight to establish a thermal and humidity equilibrium before the photocatalytic measurements. The photocatalytic activity tests were performed at ambient conditions at a temperature of 32 ± 2 °C and a relative humidity of $34 \pm 3\%$ (monitored with a Humidity and Temperature Transmitter (Vaisala, Helsinki, Finland)) under UV and green light irradiation. The photon flux of UV and green light LED lamp emission were 2.9×10^{15} photons/cm²/s in the 300 nm to 400 nm spectral range and 8.1×10^{15} photons/cm²/s in the 450 nm to 600 nm spectral range, respectively, as measured with an Avantes Avaspec Spectroradiometer (Avantes BV, Apeldoorn, The Netherlands).

The degradation of stearic acid during illumination was measured by recording FTIR absorbance spectra (Thermo Nicolet 6700, Thermo Fisher Scientific, Madison, WI, USA) of the solid film with a 1 cm⁻¹ resolution and with the sample placed at a fixed angle of 9° with the IR beam in order to minimize internal reflection effects. The quantity of stearic acid remaining on the sample surface was determined by integrating the area of the IR band between 2800 and 3000 cm⁻¹, which consists of the asymmetric $\nu_{as}(-\text{CH}_3)$ vibration at 2958 cm⁻¹, the asymmetric $\nu_{as}(-\text{CH}_2)$ at 2923 cm⁻¹ and the symmetric $\nu_s(-\text{CH}_2)$ at 2853 cm⁻¹ of the stearic acid hydrocarbon chain, and the results were plotted versus illumination time. The degradation experiments under UV illumination were performed over 15 min and the experiments under green light were monitored over a period of 93 h. This methodology was validated in earlier work of various authors.^{215, 220-}

6.3 Morphology of Au nanoclusters modified TiO₂ powder films

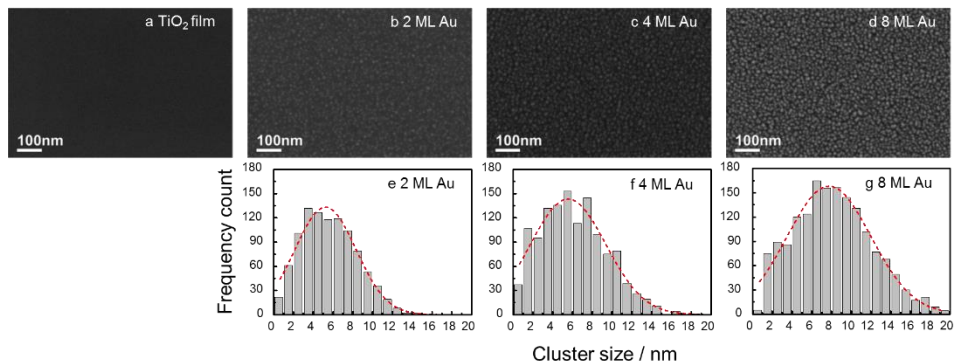


Figure 6.1 SEM images of Si wafers supported TiO₂ P25 (a). Gas phase Au cluster modified P25 films with 2 ML (b), 4 ML (c) and 8 ML (d) equivalent coverage as well as size distribution histograms of 2 ML (e), 4 ML (f) and 8 ML (g) samples. The red dash lines in the histograms are the fittings of cluster distributions.

Figure 6.1-a shows a Scanning Electron Microscopy (SEM) image of the TiO₂ P25 film, supported on a Si wafer. TiO₂ P25 films are uniform and no apparent regions or island discontinuities are observed on the sample surface at this scale. SEM images of 2 ML, 4 ML and 8 ML of AuNCs modified TiO₂ P25 films are presented in Figure 6.1-b–d, respectively. Due to the lower ionization potential of Au compared to TiO₂, the electron intensity from AuNCs is higher allowing AuNCs to be revealed. The cluster size is determined by the cluster projected area and the cluster size distributions are presented in Figure 6.1-e (2 ML), Figure 6.1-f (4 ML) and Figure 6.1-g (8 ML). All the coated TiO₂ P25 films are homogeneously covered by AuNCs. At the lowest coverage (2 ML) most of AuNCs have an average size of 5.2 nm and appear individually without any sign of aggregation, while at the highest coverage (8 ML) AuNCs with a larger size of 7.8 nm and irregular shapes are observed suggesting a significant level of cluster coalescence. The morphology of the 4 ML sample consists mainly of individual nanoclusters with an average size of 5.5 nm very similar to the NCs in the 2 ML sample. The mobility of the Au atoms on TiO₂ has been studied by Scanning Tunneling Microscopy (STM) and the binding energy of Au atoms on TiO₂ was investigated by Density Functional Theory (DFT). Both of these studies show that the binding energy of Au atoms and nanoclusters is low enough so that Au nanoclusters can become mobile on the TiO₂ surface.²²²⁻²²³ Therefore, when the coverage of Au nanoclusters increases, the chance of Au nanoclusters to coalesce will increase and result in larger and irregularly shaped particles.

Optical characterization of the AuNCs revealed that for all three modified samples, a typical gold surface plasmon resonance (SPR) band is observed at a wavelength of ca. 520 nm, as expected for small gold nanoclusters (Figure 6.2). The absorbance intensity of the SPR band increases as the gold loading on the sample increases. It is also striking that the absorption onset for the 8 ML sample is strongly red-shifted compared to the other samples and the SPR band is broadened. This is in full agreement with the larger average particle size, degree of coalescence, and irregular shape of the particles observed by SEM for this particular sample.

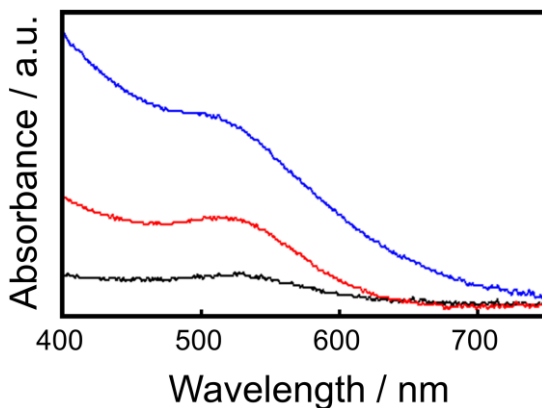


Figure 6.2 UV-Vis absorption spectra of 2 ML (black), 4 ML (red) and 8 ML (blue) AuNCs on TiO₂ films, with a pristine TiO₂ film as the background sample.

6.4 Photo-degradation of stearic acid on Au cluster modified films

The integrated area of the Fourier-transform infrared (FTIR) absorbance spectra between 2800 and 3000 cm⁻¹ of the C-H stretch as a function of time with different coverage is shown in Figure 6.3-a, b for stearic acid degradation under UV and green LED light, respectively. The quantity of stearic acid remaining on the sample surface decreased linearly with time, indicating a zero order degradation kinetics. This is consistent with the self-cleaning behavior of plasmonic photocatalysts reported in earlier work.²¹⁴ A series of blank reference experiments was done in our previous work to exclude the possible contributions of photolysis, plasmonic heating or direct plasmonic catalysis on the noble metal nanoclusters by investigating a blank silicon wafer and samples with direct deposition of noble metal nanoclusters but without TiO₂. The results showed that these samples present no activity under either UV, 490 nm LED light, nor simulated solar light.²¹⁴

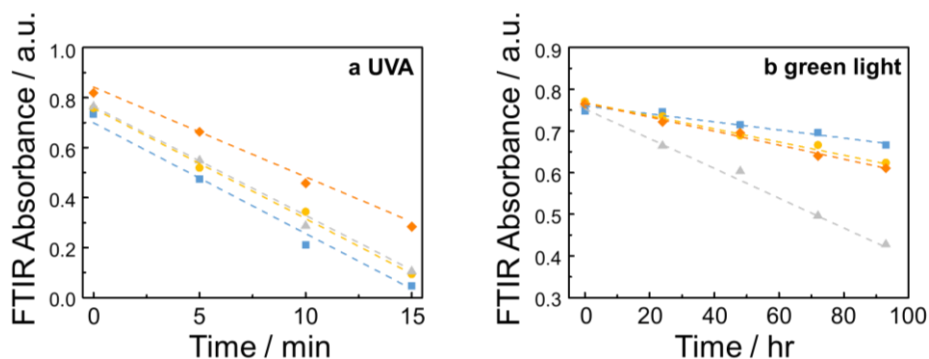


Figure 6.3 Evolution of integrated FTIR absorbance of stearic acid between 2800 to 3000 cm^{-1} as a function of illumination time on the sample of pristine TiO_2 P25 film (blue ■) and Au cluster modified TiO_2 P25 films with 2 ML (yellow ●), 4 ML (grey ▲) and 8 ML (orange ◆) Au coverages under (a) UV and (b) green light illumination.

In Figure 6.3 blue lines correspond to the TiO_2 P25 films without Au cluster modification while the yellow, grey and the orange lines to TiO_2 P25 films modified with 2 ML, 4 ML, and 8 ML of AuNCs, respectively. The photocatalytic activities of TiO_2 P25 under UV towards stearic acid degradation were not improved upon modification with AuNCs. The activity was even disrupted to some extent at the highest coverage of 8 ML. Under green LED light illumination, however, all the photocatalytic activities of AuNCs modified TiO_2 films were enhanced significantly. These results are preferably expressed as “Formal Quantum Efficiency” (FQE) for comparison,²²⁰ which is defined as

$$FQE = \frac{\text{the rate of stearic acid degradation in molecules/cm}^2/\text{s}}{\text{the rate of incident light in photons/cm}^2/\text{s}} \quad 6.1$$

The FQE under UV and green light illumination as a function of Au coverage are presented in Figure 6.4-a, b, respectively.

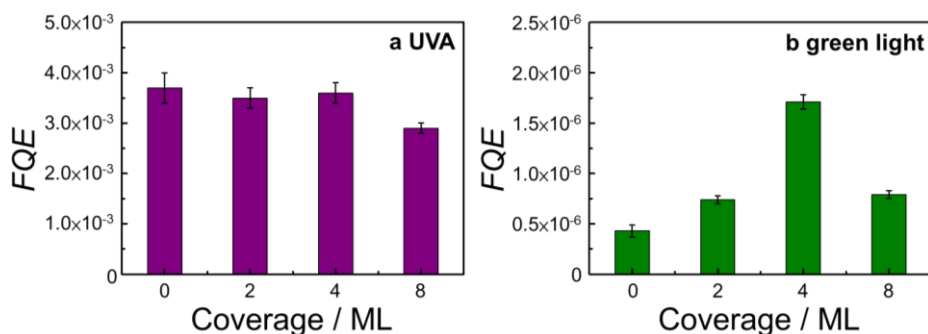


Figure 6.4 FQE under (a) UV and (b) green light illumination as a function of Au cluster coverage on TiO_2 P25.

Under UV illumination, the performance of all samples is similar. The *FQE* of the pristine TiO₂ P25 reference film under UV was measured to be 3.7×10^{-3} . The value measured by Mills et al. was 4.8×10^{-3} for the same type of catalyst, which is in very good agreement with our result given the fact that their film was prepared with a three-time dipping-drying process that leaves a larger amount of catalyst on the film.²²⁰ This result is also in line with the findings of Allain et al. for a mesoporous TiO₂ film (1.02×10^{-3}).²²⁴ Our results show that modification with noble metal NCs did not improve the activity of the pristine reference sample under UV irradiation nor disrupt it until an equivalent Au coverage of 8 ML is reached. For the latter 8 ML sample a 20% decrease in degradation efficiency is observed under UV illumination. This may be attributed to an incremental blocking of the catalyst active sites, or to the fact that a larger fraction of incoming light is prevented from reaching the catalyst in comparison to the samples featuring lower Au coverages.

Under pure green visible LED light, a very clear positive effect in the presence of metallic AuNCs for all the samples is observed. This is ascribed to the plasmonic effect of AuNCs, active in this wavelength range. At first, it should be noted that the pristine TiO₂ P25 features a small photocatalytic activity under green LED light illumination, which is rather unexpected and controversial. In principle visible light cannot initiate photocatalytic reactions on a TiO₂ surface, as its photon energy is much lower than the TiO₂ P25 band gap of 3.1 eV.²²⁵ A possible explanation could be related to the presence of defect states present in the band gap of TiO₂ P25 that enable the generation of charge carriers in pristine TiO₂ P25 upon pure visible light excitation as has been demonstrated by means of Electron Paramagnetic Resonance (EPR) measurements.²²⁶ This low basal activity under visible light was also observed in our previous study and could not be attributed to thermal degradation nor to pure photolysis processes.²¹⁴

6.5 Discussion

Upon modification of TiO₂ with AuNCs, a significant increase of the photocatalytic efficiency under 515 nm green light is observed for all coverages. Although a modest increment is found for 2 ML AuNCs modified TiO₂ P25 films, a *FQE* 4 times greater than the reference and 2.5 times greater than the 2 ML sample was measured in the 4 ML sample. However, further doubling the AuNC coverage to an equivalent of 8 ML resulted in a lowered efficiency, which may again be explained by an excessive blocking of the active sites and/or by unwanted light scattering. The hypothesis is supported by the observation of the SEM images. The size of the NCs at the surface of the 8 ML sample is larger compared to the other lower coverages, which is suggesting cluster aggregation and coalescence happened on the sample surface. This is also confirmed by broadening of the UV-Vis absorption spectrum of the nanoclusters. Furthermore, the surface of the

TiO₂ P25 powder film is almost fully covered by AuNCs. The photocatalytic activity of pure noble metal nanoclusters was studied in previous work and it was shown there is no photocatalytic nor photo-thermal activity of noble metal nanoparticles as such.²¹⁴ It was also studied that the active site is located at the metal-support site. The availability of both metal and support are necessary for the reaction to occur. Therefore, as the AuNCs coverage increases on the TiO₂ surface, the accessibility of the AuNCs-TiO₂ site reduces.²²⁷ As a combined result of these effects, the photocatalytic activity of 8 ML Au cluster modified TiO₂ P25 film is reduced.

AuNCs feature a strong light absorption in the visible region where the absorbed energy can induce resonant oscillation of the free electrons present in the Au nanoclusters.²²⁸ The trapped energy can then be transferred to the coupled semiconductor substrate by a variety of mechanisms.²²⁹ This was highlighted by electron paramagnetic resonance (EPR) studies of Au-TiO₂ composites that showed that hot electron transfer from a gold excited plasmonic state into the TiO₂ conduction band is an important underlying mechanism (Figure 6.5).^{228, 230}

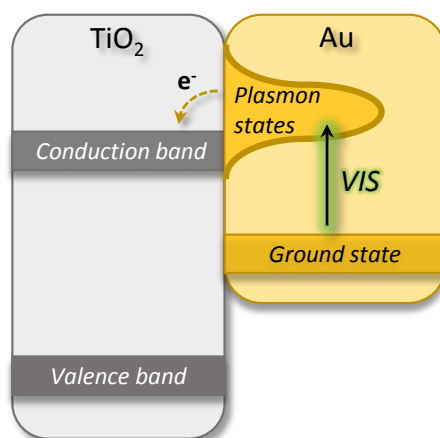


Figure 6.5 Schematic illustration of hot electron transfer from an excited plasmonic state on the gold nanoparticle, to the TiO₂ conduction band. Modified from reference.²¹²

One of the other advantages of the gas phase Au cluster deposition method, is that the active particles are exclusively located at the surface of the powder film where they can efficiently interact with incident photons, and not in the bulk. This increases the efficiency of material usage. For instance, the weight per area of 4 ML AuNCs is estimated to be only 2 $\mu\text{g}/\text{cm}^2$.

Although the IUPAC recommends to express the photocatalytic activity in terms of *FQE*, there is not yet a standard way to present the photocatalytic activity in the

photocatalysis community. Therefore, it is difficult to compare the photocatalytic activity of our system to recent literature results. The 4 ML AuNCs film demonstrates higher photocatalytic activity compared to our previous studies on Au-Ag bimetallic plasmonic particles. It was found that TiO₂ P90 (90% anatase, 10% rutile) modified with 1.5 wt % of Au_{0.3}Ag_{0.7} plasmonic alloy nanoparticles under 490 nm teal light illumination resulted in a *FQE* of 0.39×10^{-6} .²¹⁵ In the present work, the *FQE* of 4 ML AuNCs modified TiO₂ P25 under 515 nm green light is 1.7×10^{-6} . In another study Au_xAg_{1-x} ($x = 0.2$ to 1) nanoparticles were deposited on TiO₂ P25, resulting in a so-called rainbow photocatalyst that was 16% more effective than pristine TiO₂ P25 under both simulated and real solar light toward stearic acid degradation (i.e., combined UV and visible light irradiation).²¹⁴ The excellent photocatalytic activity enhancement observed under green light obtained with pure AuNCs in this study suggests that fabricating a similar “rainbow” photocatalyst using our physical gas phase cluster deposition method may lead to further enhancements of the photocatalytic activity, and is the subject of ongoing research.

6.6 Conclusions

We have demonstrated the excellent photocatalytic self-cleaning activity of a series of TiO₂ P25 films modified with gas phase AuNCs synthesized by Cluster Beam Deposition. Photocatalytic stearic acid degradation is achieved under UV and green light illumination. At an atomic equivalent Au cluster coverage of 2 ML and 4 ML, the photocatalytic activities of the TiO₂ films under UV are not influenced by the presence of the AuNCs; however, the photocatalytic activities of these two films under green LED light, especially for the sample with 4 ML coverage, are greatly improved. Increasing the AuNC coverage to 8 ML does not lead to any further improvement of the photocatalytic activity, as it even starts to disrupt the photocatalytic activity. Altogether, this work presents a versatile and valuable strategy for the fabrication of noble metal modified photocatalytic surfaces with a high control over the cluster size and coverage, without using aggressive solvents nor organic ligands to reduce the negative effect of these molecules.

General Conclusions and Perspective

The main objective of this thesis was to design, produce and characterize novel catalysts based on mono- and bi-metallic deposited nanoclusters synthesized by cluster beam deposition methods. Composition controlled BNCs were successfully synthesized and deposited on various supports for structural and catalytic investigations. The structures of the BNCs were characterized by electron microscopy and X-ray spectroscopy techniques. The catalytic activities of the BNCs towards CO oxidation and methanol decomposition were studied in an industrial relevant gas flow reactor and a homebuilt temperature programmed desorption setup. Photocatalytic properties of cluster modified TiO₂ surfaces with different coverage were studied by Fourier-transform infrared spectroscopy to monitor the molecule degradation.

The BNCs were designed and produced with a laser ablation cluster source. Their composition and structure were controlled by the ablation laser power applied on the targets. An in-flight composition determination method was developed based on the binomial combination theorem and applied to fine tune the cluster composition prior to their deposition (Chapter 3). These composition analysis methods were validated by analysing the mass spectra of a series of Au_xAg_{1-x} nanoclusters produced from Au_xAg_{1-x} alloy targets with known stoichiometries and the global composition measurement of the deposited nanoclusters by Rutherford backscattering spectrometry. The composition controlled nanoclusters were deposited on various substrates for further detailed property investigations and catalytic studies.

First, the structure of Au_xAg_{1-x} BNCs was studied in details and the cluster formation mechanism was revealed. Au_xAg_{1-x} BNCs were deposited on SiO₂ wafers and carbon TEM grids for height and diameter measurements by atomic force microscopy and scanning transmission electron microscopy, respectively. It was found that the cluster shape remained spherical in Au rich BNCs while Ag rich nanoclusters got flattened due to interaction with the support. The detailed atomic structure of the Au_xAg_{1-x} BNCs from gold rich to silver rich compositions was investigated with highly magnified STEM images and an interesting composition-dependent phase segregated structural arrangement was found. By polar coordinates intensity integration, it was revealed that the minority element is systematically predominant in the core of the nanoclusters and the majority element in the outer shell. The atomic arrangement of the Au and Ag atoms inside the nanoclusters was further supported by an extended X-ray absorption fine structure investigation. The electronic structure of the Au_xAg_{1-x} BNCs determined by X-ray photoelectron spectroscopy measurements demonstrated a charge transfer between Ag and Au atoms. The effect of this charge transfer from Ag to Au is likely stabilizing the Ag enriched core against the galvanic replacement reaction, which explains the

stability of this atomic arrangement. Density functional theory calculations further explained the cluster formation mechanism and the charge transfer between Ag and Au, which determines the formation and the stabilization of the phase segregated structure.

In order to study the synergistic effects in BNCs and the support effect on the catalytic activity, a preliminary investigation of the CO oxidation catalytic activity of phase segregated and fully alloyed $\text{Au}_x\text{Ag}_{1-x}$ nanoclusters produced both by laser ablation cluster source and a matrix assembly cluster source, supported on various supports, were tested in an industrial relevant quartz tube gas flow reactors with controlled gas flow and reaction temperature (Chapter 4). It was found that all $\text{Au}_x\text{Ag}_{1-x}$ nanoclusters were catalytically active and their activity was strongly depending on their compositions and supports. In the case of SiO_2 supported phase segregated $\text{Au}_x\text{Ag}_{1-x}$ nanoclusters, $\text{Au}_{0.9}\text{Ag}_{0.1}$ was the most active sample and their catalytic activity was even enhanced in the second CO oxidation reaction cycle. This might be assigned to a re-arrangement of Au and Ag atoms within the nanoclusters under the reaction gases and the temperature applied on the sample. A support affected catalytic activity of the nanoclusters was also observed and it was found that the catalytic activity of TiO_2 anatase supported $\text{Au}_{0.5}\text{Ag}_{0.5}$ nanoclusters was highly enhanced compared to their counterparts supported on SiO_2 . Further and detailed studies are required to fundamentally understand the dynamics and the mechanism of this phenomenon. Despite the limited amount of nanoclusters the production of CO_2 molecules can be observed. However, CO consumption could not be quantified by the mass spectrometer. In order to upscale the amount of nanoclusters to have a sufficient amount of catalyst for industrial relevant catalysis investigations, MACS was used to produce fully alloyed $\text{Au}_x\text{Ag}_{1-x}$ nanoclusters. 2 micro-gram of MgO supported copper contaminated $\text{Au}_{0.25}\text{Ag}_{0.75}$ sample was shown to reach 100 % conversion rate, highlighting the capability of MACS to upscale the cluster production. Further studies regarding the control of the sputtering time are required to prevent copper contamination and detailed studies of the catalytic activity of the nanoclusters supported on other supports are necessary to design a better catalyst.

A series of $\text{Pt}_x\text{Ni}_{1-x}$ nanoclusters were also produced and their phase segregated structures revealed by STEM. Their formation mechanism also is based on the preferential formation of binary few-atom nanoclusters in the initial growth stage (Chapter 5). The catalytic activity of a series of phase segregated $\text{Pt}_x\text{Ni}_{1-x}$ nanoclusters was investigated in a homebuilt temperature programmed desorption setup under methanol decomposition conditions. $\text{Pt}_x\text{Ni}_{1-x}$ nanoclusters were shown to be stable under methanol dehydrogenation reactions and the catalytic activity of Pt rich nanoclusters were preserved. Furthermore, the CO poisoning effect was substantially reduced by alloying Pt with Ni. DFT calculations confirmed that local charge transfer occurs between Pt and Ni atoms and that the underlying reasons for the reduced CO-Pt interaction strength is the modified d-state electronic structure for Pt atoms with subsurface Ni atoms.

The photocatalytic activity and the surface morphology of Au nanoclusters-modified TiO_2 powder films with different coverage was also investigated (Chapter 6). The photocatalytic activities of 2 ML, 4 ML and 8 ML Au nanoclusters modified TiO_2 powder films were tested under visible light as self-cleaning surface towards stearic acid degradation with FTIR. A coverage dependent photocatalytic activity was found and the 4 ML Au nanoclusters on TiO_2 powder was shown to be an excellent photocatalyst towards stearic acid degradation. It was revealed by scanning electron microscopy that the nanoclusters with 2 ML and 4 ML coverage still remain individual on the powder surface while they aggregate when their coverage reaches 8 ML.

To conclude, an in-flight composition determination method was successfully developed and applied for the production of BNCs. With a combination of electron- and X-ray-based characterization techniques, the detailed structure and the formation mechanism can be revealed. Preliminary investigation of catalytic CO oxidation also provides a direction for future industrial relevant catalytic studies. The homebuilt TPD setup was designed and constructed during the PhD project. This setup has not only been successfully tested, but also showed the capability of studying the catalytic reactions under UHV with very limited amount of nanoclusters present on the oxide surface. The photocatalyst produced by cluster beam deposition was shown to be excellent compared to the equivalent one prepared chemically. It also provides a new direction for designing novel photocatalyst in the future.

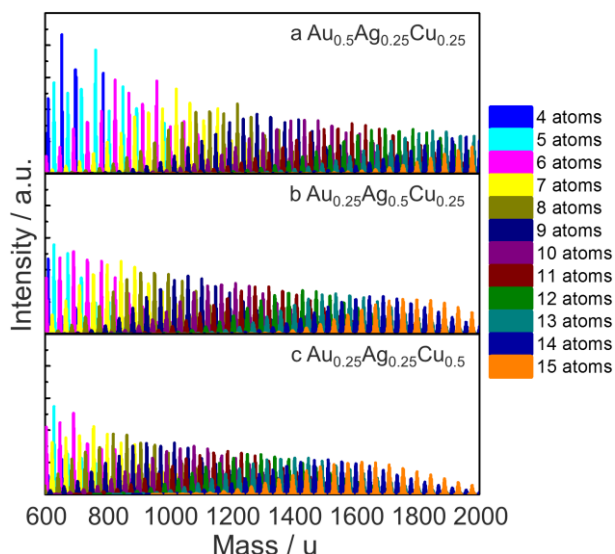


Figure 7.1 Simulated mass spectra within the mass range from 600 u to 2000 u (4 atoms to 15 atoms) of a series Au-Ag-Cu nanoclusters from Au rich $\text{Au}_{0.5}\text{Ag}_{0.25}\text{Cu}_{0.25}$ (a), Ag rich $\text{Au}_{0.25}\text{Ag}_{0.5}\text{Cu}_{0.25}$ (b) and Cu rich $\text{Au}_{0.25}\text{Ag}_{0.25}\text{Cu}_{0.5}$.

Further investigations of composition controlled nanoclusters can be based on the results presented in this PhD thesis. The described RToF mass spectra analysis method based on binomial combinatorial calculations opens up opportunities for controlled production of various types of BNCs with high flexibility. It can be a useful tool to produce BNCs with atomic precision for fundamental investigation. On top of that, this method also can be generalized to the production of trimetallic or multimetallic nanoclusters. A series of simulated mass spectra of Au-Ag-Cu trimetallic nanoclusters (TNCs) from 600 u to 2000 u is presented in Figure 7.1. These generated mass spectra with different compositions and different sizes can be used to fit the experimental spectra and extract the composition of the TNC in the cluster beams prior to deposition.

Great interest in the production of trimetallic nanoparticles from chemical methods was developed in the low temperature fuel cell community. Pt-Fe-Ni,²³¹ Pt-Cu-Ni,²³² Pd-Ni-Pt,²³³ Au-Cu-Pt,²³⁴ Au-Pd-Pt²³⁵ and Ag-Pd-Pt²³⁶ TNPs are synthesized and characterized. The atomic arrangements of these TNPs were revealed by STEM, energy-dispersive X-ray spectroscopy (EDX) and XAS. The electrocatalytic activity of Pd-Ni-Pt and Au-Pd-Pt TNPs were highly enhanced for the oxidation of methanol.^{233, 235} Enhanced oxygen reduction reaction activity and durability were observed on PtFeNi and Pt-Cu-Ni TNPs.²³¹⁻²³² Therefore, TNCs produced by cluster beam deposition methods with precise composition control may contribute to improving low temperature fuel cell performance. Furthermore, from the application point of view, MACS provides high flux cluster beam that can be used to produce sufficient amount of catalyst that can be deposited on oxide support and electrodes of fuel cells in a short time frame for manifold applications such as exhaust pollutants removal, fuel cell activity enhancement as well life time prolongation and self-cleaning surface efficiency enhancement. The methodology that was utilized in this thesis can be further applied for investigating the properties of BNCs and TNCs.

Concerning fundamental investigations of catalytic properties, the constructed TPD setup is suitable for investigating the chemical properties of BNCs and TNCs with only a small quantity of clusters available on the sample surface. Any kind of gases can easily be introduced into the system for studying various types of reactions. Furthermore, the gas line of the TPD setup can be easily integrated with industrial relevant gas flow reactors. In fact, the exhaust gas of gas flow reactors can be introduced into the TPD chamber and analysed by the QMS mass analyser. Therefore, this setup is well able to bridge model catalysts investigations with industrial relevant catalyst studies.

Bibliography

1. Liu, N.; Nittler, L. R.; Alexander, C. M. O.; Wang, J. H. Late Formation of Silicon Carbide in Type II Supernovae. *Sci. Adv.* **2018**, *4*.
2. Li, A.; Draine, B. T. Are Silicon Nanoparticles an Interstellar Dust Component? *Astrophys. J.* **2002**, *564*, 803-812.
3. Jones, A. P.; Nuth, J. A. Dust Destruction in the ISM: A Re-Evaluation of Dust Lifetimes. *Astron. Astrophys.* **2011**, *530*.
4. Henning, T.; Mutschke, H. Low-Temperature Infrared Properties of Cosmic Dust Analogues. *Astron. Astrophys.* **1997**, *327*, 743-754.
5. Narayanan, K. B.; Sakthivel, N. Biological Synthesis of Metal Nanoparticles by Microbes. *Adv. Colloid Interface Sci.* **2010**, *156*, 1-13.
6. Handy, R. D.; Owen, R.; Valsami-Jones, E. The Ecotoxicology of Nanoparticles and Nanomaterials: Current Status, Knowledge Gaps, Challenges, and Future Needs. *Ecotoxicology* **2008**, *17*, 315-325.
7. Strambeanu, N.; Demetrovici, L.; Dragos, D., Natural Sources of Nanoparticles. In *Nanoparticles' Promises and Risks: Characterization, Manipulation, and Potential Hazards to Humanity and the Environment*, Lungu, M.; Neculae, A.; Bunoiu, M.; Biris, C., Eds. Springer International Publishing: Cham, 2015; pp 9-19.
8. Heiligtag, F. J.; Niederberger, M. The Fascinating World of Nanoparticle Research. *Mater. Today* **2013**, *16*, 262-271.
9. Sciau, P. Nanoparticles in Ancient Materials: The Metallic Lustre Decorations of Medieval Ceramics. *Delivery Nanopart.* **2012**, *525-540*.
10. Feynman, R. P. There's Plenty of Room at the Bottom. *Eng. Sci.* **1960**, *23*, 22-36.
11. Knoll, M.; Ruska, E. Das Elektronenmikroskop. *Z. Phys.* **1932**, *78*, 318-339.
12. Binnig, G.; Rohrer, H. Scanning Tunneling Microscopy. *IBM J. Res. Dev.* **1986**, *30*, 355-369.
13. Zhang, H. J.; Watanabe, T.; Okumura, M.; Haruta, M.; Toshima, N. Catalytically Highly Active Top Gold Atom on Palladium Nanocluster. *Nat. Mater.* **2012**, *11*, 49-52.
14. Wang, D.; Villa, A.; Porta, F.; Prati, L.; Su, D. S. Bimetallic Gold/Palladium Catalysts: Correlation between Nanostructure and Synergistic Effects. *J. Phys. Chem. C* **2008**, *112*, 8617-8622.
15. Jiang, H. L.; Akita, T.; Ishida, T.; Haruta, M.; Xu, Q. Synergistic Catalysis of Au@Ag Core-Shell Nanoparticles Stabilized on Metal-Organic Framework. *J. Am. Chem. Soc.* **2011**, *133*, 1304-1306.
16. Sharma, V. K.; Yngard, R. A.; Lin, Y. Silver Nanoparticles: Green Synthesis and Their Antimicrobial Activities. *Adv. Colloid Interface Sci.* **2009**, *145*, 83-96.

17. Huttel, Y. *Gas-Phase Synthesis of Nanoparticles*. John Wiley & Sons: 2017.
18. Rousset, J. L.; Cadrot, A. M.; Aires, F. J. C. S.; Renouprez, A.; Melinon, P.; Perez, A.; Pellarin, M.; Vialle, J. L.; Broyer, M. Study of Bimetallic Pd-Pt Clusters in Both Free and Supported Phases. *J. Chem. Phys.* **1995**, *102*, 8574-8585.
19. Shayeghi, A.; Heard, C. J.; Johnston, R. L.; Schafer, R. Optical and Electronic Properties of Mixed Ag-Au Tetramer Cations. *J. Chem. Phys.* **2014**, *140*.
20. Wagner, R. L.; Vann, W. D.; Castleman, A. W. A Technique for Efficiently Generating Bimetallic Clusters. *Rev. Sci. Instrum.* **1997**, *68*, 3010-3013.
21. Bouwen, W.; Thoen, P.; Vanhoutte, F.; Bouckaert, S.; Despa, F.; Weidele, H.; Silverans, R. E.; Lievens, P. Production of Bimetallic Clusters by a Dual-Target Dual-Laser Vaporization Source. *Rev. Sci. Instrum.* **2000**, *71*, 54-58.
22. Liao, T.-W.; Yadav, A.; Hu, K.-J.; van der Tol, J.; Cosentino, S.; D'Acapito, F.; Palmer, R. E.; Lenardi, C.; Ferrando, R.; Grandjean, D., et al. Unravelling the Nucleation Mechanism of Bimetallic Nanoparticles with Composition-Tunable Core-Shell Arrangement. *Nanoscale* **2018**, *10*, 6684-6694.
23. Pauwels, B.; Van Tendeloo, G.; Zhurkin, E.; Hou, M.; Verschoren, G.; Kuhn, L. T.; Bouwen, W.; Lievens, P. Transmission Electron Microscopy and Monte Carlo Simulations of Ordering in Au-Cu Clusters Produced in a Laser Vaporization Source. *Phys. Rev. B* **2001**, *63*, 165406.
24. Milani, P.; Iannotta, S. *Cluster Beam Synthesis of Nanostructured Materials*. Springer Science & Business Media: 2012.
25. Krishnan, G.; Verheijen, M. A.; ten Brink, G. H.; Palasantzas, G.; Kooi, B. J. Tuning Structural Motifs and Alloying of Bulk Immiscible Mo-Cu Bimetallic Nanoparticles by Gas-Phase Synthesis. *Nanoscale* **2013**, *5*, 5375-5383.
26. Krishnan, G.; Negrea, R. F.; Ghica, C.; ten Brink, G. H.; Kooi, B. J.; Palasantzas, G. Synthesis and Exceptional Thermal Stability of Mg-Based Bimetallic Nanoparticles During Hydrogenation. *Nanoscale* **2014**, *6*, 11963-11970.
27. Grammatikopoulos, P.; Kioseoglou, J.; Galea, A.; Vernieres, J.; Benelmekki, M.; Diaz, R. E.; Sowwan, M. Kinetic Trapping through Coalescence and the Formation of Patterned Ag-Cu Nanoparticles. *Nanoscale* **2016**, *8*, 9780-9790.
28. Johnson, G. E.; Colby, R.; Laskin, J. Soft Landing of Bare Nanoparticles with Controlled Size, Composition, and Morphology. *Nanoscale* **2015**, *7*, 3491-3503.
29. Singh, V.; Cassidy, C.; Grammatikopoulos, P.; Djurabekova, F.; Nordlund, K.; Sowwan, M. Heterogeneous Gas-Phase Synthesis and Molecular Dynamics Modeling of Janus and Core-Satellite Si-Ag Nanoparticles. *J. Phys. Chem. C* **2014**, *118*, 13869-13875.
30. Yasumatsu, H. Generation of Intense and Cold Beam of Pt-Ag Bi-Element Cluster Ions Having Single-Composition. *Eur. Phys. J. D* **2011**, *63*, 195-200.
31. Llamasa, D.; Ruano, M.; Martinez, L.; Mayoral, A.; Roman, E.; Garcia-Hernandez, M.; Huttel, Y. The Ultimate Step Towards a Tailored Engineering of Core@Shell and Core@Shell@Shell Nanoparticles. *Nanoscale* **2014**, *6*, 13483-13486.

32. Li, Z.; Wilcoxon, J.; Yin, F.; Chen, Y.; Palmer, R.; Johnston, R. Structures and Optical Properties of 4–5 nm Bimetallic AgAu Nanoparticles. *Faraday Discuss.* **2008**, *138*, 363-373.
33. Wang, A. Q.; Liu, J. H.; Lin, S. D.; Lin, T. S.; Mou, C. Y. A Novel Efficient Au-Ag Alloy Catalyst System: Preparation, Activity, and Characterization. *J. Catal.* **2005**, *233*, 186-197.
34. Haldar, K. K.; Kundu, S.; Patra, A. Core-Size-Dependent Catalytic Properties of Bimetallic Au/Ag Core-Shell Nanoparticles. *ACS Appl. Mater. Interfaces* **2014**, *6*, 21946-21953.
35. Haruta, M. Size- and Support-Dependency in the Catalysis of Gold. *Catal. Today* **1997**, *36*, 153-166.
36. Lee, S.; Fan, C. Y.; Wu, T. P.; Anderson, S. L. Cluster Size Effects on CO Oxidation Activity, Adsorbate Affinity, and Temporal Behavior of Model Au_n/TiO₂ Catalysts. *J. Chem. Phys.* **2005**, *123*.
37. Arenz, M.; Landman, U.; Heiz, U. CO Combustion on Supported Gold Clusters. *Chemphyschem* **2006**, *7*, 1871-1879.
38. Kaden, W. E.; Wu, T. P.; Kunkel, W. A.; Anderson, S. L. Electronic Structure Controls Reactivity of Size-Selected Pd Clusters Adsorbed on TiO₂ Surfaces. *Science* **2009**, *326*, 826-829.
39. Bonanni, S.; Ait-Mansour, K.; Harbich, W.; Brune, H. Effect of the TiO₂ Reduction State on the Catalytic CO Oxidation on Deposited Size-Selected Pt Clusters. *J. Am. Chem. Soc.* **2012**, *134*, 3445-3450.
40. Liu, X. Y.; Wang, A. Q.; Zhang, T.; Su, D. S.; Mou, C. Y. Au-Cu Alloy Nanoparticles Supported on Silica Gel as Catalyst for CO Oxidation: Effects of Au/Cu Ratios. *Catal. Today* **2011**, *160*, 103-108.
41. Yen, C. W.; Lin, M. L.; Wang, A. Q.; Chen, S. A.; Chen, J. M.; Mou, C. Y. CO Oxidation Catalyzed by Au-Ag Bimetallic Nanoparticles Supported in Mesoporous Silica. *J. Phys. Chem. C* **2009**, *113*, 17831-17839.
42. Hakkinen, H.; Abbet, W.; Sanchez, A.; Heiz, U.; Landman, U. Structural, Electronic, and Impurity-Doping Effects in Nanoscale Chemistry: Supported Gold Nanoclusters. *Angew. Chem., Int. Ed.* **2003**, *42*, 1297-1300.
43. Sharafutdinov, I.; Elkjaer, C. F.; de Carvalho, H. W. P.; Gardini, D.; Chiarello, G. L.; Damsgaard, C. D.; Wagner, J. B.; Grunwaldt, J. D.; Dahl, S.; Chorkendorff, I. Intermetallic Compounds of Ni and Ga as Catalysts for the Synthesis of Methanol. *J. Catal.* **2014**, *320*, 77-88.
44. Hoffmann, M. R.; Martin, S. T.; Choi, W. Y.; Bahnemann, D. W. Environmental Applications of Semiconductor Photocatalysis. *Chem. Rev.* **1995**, *95*, 69-96.
45. Li, J. T.; Wu, N. Q. Semiconductor-Based Photocatalysts and Photoelectrochemical Cells for Solar Fuel Generation: A Review. *Catal. Sci. Technol.* **2015**, *5*, 1360-1384.

46. Ni, M.; Leung, M. K. H.; Leung, D. Y. C.; Sumathy, K. A Review and Recent Developments in Photocatalytic Water-Splitting Using TiO₂ for Hydrogen Production. *Renew. Sust. Energ. Rev.* **2007**, *11*, 401-425.
47. Hashimoto, K.; Irie, H.; Fujishima, A. TiO₂ Photocatalysis: A Historical Overview and Future Prospects. *Jpn. J. Appl. Phys., Part 1* **2005**, *44*, 8269-8285.
48. Sugano, Y.; Shiraishi, Y.; Tsukamoto, D.; Ichikawa, S.; Tanaka, S.; Hirai, T. Supported Au-Cu Bimetallic Alloy Nanoparticles: An Aerobic Oxidation Catalyst with Regenerable Activity by Visible-Light Irradiation. *Angew. Chem., Int. Ed.* **2013**, *52*, 5295-5299.
49. Su, R.; Tiruvalam, R.; Logsdail, A. J.; He, Q.; Downing, C. A.; Jensen, M. T.; Dimitratos, N.; Kesavan, L.; Wells, P. P.; Bechstein, R., et al. Designer Titania-Supported Au-Pd Nanoparticles for Efficient Photocatalytic Hydrogen Production. *ACS Nano* **2014**, *8*, 3490-3497.
50. Dobrynin, A. N.; Ievlev, D. N.; Verschoren, G.; Swerts, J.; Van Bael, M. J.; Temst, K.; Lievens, P.; Piscopiello, E.; Van Tendeloo, G.; Zhou, S. Q., et al. Atomic-Scale Modification of Hybrid FePt Cluster-Assembled Films. *Phys. Rev. B* **2006**, *73*.
51. Verschoren, G.; Dobrynin, A. N.; Temst, K.; Silverans, R. E.; Van Haesendonck, C.; Lievens, P.; Pipeleers, B.; Zhou, S. Q.; Vantomme, A.; Bras, W. Electron Scattering in Au Films Containing Co Clusters. *Thin Solid Films* **2008**, *516*, 8232-8239.
52. Li, Z.; Chen, H. Y. T.; Schouteden, K.; Picot, T.; Houben, K.; Liao, T. W.; Van Haesendonck, C.; Pacchioni, G.; Lievens, P.; Janssens, E. Size-Dependent Penetration of Gold Nanoclusters through a Defect-Free, Nonporous NaCl Membrane. *Nano Lett.* **2016**, *16*, 3063-3070.
53. Scheerder, J. E.; Picot, T.; Reckinger, N.; Sneyder, T.; Zharinov, V. S.; Colomer, J. F.; Janssens, E.; Van de Vondel, J. Decorating Graphene with Size-Selected Few-Atom Clusters: A Novel Approach to Investigate Graphene-Adparticle Interactions. *Nanoscale* **2017**, *9*, 10494-10501.
54. Li, Z.; Chen, H. Y. T.; Schouteden, K.; Picot, T.; Hillion, A.; Pacchioni, G.; Van Haesendonck, C.; Janssens, E.; Lievens, P. Size-Dependent Dissociation of Small Cobalt Clusters on Ultrathin NaCl Films. *Nano. Res.* **2017**, *10*, 1832-1839.
55. Zhao, J. L.; Cao, L.; Palmer, R. E.; Nordlund, K.; Djurabekova, F. Formation and Emission Mechanisms of Ag Nanoclusters in the Ar Matrix Assembly Cluster Source. *Phy. Rev. Mater.* **2017**, *1*.
56. Palmer, R. E.; Cao, L.; Yin, F. Note: Proof of Principle of a New Type of Cluster Beam Source with Potential for Scale-Up. *Rev. Sci. Instrum.* **2016**, *87*, 046103.
57. Ellis, P. R.; Brown, C. M.; Bishop, P. T.; Yin, J.; Cooke, K.; Terry, W. D.; Liu, J.; Yin, F.; Palmer, R. E. The Cluster Beam Route to Model Catalysts and Beyond. *Faraday Discuss.* **2016**.
58. Pauly, H., Fundamental Principles of Gas Dynamics. In *Atom, Molecule, and Cluster Beams I: Basic Theory, Production and Detection of Thermal Energy Beams*, Springer Berlin Heidelberg: Berlin, Heidelberg, 2000; pp 77-146.

59. Ferrari, P.; Vanbuel, J.; Li, Y.; Liao, T.-W.; Janssens, E.; Lievens, P., The Double-Laser Ablation Source Approach. In *Gas-Phase Synthesis of Nanoparticles*, Wiley-VCH Verlag GmbH & Co. KGaA: Weinheim, Germany, 2017; pp 59-78.
60. Goldby, I. M.; vonIssendorff, B.; Kuipers, L.; Palmer, R. E. Gas Condensation Source for Production and Deposition of Size-Selected Metal Clusters. *Rev. Sci. Instrum.* **1997**, *68*, 3327-3334.
61. Pratontep, S.; Carroll, S. J.; Xirouchaki, C.; Streun, M.; Palmer, R. E. Size-Selected Cluster Beam Source Based on Radio Frequency Magnetron Plasma Sputtering and Gas Condensation. *Rev. Sci. Instrum.* **2005**, *76*.
62. Hartmann, H.; Popok, V. N.; Barke, I.; Von Oeynhausen, V.; Meiwes-Broer, K. H. Design and Capabilities of an Experimental Setup Based on Magnetron Sputtering for Formation and Deposition of Size-Selected Metal Clusters on Ultra-Clean Surfaces. *Rev. Sci. Instrum.* **2012**, *83*.
63. Haberland, H.; Mall, M.; Moseler, M.; Qiang, Y.; Reiners, T.; Thurner, Y. Filling of Micron-Sized Contact Holes with Copper by Energetic Cluster-Impact. *Journal of Vacuum Science & Technology A* **1994**, *12*, 2925-2930.
64. Oiko, V. T.; Mathieu, T.; Cao, L.; Liu, J.; Palmer, R. E. Note: Production of Silver Nanoclusters Using a Matrix-Assembly Cluster Source with a Solid CO₂ Matrix. *J. Chem. Phys.* **2016**, *145*, 166101.
65. Mamyrin, B.; Karataev, V.; Shmikk, D.; Zagulin, V. The Mass-Reflectron, a New Non-Magnetic Time-of-Flight Mass Spectrometer with High Resolution. *Zh. Eksp. Teor. Fiz* **1973**, *64*, 82-89.
66. Bergmann, T.; Martin, T. P.; Schaber, H. High-Resolution Time-of-Flight Mass-Spectrometer. *Rev. Sci. Instrum.* **1989**, *60*, 792-793.
67. Perriere, J. Rutherford Backscattering Spectrometry. *Vacuum* **1987**, *37*, 429-432.
68. Cosslett, V. E. Scanning Electron-Microscopy - Physics of Image-Formation and Microanalysis - Reimer, L. *Nature* **1986**, *323*, 212-212.
69. Hartel, P.; Rose, H.; Dinges, C. Conditions and Reasons for Incoherent Imaging in STEM. *Ultramicroscopy* **1996**, *63*, 93-114.
70. Wang, Z. W.; Li, Z. Y.; Park, S. J.; Abdela, A.; Tang, D.; Palmer, R. E. Quantitative Z-Contrast Imaging in the Scanning Transmission Electron Microscope with Size-Selected Clusters. *Phys. Rev. B* **2011**, *84*.
71. Young, N. P.; Li, Z. Y.; Chen, Y.; Palomba, S.; Di Vece, M.; Palmer, R. E. Weighing Supported Nanoparticles: Size-Selected Clusters as Mass Standards in Nanometrology. *Phys. Rev. Lett.* **2008**, *101*.
72. McCash, E. M. *Surface Chemistry*. Oxford University Press: Oxford, 2001.
73. Newville, M. Fundamentals of Xafs. *Rev. Mineral. Geochem.* **2014**, *78*, 33-74.
74. Penner-Hahn, J. E. X-Ray Absorption Spectroscopy. *eLS* **2005**.

75. Hummer, A. A.; Rompel, A. X-Ray Absorption Spectroscopy: A Tool to Investigate the Local Structure of Metal-Based Anticancer Compounds in Vivo. *Adv. Protein Chem. Struct. Biol.* **2013**, *93*, 257-305.
76. Marr, G. V. *Handbook on Synchrotron Radiation: Vacuum Ultraviolet and Soft X-Ray Processes*. Elsevier: 2013.
77. Binsted, N.; Campbell, J.; Gurman, S. J.; Stephenson, P. C. EXAFS Analysis Programs; Daresbury Laboratory; Warrington, U.K. *EXAFS analysis Programs; Daresbury Laboratory; Warrington, U.K.* **1991**.
78. Falconer, J. L.; Schwarz, J. A. Temperature-Programmed Desorption and Reaction - Applications to Supported Catalysts. *Catal. Rev.* **1983**, *25*, 141-227.
79. Ferrando, R.; Jellinek, J.; Johnston, R. L. Nanoalloys: From Theory to Applications of Alloy Clusters and Nanoparticles. *Chem. Rev.* **2008**, *108*, 845-910.
80. Johnston, R. L.; Wilcoxon, J. P. *Metal Nanoparticles and Nanoalloys*. Elsevier Science: 2012.
81. Cha, S. K.; Mun, J. H.; Chang, T.; Kim, S. Y.; Kim, J. Y.; Jin, H. M.; Lee, J. Y.; Shin, J.; Kim, K. H.; Kim, S. O. Au-Ag Core-Shell Nanoparticle Array by Block Copolymer Lithography for Synergistic Broadband Plasmonic Properties. *ACS Nano* **2015**, *9*, 5536-5543.
82. Benkó, T.; Beck, A.; Frey, K.; Srankó, D. F.; Geszti, O.; Sáfrán, G.; Maróti, B.; Schay, Z. Bimetallic Ag–Au/SiO₂ Catalysts: Formation, Structure and Synergistic Activity in Glucose Oxidation. *Applied Catalysis A: General* **2014**, *479*, 103-111.
83. Sun, S. H.; Murray, C. B.; Weller, D.; Folks, L.; Moser, A. Monodisperse FePt Nanoparticles and Ferromagnetic FePt Nanocrystal Superlattices. *Science* **2000**, *287*, 1989-1992.
84. Kreibig, U.; Vollmer, M. *Optical Properties of Metal Clusters*. Springer Berlin Heidelberg: 2013.
85. Habibpour, V.; Song, M. Y.; Wang, Z. W.; Cookson, J.; Brown, C. M.; Bishop, P. T.; Palmer, R. E. Novel Powder-Supported Size-Selected Clusters for Heterogeneous Catalysis under Realistic Reaction Conditions. *J. Phys. Chem. C* **2012**, *116*, 26295-26299.
86. Jian, N.; Palmer, R. E. Variation of the Core Atomic Structure of Thiolated (Au_xAg_{1-x})(312 +/- 55) Nanoclusters with Composition from Aberration-Corrected HAADF STEM. *J. Phys. Chem. C* **2015**, *119*, 11114-11119.
87. Gomes, J. F.; Garcia, A. C.; Pires, C.; Ferreira, E. B.; Albuquerque, R. Q.; Tremiliosi, G.; Gasparotto, L. H. S. Impact of the AuAg NPs Composition on Their Structure and Properties: A Theoretical and Experimental Investigation. *J. Phys. Chem. C* **2014**, *118*, 28868-28875.
88. Yang, Y.; Liu, J. Y.; Fu, Z. W.; Qin, D. Galvanic Replacement-Free Deposition of Au on Ag for Core-Shell Nanocubes with Enhanced Chemical Stability and SERS Activity. *J. Am. Chem. Soc.* **2014**, *136*, 8153-8156.

89. Hartmann, M. J.; Hakkinen, H.; Millstone, J. E.; Lambrecht, D. S. Impacts of Copper Position on the Electronic Structure of $[\text{Au}_{25-x}\text{Cu}_x(\text{Sh})_{18}]^-$ Nanoclusters. *J. Phys. Chem. C* **2015**, *119*, 8290-8298.
90. Cui, C. H.; Gan, L.; Heggen, M.; Rudi, S.; Strasser, P. Compositional Segregation in Shaped Pt Alloy Nanoparticles and Their Structural Behaviour During Electrocatalysis. *Nat. Mater.* **2013**, *12*, 765-771.
91. Gould, A. L.; Logsdail, A. J.; Catlow, C. R. A. Influence of Composition and Chemical Arrangement on the Kinetic Stability of 147-Atom Au-Ag Bimetallic Nanoclusters. *J. Phys. Chem. C* **2015**, *119*, 23685-23697.
92. Gilroy, K. D.; Ruditskiy, A.; Peng, H. C.; Qin, D.; Xia, Y. N. Bimetallic Nanocrystals: Syntheses, Properties, and Applications. *Chem. Rev.* **2016**, *116*, 10414-10472.
93. Chaudhuri, R. G.; Paria, S. Core/Shell Nanoparticles: Classes, Properties, Synthesis Mechanisms, Characterization, and Applications. *Chem. Rev.* **2012**, *112*, 2373-2433.
94. Marbella, L. E.; Chevrier, D. M.; Tancini, P. D.; Shobayo, O.; Smith, A. M.; Johnston, K. A.; Andolina, C. M.; Zhang, P.; Mpourmpakis, G.; Millstone, J. E. Description and Role of Bimetallic Prenucleation Species in the Formation of Small Nanoparticle Alloys. *J. Am. Chem. Soc.* **2015**, *137*, 15852-15858.
95. Finney, E. E.; Finke, R. G. Nanocluster Nucleation and Growth Kinetic and Mechanistic Studies: A Review Emphasizing Transition-Metal Nanoclusters. *J. Colloid Interface Sci.* **2008**, *317*, 351-374.
96. Chen, X. L.; Schroder, J.; Hauschild, S.; Rosenfeldt, S.; Dulle, M.; Forster, S. Simultaneous SAXS/WAXS/UV-VIS Study of the Nucleation and Growth of Nanoparticles: A Test of Classical Nucleation Theory. *Langmuir* **2015**, *31*, 11678-11691.
97. Wuithschick, M.; Witte, S.; Kettemann, F.; Rademann, K.; Polte, J. Illustrating the Formation of Metal Nanoparticles with a Growth Concept Based on Colloidal Stability. *Phys. Chem. Chem. Phys.* **2015**, *17*, 19895-19900.
98. Wang, F. D.; Richards, V. N.; Shields, S. P.; Buhro, W. E. Kinetics and Mechanisms of Aggregative Nanocrystal Growth. *Chem. Mater.* **2014**, *26*, 5-21.
99. Popok, V. N.; Barke, I.; Campbell, E. E. B.; Meiwes-Broer, K. H. Cluster-Surface Interaction: From Soft Landing to Implantation. *Surf. Sci. Rep.* **2011**, *66*, 347-377.
100. Herbani, Y.; Nakamura, T.; Sato, S. Synthesis of near-Monodispersed Au-Ag Nanoalloys by High Intensity Laser Irradiation of Metal Ions in Hexane. *J. Phys. Chem. C* **2011**, *115*, 21592-21598.
101. Chen, H.; Liu, R.; Jang, L.-Y.; Lee, J.-F.; Hu, S. Characterization of Core-Shell Type and Alloy Ag/Au Bimetallic Clusters by Using Extended X-Ray Absorption Fine Structure Spectroscopy. *Chem. Phys. Lett.* **2006**, *421*, 118-123.
102. Ristig, S.; Prymak, O.; Loza, K.; Gocyla, M.; Meyer-Zaika, W.; Heggen, M.; Raabe, D.; Epple, M. Nanostructure of Wet-Chemically Prepared, Polymer-Stabilized

Silver-Gold Nanoalloys (6 nm) over the Entire Composition Range. *J. Mater. Chem. B* **2015**, *3*, 4654-4662.

103. Liao, T.-W.; Verbruggen, S. W.; Claes, N.; Yadav, A.; Grandjean, D.; Bals, S.; Lievens, P. TiO₂ Films Modified with Au Nanoclusters as Self-Cleaning Surfaces under Visible Light. *Nanomaterials* **2018**, *8*, 30.

104. Sasirekha, N.; Sangeetha, P.; Chen, Y.-W. Bimetallic Au–Ag/CeO₂ Catalysts for Preferential Oxidation of CO in Hydrogen-Rich Stream: Effect of Calcination Temperature. *J. Phys. Chem. C* **2014**, *118*, 15226-15233.

105. Liu, J.-H.; Wang, A.-Q.; Chi, Y.-S.; Lin, H.-P.; Mou, C.-Y. Synergistic Effect in an Au-Ag Alloy Nanocatalyst: CO Oxidation. *J. Phys. Chem. B* **2005**, *109*, 40-43.

106. Sarina, S.; Zhu, H. Y.; Xiao, Q.; Jaatinen, E.; Jia, J. F.; Huang, Y. M.; Zheng, Z. F.; Wu, H. S. Viable Photocatalysts under Solar-Spectrum Irradiation: Nonplasmonic Metal Nanoparticles. *Angew. Chem., Int. Ed.* **2014**, *53*, 2935-2940.

107. Xiao, Q.; Sarina, S.; Waclawik, E. R.; Jia, J. F.; Chang, J.; Riches, J. D.; Wu, H. S.; Zheng, Z. F.; Zhu, H. Y. Alloying Gold with Copper Makes for a Highly Selective Visible-Light Photocatalyst for the Reduction of Nitroaromatics to Anilines. *ACS Catal.* **2016**, *6*, 1744-1753.

108. Wang, J. L.; Ando, R. A.; Camargo, P. H. C. Investigating the Plasmon-Mediated Catalytic Activity of AgAu Nanoparticles as a Function of Composition: Are Two Metals Better Than One? *ACS Catal.* **2014**, *4*, 3815-3819.

109. Kim, W. J.; Kim, S.; Kim, A. R.; Yoo, D. J. Direct Detection System for Escherichia Coli Using Au-Ag Alloy Microchips. *Ind. Eng. Chem. Res.* **2013**, *52*, 7282-7288.

110. Hu, B.; Wang, N.; Han, L.; Chen, M. L.; Wang, J. H. Core-Shell-Shell Nanorods for Controlled Release of Silver That Can Serve as a Nanoheater for Photothermal Treatment on Bacteria. *Acta Biomater.* **2015**, *11*, 511-519.

111. Chernousova, S.; Epple, M. Silver as Antibacterial Agent: Ion, Nanoparticle, and Metal. *Angew. Chem., Int. Ed.* **2013**, *52*, 1636-1653.

112. Dreaden, E. C.; Alkilany, A. M.; Huang, X. H.; Murphy, C. J.; El-Sayed, M. A. The Golden Age: Gold Nanoparticles for Biomedicine. *Chem. Soc. Rev.* **2012**, *41*, 2740-2779.

113. Hellenbrandt, M. The Inorganic Crystal Structure Database (ICSD)—Present and Future. *Crystallogr. Rev.* **2004**, *10*, 17-22.

114. Hannemann, S.; Grunwaldt, J. D.; Krumeich, F.; Kappen, P.; Baiker, A. Electron Microscopy and EXAFS Studies on Oxide-Supported Gold-Silver Nanoparticles Prepared by Flame Spray Pyrolysis. *Appl. Surf. Sci.* **2006**, *252*, 7862-7873.

115. Li, Z. Y.; Yuan, J.; Chen, Y.; Palmer, R. E.; Wilcoxon, J. P. Direct Imaging of Core-Shell Structure in Silver-Gold Bimetallic Nanoparticles. *Appl. Phys. Lett.* **2005**, *87*, 243103.

116. Godfrey, I. J.; Dent, A. J.; Parkin, I. P.; Maenosono, S.; Sankar, G. Structure of Gold-Silver Nanoparticles. *J. Phys. Chem. C* **2017**, *121*, 1957-1963.
117. Chimentao, R. J.; Cota, I.; Dafinov, A.; Medina, F.; Sueiras, J. E.; de la Fuente, J. L. G.; Fierro, J. L. G.; Cesteros, Y.; Salagre, P. Synthesis of Silver-Gold Alloy Nanoparticles by a Phase-Transfer System. *J. Mater. Res.* **2006**, *21*, 105-111.
118. Chang, C. M.; Cheng, C.; Wei, C. M. CO Oxidation on Unsupported Au₅₅, Ag₅₅, and Au₂₅Ag₃₀ Nanoclusters. *J. Chem. Phys.* **2008**, *128*.
119. Vandamme, N.; Janssens, E.; Vanhoutte, F.; Lievens, P.; Van Haesendonck, C. Scanning Probe Microscopy Investigation of Gold Clusters Deposited on Atomically Flat Substrates. *J. Phys.: Condens. Matter* **2003**, *15*, S2983-S2999.
120. Wang, Z.; Palmer, R. Intensity Calibration and Atomic Imaging of Size-Selected Au and Pd Clusters in Aberration-Corrected HAADF-STEM. *J. Phys.: Conf. Ser.* **2012**, *371*, 012010.
121. Schindelin, J.; Arganda-Carreras, I.; Frise, E.; Kaynig, V.; Longair, M.; Pietzsch, T.; Preibisch, S.; Rueden, C.; Saalfeld, S.; Schmid, B., et al. Fiji: An Open-Source Platform for Biological-Image Analysis. *Nat. Methods* **2012**, *9*, 676-682.
122. Giannozzi, P.; Baroni, S.; Bonini, N.; Calandra, M.; Car, R.; Cavazzoni, C.; Ceresoli, D.; Chiarotti, G. L.; Cococcioni, M.; Dabo, I., et al. Quantum Espresso: A Modular and Open-Source Software Project for Quantum Simulations of Materials. *J. Phys.: Condens. Matter* **2009**, *21*.
123. Vanderbilt, D. Soft Self-Consistent Pseudopotentials in a Generalized Eigenvalue Formalism. *Phys. Rev. B* **1990**, *41*, 7892-7895.
124. Perdew, J. P.; Burke, K.; Ernzerhof, M. Generalized Gradient Approximation Made Simple. *Phys. Rev. Lett.* **1996**, *77*, 3865-3868.
125. He, H.; Li, Y.; Zhang, X. L.; Yu, Y. B.; Zhang, C. B. Precipitable Silver Compound Catalysts for the Selective Catalytic Reduction of NO_x by Ethanol. *Appl. Catal., A* **2010**, *375*, 258-264.
126. Kannisto, H.; Ingelsten, H. H.; Skoglundh, M. Ag-Al₂O₃ Catalysts for Lean NO_x Reduction-Influence of Preparation Method and Reductant. *J. Mol. Catal. A: Chem.* **2009**, *302*, 86-96.
127. Dao, T. N. A.; Singh, P.; Shankar, C.; Mott, D.; Maenosono, S. Charge-Transfer-Induced Suppression of Galvanic Replacement and Synthesis of (Au@Ag)@Au Double Shell Nanoparticles for Highly Uniform, Robust and Sensitive Bioprobes. *Appl. Phys. Lett.* **2011**, *99*.
128. Chen, T.; Yang, S.; Chai, J. S.; Song, Y. B.; Fan, J. Q.; Rao, B.; Sheng, H. T.; Yu, H. Z.; Zhu, M. Z. Crystallization-Induced Emission Enhancement: A Novel Fluorescent Au-Ag Bimetallic Nanocluster with Precise Atomic Structure. *Sci. Adv.* **2017**, *3*.
129. Shankar, C.; Dao, A. T. N.; Singh, P.; Higashimine, K.; Mott, D. M.; Maenosono, S. Chemical Stabilization of Gold Coated by Silver Core-Shell Nanoparticles Via Electron Transfer. *Nanotechnology* **2012**, *23*.

130. Nishimura, S.; Anh, D. T. N.; Mott, D.; Ebitani, K.; Maenosono, S. Spectroscopic Study on the Charge Redistribution between Au and Ag in Au@Ag Core-Shell Nanoparticles. *Nanotechnology 2012, Vol 1: Advanced Materials, Cnts, Particles, Films and Composites* **2012**, 38-41.
131. Miller, J. T.; Kropf, A. J.; Zha, Y.; Regalbuto, J. R.; Delannoy, L.; Louis, C.; Bus, E.; van Bokhoven, J. A. The Effect of Gold Particle Size on Au-Au Bond Length and Reactivity toward Oxygen in Supported Catalysts. *J. Catal.* **2006**, *240*, 222-234.
132. Sun, Y.; Frenkel, A. I.; White, H.; Zhang, L. H.; Zhu, Y. M.; Xu, H. P.; Yang, J. C.; Koga, T.; Zaitsev, V.; Rafailovich, M. H., et al. Comparison of Decanethiolate Gold Nanoparticles Synthesized by One-Phase and Two-Phase Methods. *J. Phys. Chem. B* **2006**, *110*, 23022-23030.
133. Huang, W. J.; Sun, R.; Tao, J.; Menard, L. D.; Nuzzo, R. G.; Zuo, J. M. Coordination-Dependent Surface Atomic Contraction in Nanocrystals Revealed by Coherent Diffraction. *Nat. Mater.* **2008**, *7*, 308-313.
134. Knauer, W. Formation of Large Metal Clusters by Surface Nucleation. *J. Appl. Phys.* **1987**, *62*, 841-851.
135. Ayesh, A. I.; Qamhieh, N.; Mahmoud, S. T.; Alawadhi, H. Fabrication of Size-Selected Bimetallic Nanoclusters Using Magnetron Sputtering. *J. Mater. Res.* **2012**, *27*, 2441-2446.
136. Scoles, G.; Bassi, D.; Buck, U. Atomic and Molecular Beam Methods. Oxford university press New York: 1988.
137. Hihara, T.; Sumiyama, K. Formation and Size Control of a Ni Cluster by Plasma Gas Condensation. *J. Appl. Phys.* **1998**, *84*, 5270-5276.
138. Ferrando, R., Chapter 5 - Equilibrium Structures of Nanoalloys. In *Frontiers of Nanoscience*, Riccardo, F., Ed. Elsevier: 2016; Vol. Volume 10, pp 131-183.
139. Aslan, M.; Davis, J. B. A.; Johnston, R. L. Global Optimization of Small Bimetallic Pd-Co Binary Nanoalloy Clusters: A Genetic Algorithm Approach at the DFT Level. *Phys. Chem. Chem. Phys.* **2016**, *18*, 6676-6682.
140. Pittaway, F.; Paz-Borbon, L. O.; Johnston, R. L.; Arslan, H.; Ferrando, R.; Mottet, C.; Barcaro, G.; Fortunelli, A. Theoretical Studies of Palladium-Gold Nanoclusters: Pd-Au Clusters with up to 50 Atoms. *J. Phys. Chem. C* **2009**, *113*, 9141-9152.
141. Molayem, M.; Grigoryan, V. G.; Springborg, M. Global Minimum Structures and Magic Clusters of Cu_mAg_n Nanoalloys. *J. Phys. Chem. C* **2011**, *115*, 22148-22162.
142. Molayem, M.; Grigoryan, V. G.; Springborg, M. Theoretical Determination of the Most Stable Structures of Ni-magn Bimetallic Nanoalloys. *J. Phys. Chem. C* **2011**, *115*, 7179-7192.
143. Wegner, K.; Piseri, P.; Tafreshi, H. V.; Milani, P. Cluster Beam Deposition: A Tool for Nanoscale Science and Technology. *J. Phys. D: Appl. Phys.* **2006**, *39*, R439-R459.

144. Polte, J.; Ahner, T. T.; Delissen, F.; Sokolov, S.; Emmerling, F.; Thunemann, A. F.; Kraehnert, R. Mechanism of Gold Nanoparticle Formation in the Classical Citrate Synthesis Method Derived from Coupled in Situ XANES and SAXS Evaluation. *J. Am. Chem. Soc.* **2010**, *132*, 1296-1301.
145. Polte, J.; Erler, R.; Thunemann, A. F.; Sokolov, S.; Ahner, T. T.; Rademann, K.; Emmerling, F.; Kraehnert, R. Nucleation and Growth of Gold Nanoparticles Studied Via in Situ Small Angle X-Ray Scattering at Millisecond Time Resolution. *ACS Nano* **2010**, *4*, 1076-1082.
146. Nunez, S.; Johnston, R. L. Structures and Chemical Ordering of Small Cu-Ag Clusters. *J. Phys. Chem. C* **2010**, *114*, 13255-13266.
147. Parsina, I.; Baletto, F. Tailoring the Structural Motif of AgCo Nanoalloys: Core/Shell Versus Janus-Like. *J. Phys. Chem. C* **2010**, *114*, 1504-1511.
148. Baletto, F., Modelling Janus Nanoparticles. In *Metal Clusters and Nanoalloys: From Modeling to Applications*, Springer New York: New York, NY, 2013; pp 243-273.
149. Gumber, S.; Gurumoorthy, A. V., Methanol Economy Versus Hydrogen Economy. In *Methanol*, Elsevier: 2017; pp 661-674.
150. Olah, G. A. Beyond Oil and Gas: The Methanol Economy. *Angew. Chem., Int. Ed.* **2005**, *44*, 2636-2639.
151. Hung, T. C.; Liao, T. W.; Liao, Z. H.; Hsu, P. W.; Cai, P. Y.; Lee, H.; Lai, Y. L.; Hsu, Y. J.; Chen, H. Y.; Wang, J. H., et al. Dependence on Size of Supported Rh Nanoclusters in the Decomposition of Methanol. *ACS Catal.* **2015**, *5*, 4276-4287.
152. Rostrup-Nielsen, J. R.; Nielsen, R. Fuels and Energy for the Future: The Role of Catalysis. *Catal. Rev.* **2004**, *46*, 247-270.
153. Debe, M. K. Electrocatalyst Approaches and Challenges for Automotive Fuel Cells. *Nature* **2012**, *486*, 43-51.
154. Chao, C. S.; Liao, T. W.; Wang, C. X.; Li, Y. D.; Hung, T. C.; Luo, M. F. Obstruction by CO of the Decomposition of Methanol on Pt Nanoclusters on a Thin Film of Al₂O₃/NiAl(100). *Appl. Surf. Sci.* **2014**, *293*, 352-358.
155. Chao, C. S.; Li, Y. D.; Liao, T. W.; Hung, T. C.; Luo, M. F. Decomposition of Methanol on Partially Alumina-Encapsulated Pt Nanoclusters Supported on Thin Film Al₂O₃/NiAl(100). *Appl. Surf. Sci.* **2014**, *311*, 763-769.
156. Ehteshami, S. M. M.; Chan, S. H. A Review of Electrocatalysts with Enhanced CO Tolerance and Stability for Polymer Electrolyte Membrane Fuel Cells. *Electrochim. Acta* **2013**, *93*, 334-345.
157. Baschuk, J. J.; Li, X. G. Carbon Monoxide Poisoning of Proton Exchange Membrane Fuel Cells. *Int. J. Energ. Res.* **2001**, *25*, 695-713.
158. Liu, J. L.; Lucci, F. R.; Yang, M.; Lee, S.; Marcinkowski, M. D.; Therrien, A. J.; Williams, C. T.; Sykes, E. C. H.; Flytzani-Stephanopoulos, M. Tackling CO Poisoning with Single-Atom Alloy Catalysts. *J. Am. Chem. Soc.* **2016**, *138*, 6396-6399.

159. Kizhakevariam, N.; Stuve, E. M. Promotion and Poisoning of the Reaction of Methanol on Clean and Modified Platinum (100). *Surf. Sci.* **1993**, *286*, 246-260.
160. Kramer, Z. C.; Gu, X. K.; Zhou, D. D. Y.; Li, W. X.; Skodje, R. T. Following Molecules through Reactive Networks: Surface Catalyzed Decomposition of Methanol on Pd(111), Pt(111), and Ni(111). *J. Phys. Chem. C* **2014**, *118*, 12364-12383.
161. Sexton, B. A. Methanol Decomposition on Platinum (111). *Surf. Sci.* **1981**, *102*, 271-281.
162. Stottlemeyer, A. L.; Ren, H.; Chen, J. G. Reactions of Methanol and Ethylene Glycol on Ni/Pt: Bridging the Materials Gap between Single Crystal and Polycrystalline Bimetallic Surfaces. *Surf. Sci.* **2009**, *603*, 2630-2638.
163. Feng, Y. Y.; Bi, L. X.; Liu, Z. H.; Kong, D. S.; Yu, Z. Y. Significantly Enhanced Electrocatalytic Activity for Methanol Electro-Oxidation on Ag Oxide-Promoted PtAg/C Catalysts in Alkaline Electrolyte. *J. Catal.* **2012**, *290*, 18-25.
164. Hu, J. E.; Liu, Z. F.; Eichhorn, B. W.; Jackson, G. S. CO Tolerance of Nano-Architected Pt-Mo Anode Electrocatalysts for PEM Fuel Cells. *Int. J. Hydrogen Energy* **2012**, *37*, 11268-11275.
165. Kim, J. H.; Choi, S. M.; Nam, S. H.; Seo, M. H.; Choi, S. H.; Kim, W. B. Influence of Sn Content on PtSn/C Catalysts for Electrooxidation of C-1-C-3 Alcohols: Synthesis, Characterization, and Electrocatalytic Activity. *Appl. Catal., B* **2008**, *82*, 89-102.
166. Rocha, T. A.; Ibanhi, F.; Colmati, F.; Linares, J. J.; Paganin, V. A.; Gonzalez, E. R. Nb as an Influential Element for Increasing the CO Tolerance of Pemfc Catalysts. *J. Appl. Electrochem.* **2013**, *43*, 817-827.
167. Liao, M. S.; Cabrera, C. R.; Ishikawa, Y. A Theoretical Study of CO Adsorption on Pt, Ru and Pt-M (M = Ru, Sn, Ge) Clusters. *Surf. Sci.* **2000**, *445*, 267-282.
168. Kitchin, J. R.; Norskov, J. K.; Barteau, M. A.; Chen, J. G. Modification of the Surface Electronic and Chemical Properties of Pt(111) by Subsurface 3d Transition Metals. *J. Chem. Phys.* **2004**, *120*, 10240-10246.
169. Norskov, J. K.; Abild-Pedersen, F.; Studt, F.; Bligaard, T. Density Functional Theory in Surface Chemistry and Catalysis. *Proc. Natl. Acad. Sci. U.S.A.* **2011**, *108*, 937-943.
170. Skoplyak, O.; Menning, C. A.; Barteau, M. A.; Chen, J. G. G. Experimental and Theoretical Study of Reactivity Trends for Methanol on Co/Pt(111) and Ni/Pt(111) Bimetallic Surfaces. *J. Chem. Phys.* **2007**, *127*.
171. Garcia-Muelas, R.; Li, Q.; Lopez, N. Density Functional Theory Comparison of Methanol Decomposition and Reverse Reactions on Metal Surfaces. *ACS Catal.* **2015**, *5*, 1027-1036.
172. Guo, W. L.; Tian, W. Q.; Lian, X.; Liu, F. L.; Zhou, M.; Xiao, P.; Zhang, Y. H. A Comparison of the Dominant Pathways for the Methanol Dehydrogenation to CO on Pt₇ and Pt_{7-x}Ni_x (x=1, 2, 3) Bimetallic Clusters: A DFT Study. *Comput. Theor. Chem.* **2014**, *1032*, 73-83.

173. Ferrari, P.; Molina, L. M.; Kaydashev, V. E.; Alonso, J. A.; Lievens, P.; Janssens, E. Controlling the Adsorption of Carbon Monoxide on Platinum Clusters by Dopant-Induced Electronic Structure Modification. *Angew. Chem., Int. Ed.* **2016**, *55*, 11059-11063.
174. Ferrari, P.; Vanbuel, J.; Tam, N. M.; Nguyen, M. T.; Gewinner, S.; Schollkopf, W.; Fielicke, A.; Janssens, E. Effects of Charge Transfer on the Adsorption of CO on Small Molybdenum-Doped Platinum Clusters. *Chem. Eur. J.* **2017**, *23*, 4120-4127.
175. Liang, G. F.; He, L. M.; Arai, M.; Zhao, F. Y. The Pt-Enriched PtNi Alloy Surface and Its Excellent Catalytic Performance in Hydrolytic Hydrogenation of Cellulose. *ChemSusChem* **2014**, *7*, 1415-1421.
176. Jia, Q. Y.; Segre, C. U.; Ramaker, D.; Caldwell, K.; Trahan, M.; Mukerjee, S. Structure-Property-Activity Correlations of Pt-Bimetallic Nanoparticles: A Theoretical Study. *Electrochim. Acta* **2013**, *88*, 604-613.
177. Escalera-López, D.; Niu, Y.; Park, S. J.; Isaacs, M.; Wilson, K.; Palmer, R. E.; Rees, N. V. Hydrogen Evolution Enhancement of Ultra-Low Loading, Size-Selected Molybdenum Sulfide Nanoclusters by Sulfur Enrichment. *Appl. Catal., B* **2018**, *235*, 84-91.
178. Vajda, S.; White, M. G. Catalysis Applications of Size-Selected Cluster Deposition. *ACS Catal.* **2015**, *5*, 7152-7176.
179. Duncan, M. A. Invited Review Article: Laser Vaporization Cluster Sources. *Rev. Sci. Instrum.* **2012**, *83*.
180. Hesse, R.; Streubel, P.; Szargan, R. Improved Accuracy of Quantitative XPS Analysis Using Predetermined Spectrometer Transmission Functions with Unifit 2004. *Surf. Interface Anal.* **2005**, *37*, 589-607.
181. Singh-Miller, N. E.; Marzari, N. Surface Energies, Work Functions, and Surface Relaxations of Low-Index Metallic Surfaces from First Principles. *Phys. Rev. B* **2009**, *80*.
182. Hutter, J.; Iannuzzi, M.; Schiffmann, F.; VandeVondele, J. CP2K: Atomistic Simulations of Condensed Matter Systems. *Wiley Interdiscip. Rev.: Comput. Mol. Sci.* **2014**, *4*, 15-25.
183. VandeVondele, J.; Krack, M.; Mohamed, F.; Parrinello, M.; Chassaing, T.; Hutter, J. Quickstep: Fast and Accurate Density Functional Calculations Using a Mixed Gaussian and Plane Waves Approach. *Comput. Phys. Commun.* **2005**, *167*, 103-128.
184. Goedecker, S.; Teter, M.; Hutter, J. Separable Dual-Space Gaussian Pseudopotentials. *Phys. Rev. B* **1996**, *54*, 1703-1710.
185. Hirshfeld, F. L. Bonded-Atom Fragments for Describing Molecular Charge-Densities. *Theor. Chim. Acta* **1977**, *44*, 129-138.
186. Li, Y. D.; Liao, T. W.; Wang, C. X.; Chao, C. S.; Hung, T. C.; Ho, C. Y.; Luo, M. F.; Lai, Y. L.; Hsu, Y. J. The Decomposition of Methanol on Au-Pt Bimetallic Clusters Supported by a Thin Film of Al₂O₃/NiAl(100). *Rsc Advances* **2014**, *4*, 31602-31613.

187. Wu, F. L.; Huang, D. L.; Yue, Y.; Liu, L. Template Growth of Au, Ni and Ni-Au Nanoclusters on Hexagonal Boron Nitride/Rh(111): A Combined STM, TPD and AES Study. *Rsc Advances* **2017**, *7*, 44169-44177.
188. Netzer, F. P.; Madey, T. E. The Structure of CO on Ni(111). *J. Chem. Phys.* **1982**, *76*, 710-715.
189. Conrad, H.; Ertl, G.; Kuppers, J.; Latta, E. E. Adsorption of CO on Clean and Oxygen Covered Ni(111) Surfaces. *Surf. Sci.* **1976**, *57*, 475-484.
190. Stamenkovic, V. R.; Fowler, B.; Mun, B. S.; Wang, G. F.; Ross, P. N.; Lucas, C. A.; Markovic, N. M. Improved Oxygen Reduction Activity on Pt₃Ni(111) Via Increased Surface Site Availability. *Science* **2007**, *315*, 493-497.
191. Löwdin, P. O. On the Non-Orthogonality Problem Connected with the Use of Atomic Wave Functions in the Theory of Molecules and Crystals. *J. Chem. Phys.* **1950**, *18*, 365-375.
192. Hammer, B.; Morikawa, Y.; Norskov, J. K. CO Chemisorption at Metal Surfaces and Overlayers. *Phys. Rev. Lett.* **1996**, *76*, 2141-2144.
193. Mills, A.; LeHunte, S. An Overview of Semiconductor Photocatalysis. *J. Photochem. Photobiol., A* **1997**, *108*, 1-35.
194. Wenderich, K.; Mul, G. Methods, Mechanism, and Applications of Photodeposition in Photocatalysis: A Review. *Chem. Rev.* **2016**, *116*, 14587-14619.
195. Ismail, A. A.; Bahnemann, D. W.; Bannat, I.; Wark, M. Gold Nanoparticles on Mesoporous Interparticle Networks of Titanium Dioxide Nanocrystals for Enhanced Photonic Efficiencies. *J. Phys. Chem. C* **2009**, *113*, 7429-7435.
196. Mishra, Y. K.; Modi, G.; Cretu, V.; Postica, V.; Lupan, O.; Reimer, T.; Paulowicz, I.; Hrkac, V.; Benecke, W.; Kienle, L., et al. Direct Growth of Freestanding ZnO Tetrapod Networks for Multifunctional Applications in Photocatalysis, UV Photodetection, and Gas Sensing. *ACS Appl. Mater. Interfaces* **2015**, *7*, 14303-14316.
197. Grottrup, J.; Schutt, F.; Smazna, D.; Lupan, O.; Adelung, R.; Mishra, Y. K. Porous Ceramics Based on Hybrid Inorganic Tetrapodal Networks for Efficient Photocatalysis and Water Purification. *Ceram. Int.* **2017**, *43*, 14915-14922.
198. Mishra, Y. K.; Adelung, R. ZnO Tetrapod Materials for Functional Applications. *Mater. Today* **2018**, *21*, 631-651.
199. Reimer, T.; Paulowicz, I.; Roder, R.; Kaps, S.; Lupan, O.; Chemnitz, S.; Benecke, W.; Ronning, C.; Adelung, R.; Mishra, Y. K. Single Step Integration of ZnO Nano- and Microneedles in Si Trenches by Novel Flame Transport Approach: Whispering Gallery Modes and Photocatalytic Properties. *ACS Appl. Mater. Interfaces* **2014**, *6*, 7806-7815.
200. Kato, H.; Kudo, A. Visible-Light-Response and Photocatalytic Activities of TiO₂ and SrTiO₃ Photocatalysts Codoped with Antimony and Chromium. *J. Phys. Chem. B* **2002**, *106*, 5029-5034.

201. Padhi, D. K.; Parida, K. Facile Fabrication of Alpha-FeOOH Nanorod/RGO Composite: A Robust Photocatalyst for Reduction of Cr(VI) under Visible Light Irradiation. *J. Mater. Chem. A* **2014**, *2*, 10300-10312.
202. Jin, J.; Yu, J. G.; Guo, D. P.; Cui, C.; Ho, W. K. A Hierarchical Z-Scheme CdS-WO₃ Photocatalyst with Enhanced CO₂ Reduction Activity. *Small* **2015**, *11*, 5262-5271.
203. del Alamo, J. A. Nanometre-Scale Electronics with III-V Compound Semiconductors. *Nature* **2011**, *479*, 317-323.
204. Sivula, K.; Le Formal, F.; Gratzel, M. Solar Water Splitting: Progress Using Hematite (Alpha-Fe₂O₃) Photoelectrodes. *ChemSusChem* **2011**, *4*, 432-449.
205. Dhakshinamoorthy, A.; Navalon, S.; Corma, A.; Garcia, H. Photocatalytic CO₂ Reduction by TiO₂ and Related Titanium Containing Solids. *Energy Environ. Sci.* **2012**, *5*, 9217-9233.
206. Luna, A. L.; Novoseltceva, E.; Louarn, E.; Beaunier, P.; Kowalska, E.; Ohtani, B.; Valenzuela, M. A.; Remita, H.; Colbeau-Justin, C. Synergetic Effect of Ni and Au Nanoparticles Synthesized on Titania Particles for Efficient Photocatalytic Hydrogen Production. *Appl. Catal., B* **2016**, *191*, 18-28.
207. Luna, A. L.; Dragoe, D.; Wang, K. L.; Beaunier, P.; Kowalska, E.; Ohtani, B.; Uribe, D. B.; Valenzuela, M. A.; Remita, H.; Colbeau-Justin, C. Photocatalytic Hydrogen Evolution Using Ni-Pd/TiO₂: Correlation of Light Absorption, Charge-Carrier Dynamics, and Quantum Efficiency. *J. Phys. Chem. C* **2017**, *121*, 14302-14311.
208. Robert, D.; Malato, S. Solar Photocatalysis: A Clean Process for Water Detoxification. *Sci. Total Environ.* **2002**, *291*, 85-97.
209. Lonnen, J.; Kilvington, S.; Kehoe, S. C.; Al-Touati, F.; McGuigan, K. G. Solar and Photocatalytic Disinfection of Protozoan, Fungal and Bacterial Microbes in Drinking Water. *Water Res.* **2005**, *39*, 877-883.
210. Wen, M.; Cheng, M. Z.; Zhou, S. Q.; Wu, Q. S.; Wang, N.; Zhou, L. Y. Synthesis of Reusable NiCo@Pt Nanoalloys from Icosahedrons to Spheres by Element Lithography and Their Synergistic Photocatalysis for Nano-ZnO toward Dye Wastewater Degradation. *J. Phys. Chem. C* **2012**, *116*, 11702-11708.
211. Lin, H. X.; Xu, Z. T.; Wang, X. X.; Long, J. L.; Su, W. Y.; Fu, X. Z.; Lin, Q. Photocatalytic and Antibacterial Properties of Medical-Grade PVC Material Coated with TiO₂ Film. *J. Biomed. Mater. Res., Part B* **2008**, *87B*, 425-431.
212. Verbruggen, S. W. TiO₂ Photocatalysis for the Degradation of Pollutants in Gas Phase: From Morphological Design to Plasmonic Enhancement. *J. Photochem. Photobiol., C* **2015**, *24*, 64-82.
213. Zhao, X. J.; Zhao, Q. N.; Yu, J. G.; Liu, B. S. Development of Multifunctional Photoactive Self-Cleaning Glasses. *J. Non-Cryst. Solids* **2008**, *354*, 1424-1430.
214. Verbruggen, S. W.; Keulemans, M.; Goris, B.; Blommaerts, N.; Bals, S.; Martens, J. A.; Lenaerts, S. Plasmonic 'Rainbow' Photocatalyst with Broadband Solar Light Response for Environmental Applications. *Appl. Catal., B* **2016**, *188*, 147-153.

215. Verbruggen, S. W.; Keulemans, M.; Filippousi, M.; Flahaut, D.; Van Tendeloo, G.; Lacombe, S.; Martens, J. A.; Lenaerts, S. Plasmonic Gold-Silver Alloy on TiO₂ Photocatalysts with Tunable Visible Light Activity. *Appl. Catal., B* **2014**, *156*, 116-121.
216. Kafizas, A.; Kellici, S.; Darr, J. A.; Parkin, I. P. Titanium Dioxide and Composite Metal/Metal Oxide Titania Thin Films on Glass: A Comparative Study of Photocatalytic Activity. *J. Photochem. Photobiol., A* **2009**, *204*, 183-190.
217. Tahir, M.; Tahir, B.; Amin, N. A. S. Synergistic Effect in Plasmonic Au/Ag Alloy NPs Co-Coated TiO₂ Nws toward Visible-Light Enhanced CO₂ Photoreduction to Fuels. *Appl. Catal., B* **2017**, *204*, 548-560.
218. Kamimura, S.; Yamashita, S.; Abe, S.; Tsubota, T.; Ohno, T. Effect of Core@Shell (Au@Ag) Nanostructure on Surface Plasmon-Induced Photocatalytic Activity under Visible Light Irradiation. *Appl. Catal., B* **2017**, *211*, 11-17.
219. Mrowetz, M.; Villa, A.; Prati, L.; Selli, E. Effects of Au Nanoparticles on TiO₂ in the Photocatalytic Degradation of an Azo Dye. *Gold Bull.* **2007**, *40*, 154-160.
220. Mills, A.; Wang, J. S. Simultaneous Monitoring of the Destruction of Stearic Acid and Generation of Carbon Dioxide by Self-Cleaning Semiconductor Photocatalytic Films. *J. Photochem. Photobiol., A* **2006**, *182*, 181-186.
221. Paz, Y.; Luo, Z.; Rabenberg, L.; Heller, A. Photooxidative Self-Cleaning Transparent Titanium-Dioxide Films on Glass. *J. Mater. Res.* **1995**, *10*, 2842-2848.
222. Galhenage, R. P.; Yan, H.; Tenney, S. A.; Park, N.; Henkelman, G.; Albrecht, P.; Mullins, D. R.; Chen, D. A. Understanding the Nucleation and Growth of Metals on TiO₂: Co Compared to Au, Ni, and Pt. *J. Phys. Chem. C* **2013**, *117*, 7191-7201.
223. Akita, T.; Lu, P.; Ichikawa, S.; Tanaka, K.; Haruta, M. Analytical TEM Study on the Dispersion of Au Nanoparticles in Au/TiO₂ Catalyst Prepared under Various Temperatures. *Surf. Interface Anal.* **2001**, *31*, 73-78.
224. Allain, E.; Besson, S.; Durand, C.; Moreau, M.; Gacoin, T.; Boilot, J. P. Transparent Mesoporous Nanocomposite Films for Self-Cleaning Applications. *Adv. Funct. Mater.* **2007**, *17*, 549-554.
225. Verbruggen, S. W.; Masschaele, K.; Moortgat, E.; Korany, T. E.; Hauchecorne, B.; Martens, J. A.; Lenaerts, S. Factors Driving the Activity of Commercial Titanium Dioxide Powders Towards Gas Phase Photocatalytic Oxidation of Acetaldehyde. *Catal. Sci. Technol.* **2012**, *2*, 2311-2318.
226. Hurum, D. C.; Agrios, A. G.; Gray, K. A.; Rajh, T.; Thurnauer, M. C. Explaining the Enhanced Photocatalytic Activity of Degussa P25 Mixed-Phase TiO₂ Using EPR. *J. Phys. Chem. B* **2003**, *107*, 4545-4549.
227. Murdoch, M.; Waterhouse, G. I. N.; Nadeem, M. A.; Metson, J. B.; Keane, M. A.; Howe, R. F.; Llorca, J.; Idriss, H. The Effect of Gold Loading and Particle Size on Photocatalytic Hydrogen Production from Ethanol over Au/TiO₂ Nanoparticles. *Nat. Chem.* **2011**, *3*, 489-492.

228. Caretti, I.; Keulemans, M.; Verbruggen, S. W.; Lenaerts, S.; Van Doorslaer, S. Light-Induced Processes in Plasmonic Gold/TiO₂ Photocatalysts Studied by Electron Paramagnetic Resonance. *Top. Catal.* **2015**, *58*, 776-782.
229. Linic, S.; Christopher, P.; Ingram, D. B. Plasmonic-Metal Nanostructures for Efficient Conversion of Solar to Chemical Energy. *Nat. Mater.* **2011**, *10*, 911-921.
230. Priebe, J. B.; Karnahl, M.; Junge, H.; Beller, M.; Hollmann, D.; Bruckner, A. Water Reduction with Visible Light: Synergy between Optical Transitions and Electron Transfer in Au-TiO₂ Catalysts Visualized by in situ EPR Spectroscopy. *Angew. Chem., Int. Ed.* **2013**, *52*, 11420-11424.
231. Kuroki, H.; Tamaki, T.; Matsumoto, M.; Arao, M.; Kubobuchi, K.; Imai, H.; Yamaguchi, T. Platinum-Iron-Nickel Trimetallic Catalyst with Superlattice Structure for Enhanced Oxygen Reduction Activity and Durability. *Ind. Eng. Chem. Res.* **2016**, *55*, 11458-11466.
232. Zhang, C. L.; Sandorf, W.; Peng, Z. M. Octahedral Pt₂CuNi Uniform Alloy Nanoparticle Catalyst with High Activity and Promising Stability for Oxygen Reduction Reaction. *ACS Catal.* **2015**, *5*, 2296-2300.
233. Sneed, B. T.; Young, A. P.; Jalalpoor, D.; Golden, M. C.; Mao, S. J.; Jiang, Y.; Wang, Y.; Tsung, C. K. Shaped Pd-Ni-Pt Core-Sandwich-Shell Nanoparticles: Influence of Ni Sandwich Layers on Catalytic Electrooxidations. *ACS Nano* **2014**, *8*, 7239-7250.
234. Khanal, S.; Bhattarai, N.; McMaster, D.; Bahena, D.; Velazquez-Salazar, J. J.; Jose-Yacaman, M. Highly Monodisperse Multiple Twinned AuCu-Pt Trimetallic Nanoparticles with High Index Surfaces. *Phys. Chem. Chem. Phys.* **2014**, *16*, 16278-16283.
235. Wang, L.; Yamauchi, Y. Strategic Synthesis of Trimetallic Au@Pd@Pt Core-Shell Nanoparticles from Poly(Vinylpyrrolidone)-Based Aqueous Solution toward Highly Active Electrocatalysts. *Chem. Mater.* **2011**, *23*, 2457-2465.
236. Khanal, S.; Bhattarai, N.; Velazquez-Salazar, J. J.; Bahena, D.; Soldano, G.; Ponce, A.; Mariscal, M. M.; Mejia-Rosales, S.; Jose-Yacaman, M. Trimetallic Nanostructures: The Case of AgPd-Pt Multiply Twinned Nanoparticles. *Nanoscale* **2013**, *5*, 12456-12463.

List of Publications

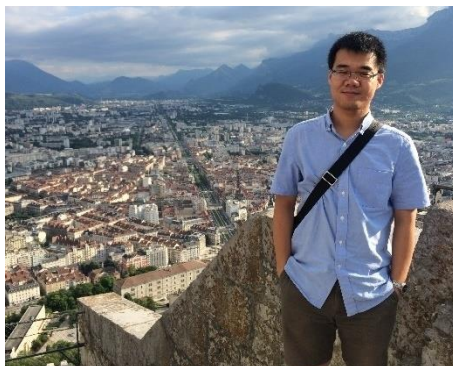
Publications at KU Leuven

- T.-W. Liao, A. Yadav, Y. Niu, J. Vernieres, P. Ferrari, K.-J. Hu, X.-K. Wei, M. Heggen, R. Dunin-Borkowski, D. Grandjean, E. Janssens, K. Laasonen, R. E. Palmer and Peter Lievens, *Reduction of CO poisoning of Pt nano-catalyst by alloying with Ni*, in preparation.
- L. Geerts, S. Cosentino, T.-W. Liao, A. Yadav, P.-C. Lin, V. S. Zharinov, K.-J. Hu, A. Longod, L. M. C. Pereira, D. Grandjean, J. Rongé, P. Lievens and J. A. Martens, “*Highly Active Oxygen Evolution Reaction Model Electrode based on supported Gas-Phase NiFe Clusters*”, submitted to Catalysis Today.
- T.-W. Liao, A. Yadav, K.-J. Hu, J. van der Tol, S. Cosentino, F. D’Acapito, D. Grandjean, R. E. Palmer, C. Lenardi, R. Ferrando, P. Lievens, “*Unravelling the nucleation mechanism of core-shell nanoparticles with tunable atomic arrangement*”, *Nanoscale*, 10, (2018), 6684-6694.
- T.-W. Liao, S. W. Verbruggen, N. Claes, A. Yadav, D. Grandjean, S. Bals and P. Lievens, “*TiO₂ Films Modified with Au Nanoclusters as Self-cleaning Surfaces under Visible Light*”, *Nanomaterials*, 8, (2018), 30.
- P. Ferrari, J. Vanbuel, Y. Li, T.-W. Liao, E. Janssens, P. Lievens, “*Modification of gas aggregation sources: The double laser ablation source approach*”, Book chapter in “*Gas Aggregation Synthesis of Nanoparticles*”, Y. Huttel (editor), Wiley (2017).
- S. Cosentino, G. Fiaschi, V. Strano, K.-J. Hu, T.-W. Liao, N. M. Hemed, A. Yadav, S. Mirabella, D. Grandjean, P. Lievens, Y. Shacham-Diamand, “*Role of Au_xPt_{1-x} Clusters in the Enhancement of the Electrochemical Activity of ZnO Nanorod Electrodes*”, *J. Phys. Chem. C*, 121, (2017), 15644–15652.
- Z. Li, H.-Y. Chen, K. Schouteden, T. Picot, K. Houben, T.-W. Liao, C. Van Haesendonck, G. Pacchioni, P. Lievens, and E. Janssens, “*Size-Dependent Penetration of Gold Nanoclusters through a Defect-Free, Nonporous NaCl Membrane*”, *Nano Lett.*, 16, (2016), 3063–3070.

Publications before my PhD

- T.-C. Hong, T.-W. Liao, Z.-H. Liao, P.-W. Hsu, P.-Y. Cai, W.-H. Lu, J.-H. Wang and M.-F. Luo, “*Dependence on size of supported Rh nanoclusters for CO adsorption*”, RSC Adv., 6, (2016), 3830.
- T.-C. Hong, T.-W. Liao, Z.-H. Liao, P.-W. Hsu, P.-Y. Cai, H. Lee, Y.-L. Lai, Y.-J. Hsu, H.-Y. Chen, J.-H. Wang and M.-F. Luo, “*Dependence on Size of Supported Rh Nanoclusters in the Decomposition of Methanol*”, ACS Catal., 5, (2015), 4276–4287.
- C.-S. Chao, T.-W. Liao, C. X. Wang, Y.-D. Li, T.-C. Hung and M.-F. Luo, “*Decomposition of methanol on partially alumina-encapsulated Pt nanoclusters supported on thin film $Al_2O_3/NiAl(100)$* ”, Appl. Surf. Sci. 311 (2014) 763–769.
- Y.-D. Li, T.-W. Liao, C. X. Wang, T.-C. Hong, and M.-F. Luo, “*The Decomposition of methanol on Au-Pt bimetallic nanoclusters supported on a thin film of $Al_2O_3/NiAl(100)$* ”, RSC Adv., 4 (2014) 31602-31613.
- C.-S. Chao, T.-W. Liao, C. X. Wang, Y.-D. Li, T.-C. Hung and M.-F. Luo, “*Obstruction by CO of the decomposition of methanol on Pt nanoclusters on a thin film of $Al_2O_3/NiAl(100)$* ”, Appl. Surf. Sci. 293 (2014) 352– 358.
- Y.-D. Li, T.-C. Hong, T.-W. Liao and M.-F. Luo, “*Surface structures of Au-Pt bimetallic nanoclusters on thin film $Al_2O_3/NiAl(100)$ probed with CO*”, Surf. Sci. 618 (2013) 132-139.

Curriculum Vitae



Ting-Wei Liao

Date of Birth: 30th September 1986

Place of Birth: Yunlin, Taiwan

2014-2018 **Department of Physics and Astronomy, KU Leuven, Belgium.**

European Union FP7-ITN Marie Curie PhD Fellowship and doctorate of Science in Physics with thesis entitled “*Production and characterization of novel catalysis based on bimetallic deposited clusters*”.

2013-2014 **Nano-scale Physics Laboratory, National Central University, Taiwan.**

Research Assistant, *Catalytic properties of oxide supported mono/bimetallic nanoclusters.*

2009-2012 **Department of Physics, National Central University, Taiwan.**

Master of Science in Physics with thesis entitled “*The Building of the Molecular Beam System*”.

2005-2009 **Department of Physics, National Central University, Taiwan.**

Bachelor of Science in Physics with a minor in Astronomy.